UNIVERSITY of CALIFORNIA
Santa Barbara

Effects of Fiber Architecture on Damage and Failure in C/SiC Composites

A Dissertation submitted in partial satisfaction of the
requirements for the degree

Doctor of Philosophy
in
Materials

by

John Henry Shaw

Committee in charge:

Professor Frank W. Zok, Chair
Professor Carlos G. Levi
Professor Matthew R. Begley
Professor Robert M. McMeeking

December 2014

The dissertation of John Henry Shaw is approved.

_____

Professor Carlos G. Levi

_____

Professor Matthew R. Begley

_____

Professor Robert M. McMeeking

_____

Professor Frank W. Zok, Committee Chair

November 2014

Effects of Fiber Architecture on Damage and Failure in C/SiC Composites

by

John Henry Shaw

for Meaghan

Acknowledgements

I would like to thank my advisor, Frank Zok, for allowing me the freedom to approach problems in my own way. His guidance has been of tremendous value to my professional development.

I gratefully acknowledge the National Hypersonics Science Center for Materials and Structures for funding this work. I would also like to thank the many members of the NHSC whose contributions made this work possible: Hrishi Bale, Renaud Rinaldi and Matthew Blacklock for providing the foundation of the computational aspects of this project; Mark Novak for developing the laser testing facility at UCSB; Michael Rossol and Tony Fast for their work on characterizing fabric deformation; Qingda Yang, Mehdi Naderi, Bao-Chan Do and Derek Schesser for their assistance in developing models based on the augmented finite element method; and David Marshall and Brian Cox for numerous insightful interactions.

I thank my colleagues at UCSB in the Zok, Levi, and Begley groups for lending me a vast pool of knowledge. In particular I would like to thank Varun Rajan, Michael Rossol and Brett Compton. In addition to helping me to solve many problems, they have become great friends. Thanks also to Peter Maxwell and Kirk Fields, who were able to overcome all obstacles in the lab.

I thank my parents, Nancy Gierlich and Robert Shaw, and my sister, Courtney Shaw, for being a source of confidence. Their unconditional faith in me has given me the courage to tackle many challenges.

Finally, I thank my wife, Meaghan, for her constant love and support.

Curriculum Vitæ

John Henry Shaw

Education

2005–2009	B.S. in Materials Science and Engineering, Economics Rutgers, The State University of New Jersey Piscataway, NJ
2009–2014	Ph.D. in Materials University of California, Santa Barbara Santa Barbara, CA

Publications

M. N. Rossol, J. H. Shaw, H. Bale, R. O. Ritchie, D. B. Marshall, and F. W. Zok. Characterizing Weave Geometry in Textile Ceramic Composites Using Digital Image Correlation. *Journal of the American Ceramic Society*, 96(8):2362–2365, 2013.

J. H. Shaw, V. P. Rajan, M. Blacklock, and F. W. Zok. Towards Virtual Testing of Textile Composites: Calibration of Thermoelastic Tow Properties. *Journal of the American Ceramic Society*, 97(4):1209–1217, 2014.

B. N. Cox, H. A. Bale, M. Begley, M. Blacklock, B. C. Do, T. Fast, M. Naderi, M. Novak, V. P. Rajan, R. G. Rinaldi, R. O. Ritchie, M. Rossol, J. H. Shaw, O. Sudre, Q. Yang, F. W. Zok, and D. B. Marshall. Stochastic Virtual Tests for High-Temperature Ceramic Matrix Composites. *Annual Review of Materials Research*, 44:479–529, 2014.

V. P. Rajan, J. H. Shaw, M. N. Rossol, and F. W. Zok. An Elastic-Plastic Constitutive Model for Ceramic Composite Laminates. *Composites Part A*, 66:44–57, 2014.

J. H. Shaw, M. N. Rossol, D. B. Marshall, and F. W. Zok. Effects of Tow-Scale Holes on the Mechanical Performance of a 3D Woven C/SiC Composite. *In press, Journal of the American Ceramic Society*.

M. Blacklock, J. H. Shaw, F. W. Zok, and B. N. Cox. Calibrated Stochastic Virtual Specimens for Analyzing Local Strain Variations in Woven Ceramic Composites, *In Preparation*.

J. H. Shaw, M. N. Rossol, D. B. Marshall, and F. W. Zok. Effects of Preform Shear on Tensile Properties of a Woven C/SiC Composite, *In Preparation*.

J. H. Shaw, V. P. Rajan, and F. W. Zok. Failure of Woven Ceramic Composites in Biaxial and Uniaxial Flexure, *In preparation*.

J. W. Pro, J. H. Shaw, F. W. Zok, and M. Begley. A Discrete Element Method Model for Thermally-Induced Matrix Cracking in a C/SiC Composite, *In preparation*.

J. H. Shaw, D. B. Marshall, and F. W. Zok. Effects of Warp Wavelength on Damage and Failure in an Angle-Interlock C/SiC Composite, *In preparation*.

Abstract

Effects of Fiber Architecture on Damage and Failure in C/SiC Composites

by

John Henry Shaw

Carbon-fiber/SiC-matrix composites are under development for applications in hypersonic vehicles due to their exceptional capabilities at high temperatures. As a subset of these materials, textile-based composites are of particular interest because they offer the possibility of accommodating complex geometries and features in engineering components. Among the numerous obstacles hindering the widespread adoption of these composites, two are addressed in the present work: (i) the incomplete understanding of the influence of textile architecture on thermoelastic properties, damage initiation and failure, and (ii) the lack of robust computational tools for predicting their thermomechanical performance at the appropriate length scales. Accordingly, an experimental study is performed of the thermal and mechanical properties of several prototypical textile C/SiC composites with various fiber architectures. In turn, the experimental results are used to guide the development of computational tools

for predicting composite response that explicitly account for fiber architecture.

Textile architecture is found to influence composite response at four length-scales: the panel, the coupon, the tow, and the sub-tow. At the *panel scale*, distortions to the architecture introduced during weaving or handling of the fabric influence the packing density and the relative rotation of tows. Even when large distortions are intentionally introduced their influence on mechanical response is minimal. At the *coupon scale* the tow architecture has the largest effects on composite mechanical response. Young's modulus, ultimate tensile strength, and strain to failure are all influenced. Changes in each of these are a function of tow shape, tow anisotropy, and the degree of constraint provided by the matrix.

At the *tow scale*, architecture effects give rise to heterogeneity in measured surface strains under both tensile and thermal loading. Methods for the calibration of tow-scale elastic and thermoelastic properties were developed to enable simulation of these effects with a geometrically-accurate virtual model. Virtual tensile and thermal tests using this model have indicated that interaction between tows has an important influence on local strains. At the *sub-tow scale*, architecture effects influence the location of matrix cracking. Simulations of the cooling cycle following matrix processing predict that matrix cracks should develop in the matrix above underlying tows due to thermal

expansion mismatch between the tows and the matrix. This is consistent with experimental observations. Two methods are presented to extend the virtual tests to explicitly simulate the onset and evolution of these cracks.

Contents

List of Figures

List of Tables

Chapter 1

Introduction

1.1 Material needs for hypersonic flight

Air-breathing hypersonic flight has long been a field of interest for both space programs and national defense programs. Whereas high speeds are of primary interest for weapon systems, the goal for space access is a fully reusable vehicle. A true space plane—capable of horizontal takeoff and landing—would dramatically reduce the cost and time involved in reaching space, enabling frequent orbital missions (Joint Technology Office on Hypersonics, 2008). At minimum, an onboard propulsion source would replace the (typically single-use) second-stage rocket boosters to provide thrust in the upper atmosphere. The candidate propulsion system for achieving this goal is

the scramjet, which is an air-breathing engine capable of operating at speeds of Mach 4–10. After decades of research, the viability of scramjets has recently been demonstrated. The X-51A program achieved the longest-ever scramjet-powered hypersonic flight; the test vehicle (Fig. 1.1) reached a speed of Mach 5.1 for a duration of 210 seconds using JP-7 jet fuel (Boeing, 2013).

In a recent report to the U.S. Congress, the Joint Technology Office on Hypersonics identified several technology areas critical to the continued development of hypersonic vehicles (Joint Technology Office on Hypersonics, 2008). One of these areas is the development of advanced materials for hot section components. While all flight demonstrations of scramjets to date have utilized metallic alloys, substantial benefits would be realized by using ceramic matrix composites (CMCs). One reason for this is illustrated in Figure 1.2. Only a handful of metallic systems (notably molybdenum and a few refractory alloys) are capable of surviving surface temperatures in excess of 1200 °C. Compared to those metallic systems, C/SiC and SiC/SiC composites exhibit a three-fold higher specific strength. Scramjets are relatively large in proportion to the total size of a hypersonic vehicle (Fig. 1.1), so the weight savings from using composites in place of metals would be significant.

The potential weight benefits of CMCs for hot section components were examined by Vermaak et al. (2009). Vermaak et al. (2009) examined the fea-

sibility of various materials for use in a notional scramjet combustor panel. They determined whether, for a range of coolant flow rates and heat transfer coefficients between combustion gases and the panel surface, there was a viable design for a panel constructed from a given material. Although the focus of the research was on optimization of metallic systems, C/SiC was used as a baseline for comparison. In the two panel configurations studied, C/SiC performed well without any addition of a thermal barrier coating (TBC). When the panel weight was calculated for an assumed set of flow rates and heat transfer coefficients, C/SiC was always lighter than any metallic system by at least a factor of two.

As a subset of CMCs, *textile-based* composites offer considerable benefits due to their high level of possible customization. Composite stiffness can be tailored to anticipated loads by adjusting the orientation and volume fraction of fibers. The high heat fluxes expected in hypersonic applications can be managed by incorporating high thermal conductivity fibers in the through-thickness direction of weaves. The feasibility of CMCs has been demonstrated in similar high heat flux applications. Marshall and Cox (2008) manufactured a prototype of a combustor liner from an angle-interlock textile composite. The part contained similar features to those required of a scramjet engine: a variety of fuel and air inlets and complex geometric shape. Figure 1.3(a) shows the inner face of the combustor liner. The liner contains film-cooling holes as well as

fuel and combustion air holes (not seen). They were introduced directly into the fabric without machining of the composite. On the reverse face, shown in Figure 1.3(b), anchor loops were incorporated in the fabric for direct attachment to the underlying alloy structure. The combustor liner was tested under conditions representative combustion in a turbine engine; all of the above features functioned as intended.

Another technology identified as being in need of development by the Joint Technology Office on Hypersonics (2008) is a computational tool for the assessment of material or component performance. Such a tool would minimize expensive testing, which would be particularly useful for CMCs. Since textiles contain inherent geometric variations introduced in manufacturing, many test specimens would be required to certify their mechanical properties. Further complications are encountered at the component scale, where a geometric feature may interact with the underlying textile geometry. The framework for a suitable *virtual test* has been outlined by Cox and Yang (2006). Such a virtual test would explicitly incorporate both textile and component geometries as well as all mechanisms known to occur in the failure process (*e.g.*, matrix cracking, interface debonding, and tow rupture). Many virtual specimens could be generated with varying input properties (such as tow geometry, elastic constants or cohesive parameters) to simulate the expected variation in component strength. These capabilities could potentially greatly reduce the number

of specimens required for testing, and could help refine the design of large-scale components prior to proof-of-concept testing.

1.2 Mechanical response of textile composites

Textile composites are influenced by their underlying fabric architecture in numerous ways. A study by Berbon et al. (2002) of SiC/SiC composites with a CVI matrix has shown that tow shape influences several characteristics of mechanical performance. Two angle-interlock textile composites with varying degrees of tow waviness (defined as a deviation from a straight path) were tested in tension; increased tow waviness was found to decrease both the Young's modulus and the ultimate tensile strength. To a lesser degree, tow waviness was also correlated with increased strain to failure. These observations are consistent with previous work on polymer matrix composites (PMCs) (Cox and Dadkhah, 1995; Cox and Flanagan, 1997), where it was observed that tow waviness has a large impact on composite stiffness. Estimated reductions in composite Young's modulus can be up to 10 % even for relatively straight tows, such as those of satin weaves or the weft tows of angle-interlock weaves (Cox and Flanagan, 1997). In weaves where the waviness is higher, such as plain weaves, the knockdown in stiffness can be as high as 50 %.

The cross-sectional area of tows has also been correlated with the onset of

matrix cracking. Morscher et al. (2009) compared the tensile response of a variety of textile-based melt-infiltrated SiC/SiC CMCs. Angle-interlock weaves, 5-harness satin weaves, 3D orthogonal weaves, and 2D tri-axial braids were included in the study. The matrix cracking stress was determined for each specimen by the onset of acoustic emission. When the matrix cracking stress was plotted against the quantity $f_0/(A_\perp)^{1/2}$, where f_0 is the fiber volume fraction aligned with the loading direction and $A_\perp$ is the cross-sectional area of the transverse tows, the measured values of matrix cracking stress collapsed into a narrow band. The inverse root scaling with $A_\perp$ suggests that the tightly packed bundles of transverse fibers—as found in textile weaves—act like voids in initiating flaws. This behavior was attributed to the fact that the porosity within fiber bundles is much higher than the porosity between fiber bundles in melt-infiltrated composites.

Measurements of full-field strains make it possible to infer the locations of the onset of matrix cracking. This is critical in evaluating CMC performance, since cracks can result in dramatic loss of properties if fibers are exposed to the environment at service temperatures. Using laser speckle interferometry, Berbon et al. (2002) measured surface strains on a two-layer angle-interlock SiC/SiC composite loaded in tension. Strain concentrations developed in regions where axial and transverse tows cross each other when loaded in either the warp or the weft direction. In some cases, these strain concentrations ap-

peared to develop before the onset of nonlinearity in the global stress-strain response. The strain concentrations were found to relate to debond cracks formed between the two tow populations, which effectively decoupled the transverse tows from the applied load. Similar debond cracks have been observed in other textile-based CMC systems (Chawla et al., 1998; Siron and Lamon, 1998).

Architecture-dependence of strain concentrations was also observed in tensile tests on an 8-harness satin weave SiC/SiC composite with a matrix derived from polymer infiltration and pyrolysis (PIP) (Rajan et al., 2012). Using digital image correlation (DIC) for strain mapping, cracks were shown to initiate in axial tows adjacent to regions where transverse tows cross over to the surface (Fig. 1.4). The hypothesis is that the crossover of the transverse tow results in some curvature in the neighboring axial tow, which elevates the strain locally and initiates the first cracks. The localized cracking appears to influence the path of the dominant crack at fracture; it passes through several crossover points. Similar periodicity of strain concentrations corresponding to tow architecture has been observed in a wide range of other fabrics and loading conditions in both CMCs and PMCs (Daggumati et al., 2011; Ivanov et al., 2009; Qin et al., 2012).

1.3 Modeling of textile composites

Selection of an appropriate CMC model depends on the length scale of interest. When modeling large components, where features are much larger than the unit cell of the textile, the composite may be effectively homogenized using phenomenological models (Genin and Hutchinson, 1997; Hahn, 1973; Rajan and Zok, 2013; Rajan et al., 2014). These models do not rely on explicit knowledge of constituent and interphase properties. They are calibrated by measuring the global composite response with mechanical tests both on- and -off axis to the fiber directions. Local strain fields around strain concentrators have been shown to be captured accurately (Genin and Hutchinson, 1997; Rajan et al., 2014). Difficulties arise in textile composites when the size of the strain concentrators is similar to the tow dimensions. For example, Rajan et al. (2014) found that simulations of the strain field around a hole agreed well in magnitude and spatial extent with DIC measurements. However, the experimental measurements detected an additional strain concentration near the hole that could not be accounted for in the model (circled in Figure 1.5). This concentration was attributed to the underlying fabric architecture.

When strain concentrators are of the same scale as architectural features, it becomes essential to explicitly model the tows. One approach for including tows is the binary model (Cox et al., 1994; McGlockton et al., 2003; Xu

et al., 1995). In the binary model, each tow is consolidated into a chain of 1D elements embedded within an effective medium. Tows are assumed to bear only axial load. The effective medium is a homogenous representation of the matrix, any porosity, and the transverse properties of the fibers. The material properties of individual composite constituents must therefore be known explicitly. The binary model is versatile enough to model complex damage mechanisms—including matrix softening and fracture, stochastic tow strength, and fiber pullout (McGlockton et al., 2003)—provided the constitutive laws governing each mechanism are known. Interaction between stress concentrators and architectural features may be captured by averaging the contribution of each over the width of the tow (Yang and Cox, 2010); when the bundle strength of the tow is exceeded, it would be expected to fail. By explicitly modeling tow paths, heterogeneity in surface strains corresponding to the tow architecture has been detected (Flores et al., 2010; Yang and Cox, 2010).

In the previous manifestations, the binary model could not detect strain localizations that occur at length-scales at or below the tow dimension. Since experimental measurements on CMCs indicate that crack initiation and the path of crack propagation is governed by the tow geometry (Berbon et al., 2002), it is necessary to explicitly represent the cross-sectional shape of the tow in a model to predict matrix cracking. Such a model would introduce new

complexities in geometry generation and meshing, though similar approaches have been used to model the deformation of textiles (Badel et al., 2007). An additional challenge is the definition of material properties. The material must now be homogenized within the tow. If the fibers are transversely isotropic, five elastic constants are required to describe the tow properties. Although composite micromechanical models have been developed to calculate these properties based on constituent properties (Christensen and Lo, 1979; Hashin, 1979; Hashin and Rosen, 1964; Levin, 1967), some calibration may be required if the matrix microstructure within the tow is complex. The development of a tow-scale model is therefore a multi-step process involving: characterization of the tow architecture, building a mathematical representation of the architecture, building a virtual geometry from the mathematical representation of the composite, and measuring both elastic and inelastic composite properties to calibrate the model (Cox et al., 2014).

1.4 Outline of dissertation

The National Hypersonics Science Center was established jointly by the National Aeronautics and Space Administration and the Air Force Office of Scientific Research to address, in part, the two research areas introduced above: the development of materials for hypersonic applications and the de-

velopment of models for rapid assessment of material and component performance. As a part of the Center, the broad goal of the research presented in this dissertation is to develop a more comprehensive understanding of the architecture-dependence of mechanical behavior of textile-based CMCs. Using a prototypical composite developed for the project by Teledyne Scientific, Inc., full-field strain measurements are used to study the influence of the underlying weave architecture on both global composite response as well as local heterogeneity in strain. The onset and propagation of surface damage are also correlated to weave architecture. The experimental measurements are combined with parallel work by other researchers in the Center. Notably, this work included the development of a virtual geometry of the model composite (Bale et al., 2012; Blacklock et al., 2012; Cox et al., 2014; Rinaldi et al., 2012). Together, the virtual geometry and experimental measurements are used to guide the development of a virtual test.

The dissertation is organized in the following way. Descriptions of the prototypical composites used in this study, as well as the methods by which a virtual model of the material is created, are presented in Chapter 2. The mechanical and thermal responses of the prototypical composites are presented in Chapters 3 and 4, respectively. Analytical models are developed to enhance understanding of composite mechanical response. Mechanical and thermal tests are used in the calibration of the virtual model. The model is validated

by predicting strain heterogeneity observed in tensile tests. The effects of modifications to the weave geometry on mechanical performance are discussed in Chapter 5. These include holes introduced directly into the fabric (as described above) as well as shear defects. Two modeling techniques for discrete damage are described in Chapter 6: the discrete element method (DEM) and the augmented finite element method (AFEM). Finally, the lessons learned through this study and thoughts on future research are discussed in Chapter 7.

Figure 1.1: The X51-A hypersonic test vehicle mounted to the wing of a B-52 bomber. The forward section is the scramjet-powered vehicle, while the region behind the first set of fins is a booster rocket to accelerate the vehicle to Mach 4. The scramjet engine comprises most of the lower section of the vehicle: approximately the full region with a metallic finish. (Wright-Patterson Air Force Base, 2012)

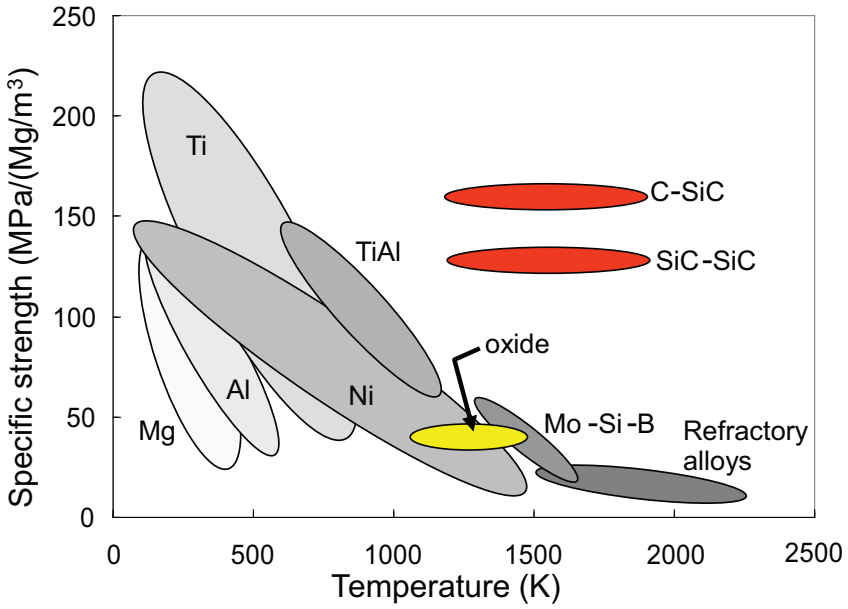

Figure 1.2: Candidate materials for hypersonic vehicle applications. Of the few materials capable of sustaining high surface temperatures (>1500 K), composites offer the greatest specific strength.

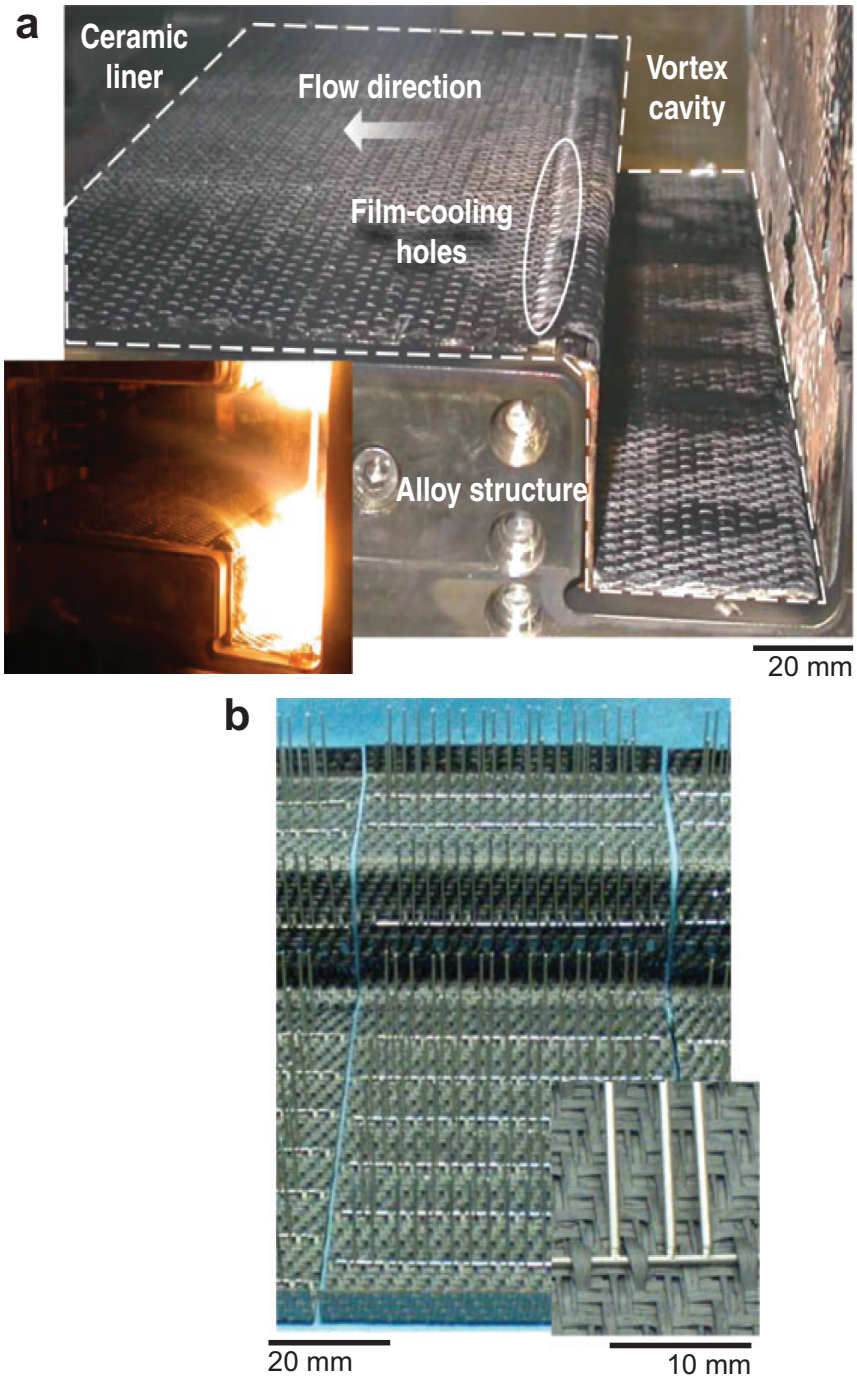

Figure 1.3: Demonstration of a multi-featured SiC/SiC combustor liner (Marshall and Cox, 2008). (a) The inside face of the combustor wall contains film-cooling, transpiration, fuel and combustion air holes, all of varying sizes. (b) The outside face has anchor loops for attachment to the surrounding alloy structure.

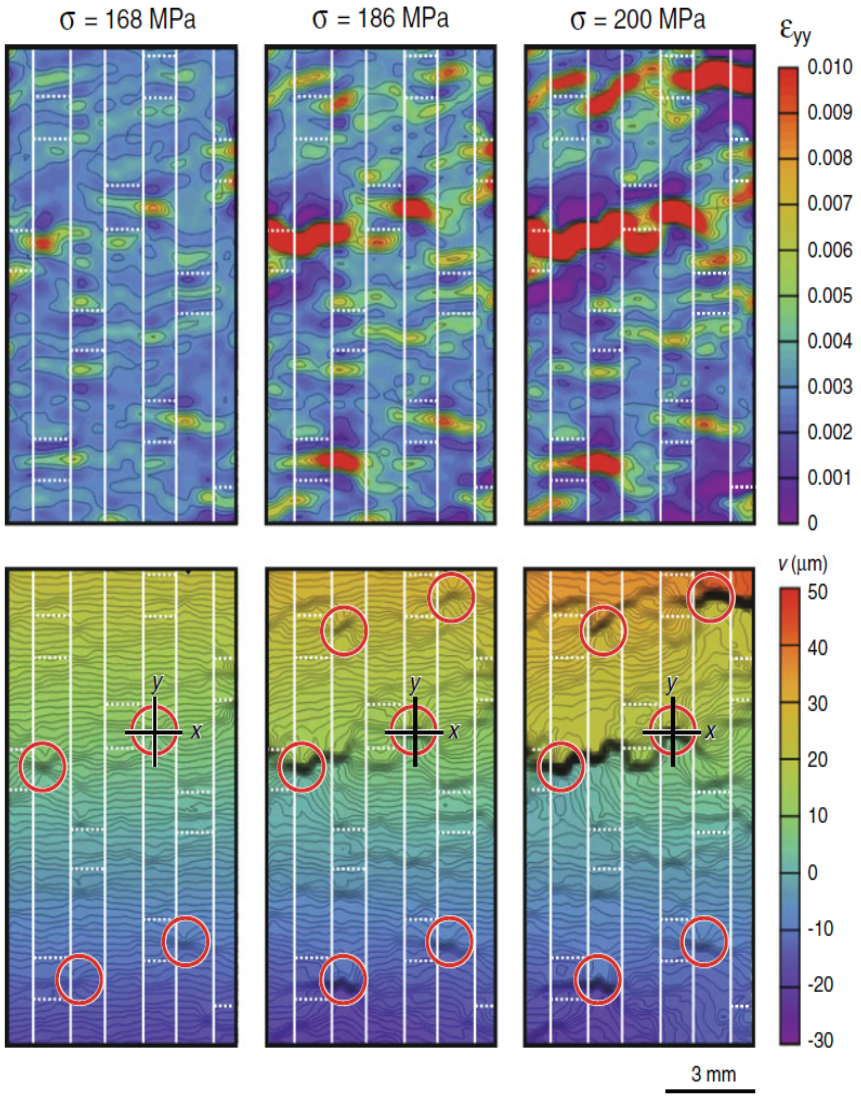

Figure 1.4: Architecture-dependent strain concentrations in an eight-harness satin weave SiC/SiC composite (Rajan et al., 2012). Cracks initiate near tow crossover points.

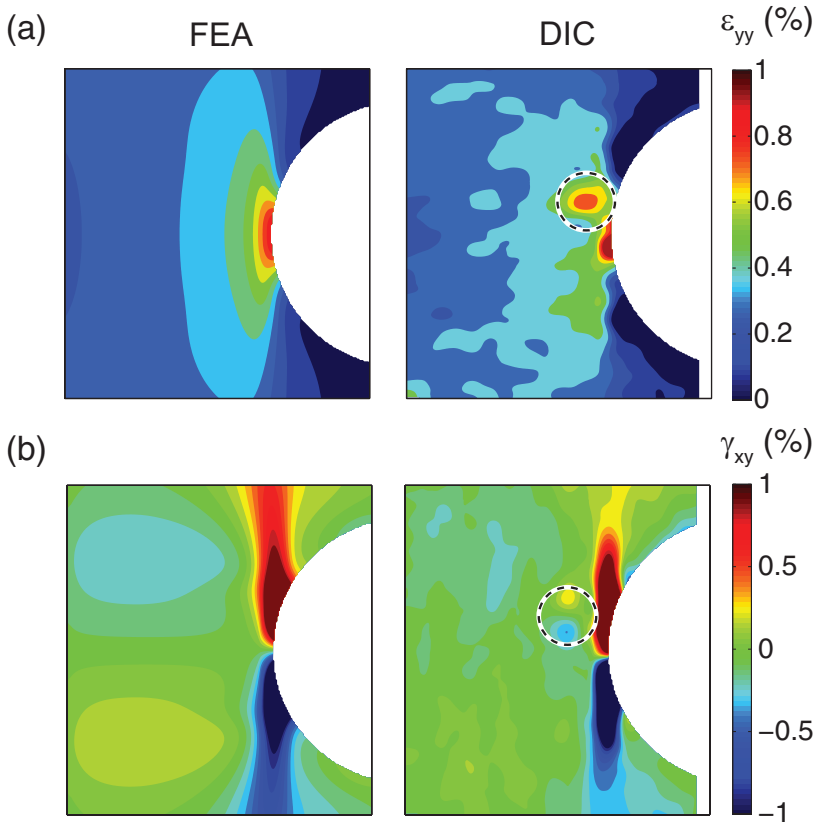

Figure 1.5: Predicted (FEA) and measured (DIC) surface distributions of (a) axial and (b) shear strains in a tensile test of a coupon containing a central hole. DIC measurements indicate a strain concentration associated with underlying architectural features (circled). Adapted from Rajan et al. (2014).

Chapter 2

The physical and virtual material system

2.1 Introduction

All materials examined in this body of work comprise woven C-fiber SiC-matrix composites manufactured by Teledyne Scientific, Inc. The composites were chosen to satisfy two goals. The first was the development of a virtual textile composite, which requires a composite with well-defined tow geometry that lends itself to characterization by tractable mathematical approximations. To this end, the composites were produced in two stages: partial-densification of the fabric preform via chemical vapor infiltration (CVI), followed by fur-

ther densification using a combination of slurry processing and polymer impregnation and pyrolysis (PIP) techniques. The CVI processing stage yields a rigid composite with clearly defined tows, which aids in the characterization of the tow paths and cross-sections. The second goal was the experimental evaluation of the influence of composite architecture on elastic response and the evolution of matrix damage, using both the partially-processed and fully-processed composites.

The chapter is organized in the following way. The fiber architecture, composite fabrication process and material microstructure are described in the first section. The next section contains details of the construction of a virtual composite from the physical version. This occurs in four steps: (i) the tow geometry is characterized by x-ray computed tomography (CT); (ii) mathematical descriptors of tow paths and cross-sections are obtained from the CT data; (iii) the mathematical descriptors are used to generate a 1-dimensional (1D) model of the fabric; and (iv), the 1D model of each tow is expanded into a 3D surface. The resulting virtual composite is utilized for numerical simulations of mechanical and thermal loadings, as detailed in subsequent chapters.

2.2 Material

2.2.1 Fabric architecture

The fiber preforms consist of three-layer angle interlock weaves of T300-6K tows. The tows fall into one of three types: (i) nominally straight surface wefts, one set evident on each of the two surfaces, (ii) central wefts, also nominally straight and residing midway between the two surface weft populations, and (iii) warp tows that weave through-thickness, transverse to the wefts. One unit cell of the fabric contains sixteen distinct tows: four warps, eight surface wefts (four on each face), and four central wefts. Fabrics were woven in two different configurations, distinguished from each other by the unit cell size. In one, the unit cell dimensions were 5.1 mm and 11.1 mm in the weft and warp directions, respectively; in the other, they were 5.1 mm and 7.5 mm in the weft and warp directions, respectively. Hereafter they are referred to as the large and the small unit cell fabrics. The resulting composite panels were $\sim$ 1.4 mm thick; thus, the only difference between the two was the wavelength of the warp weavers and, correspondingly, the packing density of the weft tows. The unit cells and tow populations of each fabric are indicated in Figures 2.1(a) and 2.2(a).

The unit cell size influences the shape of the tows. One measure of tow

shape is the degree to which the tow paths deviate from a straight line, referred to here as tow waviness. Tow waviness is characterized by d/λ, where d is the amplitude and λ is the wavelength of the out-of-plane variation of the tow centerline (Berbon et al., 2002); a value of zero corresponds to a perfectly straight tow. Tow waviness was measured from optical cross-sections along each tow population (Figures 2.1(b&c) and 2.2(b&c)) and the known unit cell parameters. Half of the change in the z coordinate between the peak and trough of the tow path, measured at the tow mid-plane, was taken to be d. The unit cell dimension in the tow direction was taken to be λ. A summary of the waviness parameters for the warp and weft tows of the large and small unit cell fabrics is presented in Table 2.1. Among the weaves, higher values of tow waviness are obtained in the small unit cell fabric in both the warp and the weft tows. This trend is expected for the warp tows, since they have the same amplitude over a shorter wavelength in the smaller unit cell. The waviness in the weft tows is attributable to the weaving process: the untensioned weft tows are readily deformed by the warps during weaving (Cox and Flanagan, 1997). This effect appears to be greater for the tighter tow packing of the smaller unit cell fabric.

The other difference between the two fabrics is the cross-sectional shape of the tows. In the larger unit cell fabric, the tow cross-sections are approximately elliptical (Fig. 2.1). The aspect ratios of the cross-sections, defined as a/b where a is the major axis and b is the minor axis, were measured by Bale

et al. (2012) from x-ray CT images of all tows contained within a single unit cell. The average aspect ratio of the warp tows is 6.3; the aspect ratio of the center and surface weft tows is 5.1. In contrast, in the smaller unit cell fabric, the cross-sections of the weft tows are rhombic in shape (Fig. 2.2). The warp tow cross-sections are again approximately elliptical in shape. Aspect ratios of the cross-sections of the small unit cell fabric were measured from optical micrographs of the composite: the major axis a was taken as the widest point of the tow, and the minor axis b was the widest part of the tow normal to the major axis. The measured aspect ratios are 4.6 and 2.9 for the warp and weft tow cross-sections, respectively. These measurements are subject to more uncertainty than those of the large unit cell fabric since they were obtained from optical micrographs containing only 10–15 tows. The difference in weft tow cross-sectional shape and aspect ratio is a result of the change in unit cell size between the two fabrics. In the smaller unit cell fabric the weft tows are naturally pushed closer together, resulting in a lower aspect ratio and a change in cross-sectional shape.

2.2.2 Composite fabrication and microstructure

The composite panels were fabricated from the fabric preforms in two stages. In the first, the fibers within the preform were coated with a thin layer

($\sim$ 1 µm) of pyrolytic carbon via chemical vapor infiltration (CVI). The preform was then infiltrated with CVI SiC, to the extent that the tows were bonded to one another and the composite was "rigidified". Processing was halted at this point in order to image the composite. Two methods were employed. In one, x-ray CT images were obtained by Bale et al. (2012) and used to characterize local variations in tow shape (as discussed in the preceding section). In the other, the surface topography was imaged using either digital image correlation (Rossol et al., 2014) or high-resolution optical scans. The results were used to measure variations in the tow paths. With both methods, a fully-processed SiC matrix would have hindered measurement of the pertinent features. Small panels of the partially-processed composite were retained to evaluate the mechanical response in the absence of a complete matrix.

In the second fabrication stage, composite panels were further densified by repeated cycles of infiltration and pyrolysis of slurries of SiC particles in a preceramic polymer (AHPCS polymer, Starfire Systems Inc., Schenectady, NY). The fully-processed materials were used to evaluate the role of fabric architecture in the progression of matrix damage under applied load, aiding in the selection of damage mechanisms to be incorporated in the virtual test. Details of the composite microstructure follow.

Several views of the partially-processed composites are shown in Figs. 2.1

and 2.2 for the large and the small unit cell fabrics, respectively. The CVI process results in thin non-uniform coatings of SiC on the individual fibers within the tows and a relatively uniform 30–40 µm-thick matrix layer, or "jacket", around the tows. The gradient in SiC concentration within the tow is evident in Figure 2.1(e). Whereas the SiC coatings on the fibers are thick near the tow exterior, little SiC can be seen at the tow center (Fig. 2.2(e)). Evidently, pathways for material ingress seal off early in the processing cycle as CVI SiC builds up on the outer-most fibers, preventing SiC from infiltrating the center of the tow. Many cracks are observed in the SiC jacket both longitudinal and transverse to the tow directions. These are attributable to the mismatch in thermal expansion between the matrix and the fibers in combination with the temperature change following coating deposition.

Cross-sections of the fully-processed material are shown in Figs. 2.3 and 2.4 for the large and the small unit cell composites, respectively. One notable feature, evident in the higher magnification images, is the presence of cracks in the matrix at locations adjacent to transverse tows (indicated with arrows). As with the CVI SiC, the cracks in the slurry- and PIP-derived SiC are attributed to the thermal expansion mismatch between the fibers and the matrix. Some of these cracks are clearly open whereas others appear to have been filled during the PIP process. Evidently, some of the PIP material had also penetrated into the fiber tows (Fig. 2.5(c)), presumably via the cracks in the CVI SiC jacket.

It is heavily cracked as a result of the volume change which occurs during pyrolysis. Many large-scale (>100 µm) pores are also present, particularly in inter-tow regions near the mid-plane of the composites (Figs. 2.3(c&f) and 2.4(c&f)). These regions had likely been sealed off during one of the early PIP cycles, and the shrinkage cracks resulting from pyrolysis could not be filled with subsequent infiltrations.

The near-surface tows are coated in about 100 µm of SiC matrix. As a result the fully-processed composite panels measure ∼1.65 mm thick, with some variation due to surface roughness.

Fiber volume fractions were calculated from the manufacturers data on tow yield, the measured specimen thickness, the unit cell dimensions, and the cross-sectional area of the tows measured by Bale et al. (2012). The volume fraction of warp fibers is $f_{warp} = 11\,\%$ in both the large and the small unit cell composites. The volume fractions of the weft fibers are $f_{weft} = 15\,\%$ and $f_{weft} = 22\,\%$ in the large and the small unit cell composites, respectively. Within the tows the fiber volume fraction is much higher at 61 %. The remainder of the composite volume is divided between porosity, CVI SiC, and slurry- and PIP-derived matrix.

2.3 The virtual composite

2.3.1 Characterizing the tow architecture

The first step in creating a virtual representation of the material system described above was to perform a detailed characterization of the shapes and the paths of the tows by x-ray CT (Bale et al., 2012). Here a single unit cell of the partially-processed composite was imaged at a resolution of 8.8 µm/voxel. A sequence of 2D cross-sections was obtained along each of the in-plane tow directions. Individual tows were identified from each 2D section using a combination of manual and computational image segmentation techniques; the high-contrast boundary between the SiC-poor tow interior and the SiC jacket was used to define the tow surface. A typical section is shown in Figure 2.6; each segmented tow is individually colored.

After each tow was individually segmented, ellipses were fit to all out-of-plane tows in each section (also shown in Fig. 2.6). Several parameters were calculated from the ellipse fits to characterize the shape and the path of each tow (Bale et al., 2012): the centroid of each ellipse in (x, y, z) defines the tow path; the area and aspect ratio of the ellipse define the tow cross-section; and the in-plane tilt of the ellipse defines the rotation of the tow about its axis. This results in a rich set of data describing the changes in tow characteristics along

their length (Fig. 2.7).

Four instances of each tow type are found within the unit cell, and each instance of a tow within a population is related by translation. Using this relationship between tows, variation in tow shape characteristics was determined. Mean values and standard deviations of each geometric parameter were calculated at identical points in the period of each tow within a population. The results are couched in terms of the mean values of the geometric parameters for each of the four prototypical tow populations: warp, upper and lower surface weft, and center weft.

2.3.2 Creating a virtual geometry

The parameters obtained by x-ray CT are then used to construct a virtual geometry. This is done in two steps. In the first, outlined by Blacklock et al. (2012) and publicly available as a Mathematica® package (Blacklock et al., 2013), a 1D model of the tow paths is constructed for any given multiple of the unit cell size. The procedure to create the 1D model takes as input the mean geometry descriptors for each population of tows in a weave as well as the parameters that describe how the individual tows are arranged to form a weave. The latter include the number of tow types, the number of tows of each type, the number of tows in each coordinate direction, the unit cell dimensions, and

the number of unit cells desired in the virtual specimen. Translation vectors describing the positions of tows of a particular type in the unit cell are also required.

Each tow is generated by applying the specified translation vector to the coordinate points defining the mean tow of the corresponding tow type. The specified unit cell size defines periodic boundary conditions so that points can not be translated outside of the unit cell. All geometric parameters (*i.e.*, area and aspect ratio) associated with each point are retained. The procedure can be expanded to include the geometric variability characterized by Bale et al. (2012). In this instance, the parameters are determined by using a random number to select a value from a normal distribution. The normal distribution is defined by the experimentally-obtained mean and standard deviation of each parameter at each point in the tow.

The second step of geometry generation is to transform the 1D model to a set of 3D surfaces (Rinaldi et al., 2012). The 3D geometry generator uses the outputs of the 1D virtual specimen generator as well as an ordering matrix. The ordering matrix states, for any pair of tows, which tow should lie above the other in the z coordinate. The process begins by generating a grid of (x, y) coordinates of the 1D model. The ellipse defined by the geometric parameters of each tow is evaluated at each grid point to define an upper and lower z co-

ordinate for the tow. The tow surfaces are obtained by joining adjacent points within a tow with polygons. Since the position of the tow surface is only evaluated at each grid point, tows inevitably have flat rather than rounded edges. This may be minimized by refining the grid spacing.

One problem with this method is interpenetration of neighboring tows. This problem is rectified in one of two ways, depending on whether the interpenetration occurs in the in-plane or out-of-plane directions. When adjacent tows of the same tow type (*i.e.*, two warp tows) overlap in x or y, the edge of each tow is truncated at the mid-point of the overlapped region. This results in a flat edge on the tow (if it were initially smooth) and slight loss in cross-sectional area. Cross-sectional area is maintained by dilating the tow in the z coordinate; all grid points on the upper surface are moved upwards and all grid points on the lower surface are moved downwards. When two tows from different populations (*i.e.*, a warp and a weft tow) overlap in the z coordinate, the ordering matrix is used to determine which tow should lie above the other in the z coordinate. The two tows are then shifted away from each other by equal amounts at grid points where the two interpenetrate, without changing the thickness of each tow. This operation conserves the cross-sectional area of the tow. After these operations are performed on all interpenetrating tows, the model is checked for any additional tow overlap which may have been introduced through the process of resolving the initial interpenetration. The

procedure is repeated if necessary.

The final output of the 3D geometry generator is the set of fully-defined surfaces for each tow (Fig. 2.8(a&c)). This virtual specimen for the large unit cell fabric was generated with a grid spacing of 170 µm and 185 µm in the weft and warp directions, respectively. The cross-sectional tow shapes remain approximately elliptical. Cross-sections of the virtual specimen are compared to optical micrographs of the corresponding material for all three tow populations in Figure 2.9. The agreement is strong.

Although x-ray CT data was not available for the small unit cell composite, an attempt was made to generate a virtual model for this composite by adapting the geometry of the large unit cell model. To do so, the inputs to the 1D model for the large unit cell composite were modified in two ways. First, all y coordinates (corresponding to the warp direction) were scaled by the ratio of the unit cell sizes in the warp orientation. Second, the aspect ratios of the tow cross-sections were selected to be equal to the values measured from optical cross-sections. The cross-sectional area was kept constant. The resulting 3D model is shown in Figure 2.8(b&d). In comparison to the model of the large unit cell, the weft tows of the small unit cell have an irregular shape near the tow edges. Presumably this is because the elliptical shape used by the model does not taper in thickness as rapidly as the actual rhombic shape

near the tow edge, resulting in significant interpenetration between the weft and warp tows. As the interpenetration is resolved, the weft tow edges are shifted far enough in the z coordinate so as to appear irregular. Overall, the correspondence between the virtual model and actual material is deemed to be unsatisfactory.

2.4 Summary

Four variants of C/SiC composites of interest in the present study have been presented, covering two different states of matrix processing and two different unit cell sizes. The partially-processed composite with the large unit cell fabric was used to develop a virtual geometry; the geometry is used in subsequent chapters for calibration and validation of the virtual model. Sections of virtual geometry were found to be in good agreement with optical cross-sections of the composite.

An attempt to generate a virtual model for the small unit cell fabric by adjusting the geometric parameters of the large unit cell proved to be less successful. Here the weft tows in the virtual model were irregular in shape, and differed from those seen in the real composite. Because of this, the finite element calculations presented in subsequent chapters are restricted to the large unit cell composite. Ongoing work is focused on developing an alternative

mathematical description of the tow cross-section in the small unit cell fabric.

Table 2.1: Waviness of Tow Populations

	d (mm)	λ (mm)	d/λ
Small unit cell			
weft tows	0.11	5.1	0.021
warp tows	0.58	7.5	0.077
Large unit cell			
weft tows	0.08	5.1	0.016
warp tows	0.58	11.1	0.052

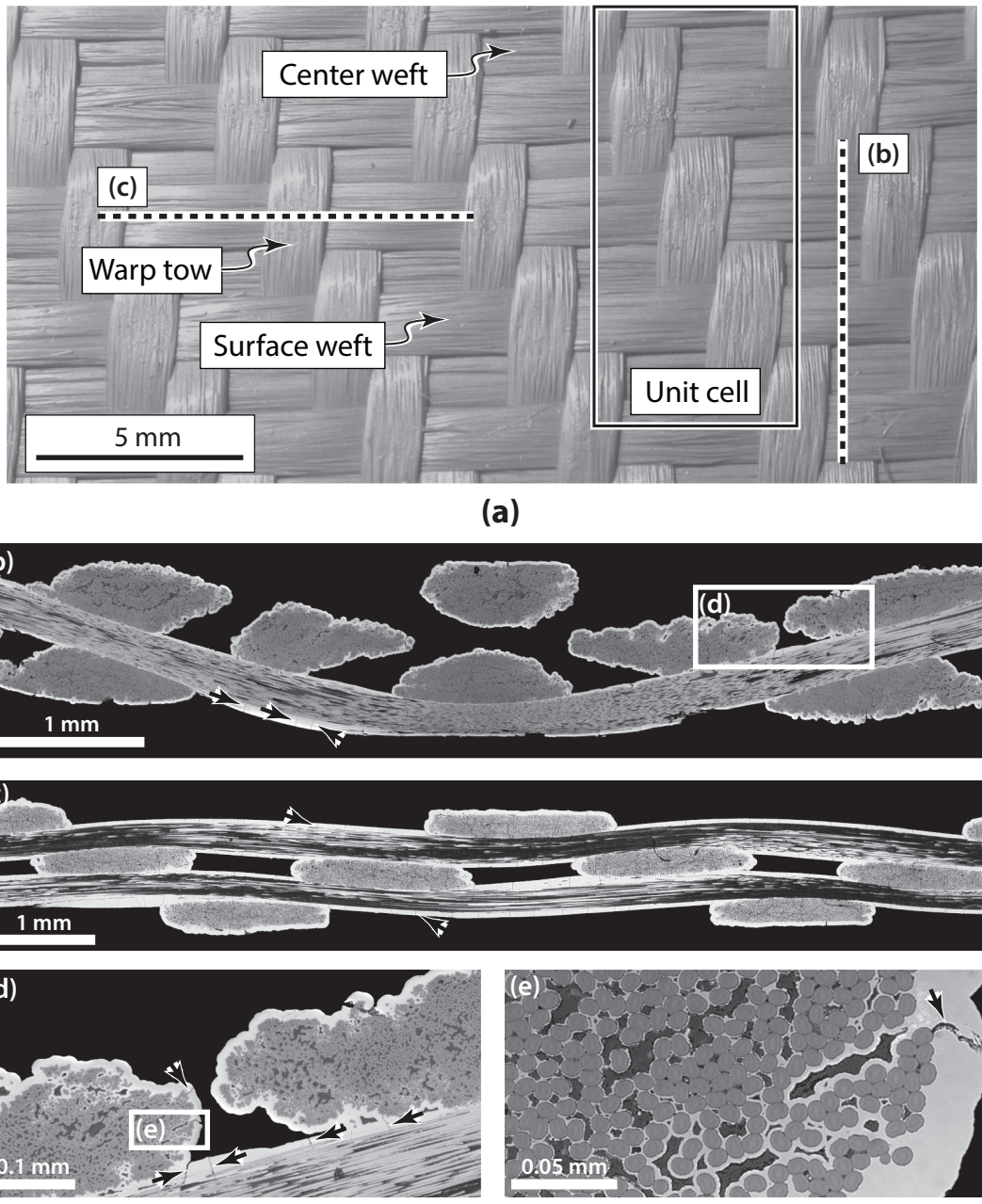

Figure 2.1: (a) Plan view of the woven large unit cell C/SiC composite, indicating the various tow genuses and the unit cell. The lines denote the locations at which subsequent sections (b&c) were obtained. Images (d&e) show the gradients in the thickness of the CVI SiC from the outside to the inside of the tow.

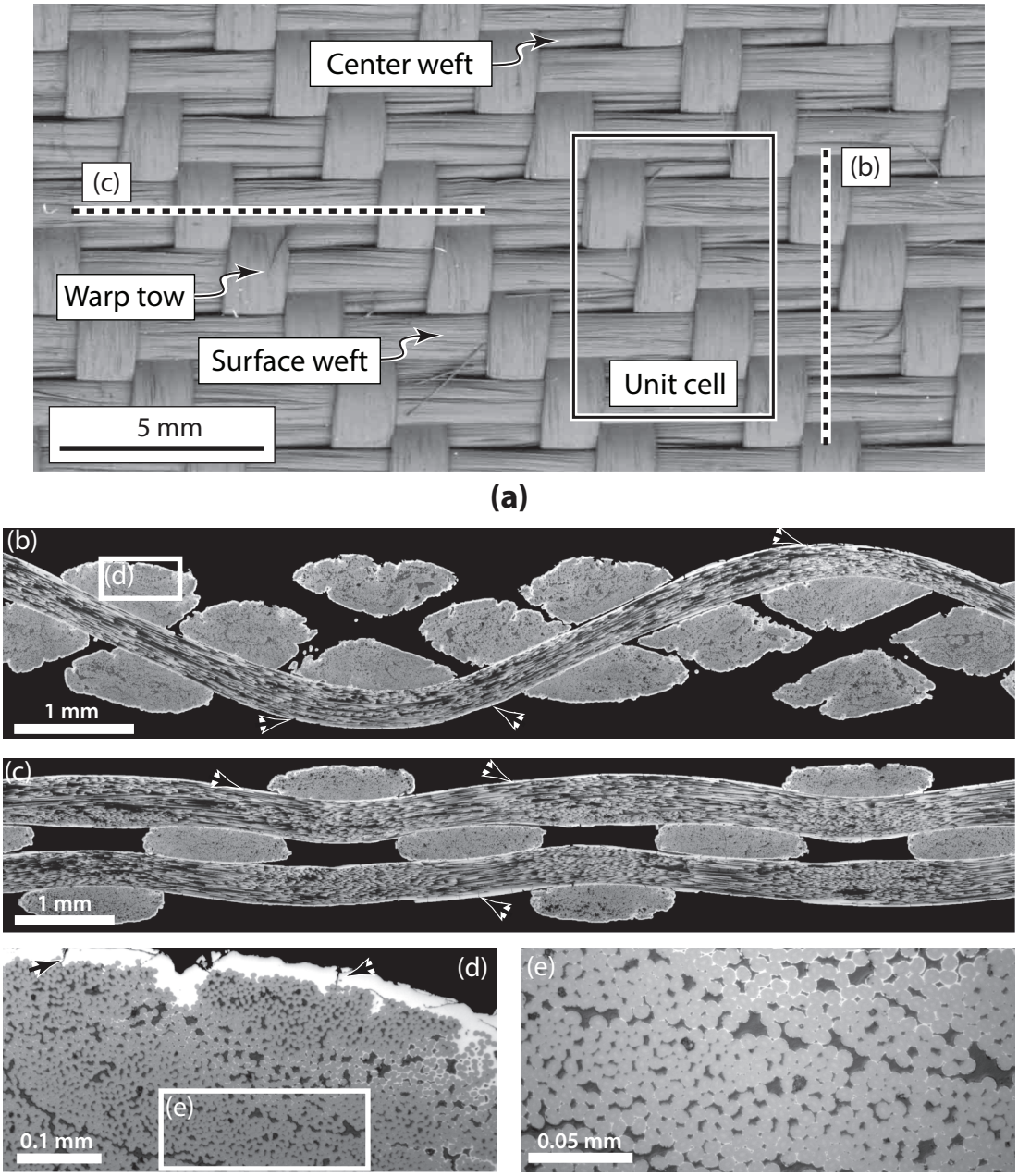

Figure 2.2: (a) Plan view of the woven small unit cell C/SiC composite, indicating the various tow genuses and the unit cell. The lines denote the locations at which subsequent sections (b&c) were obtained. Images (d&e) show the gradients in the thickness of the CVI SiC from the outside to the inside of the tow.

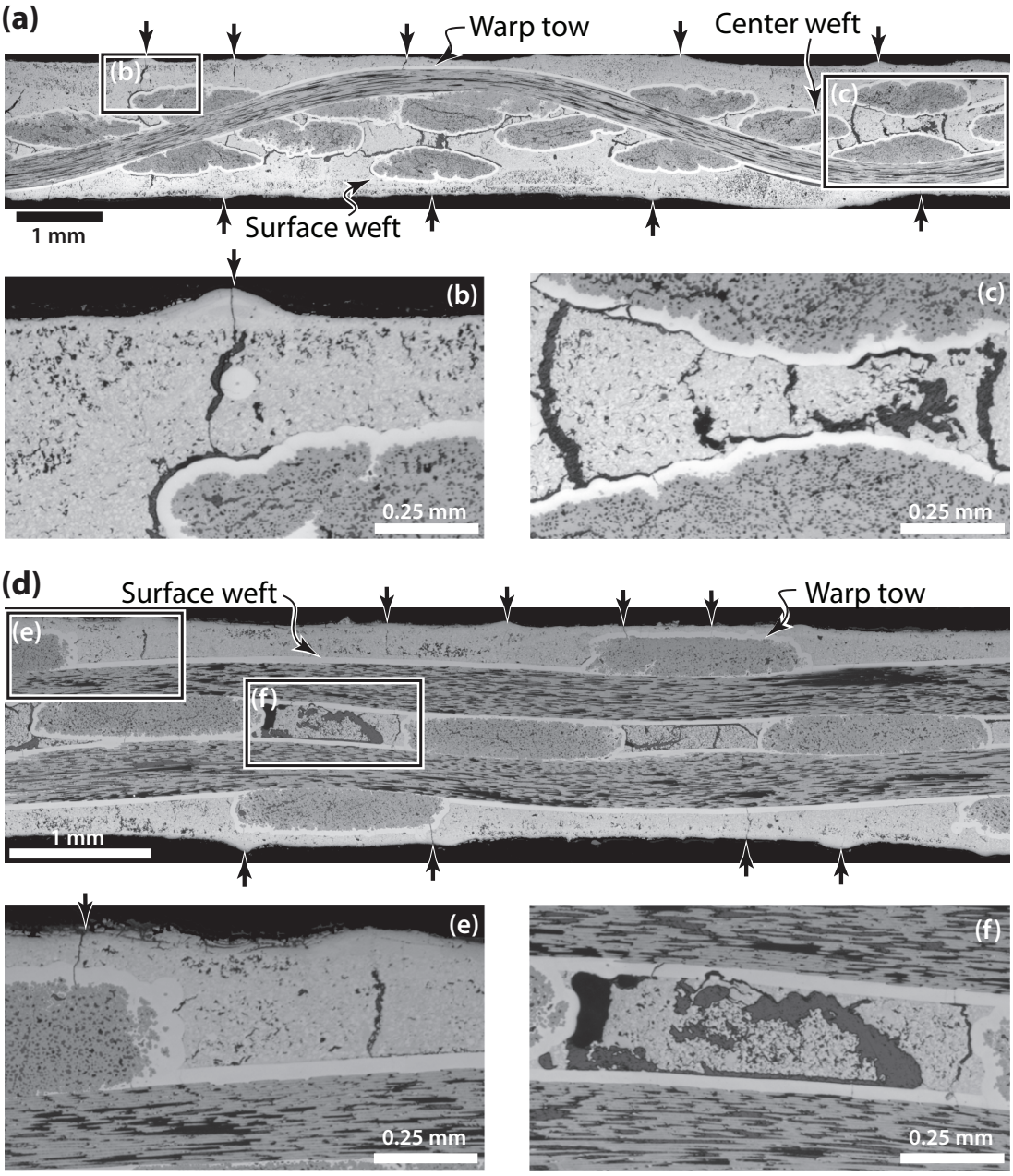

Figure 2.3: Optical micrographs of the large unit cell composite after final densification by slurry and PIP processing sectioned along the (a) warp and (d) weft directions. Arrows indicate locations of cracks intersecting the surface. (b,e) Closer views of surface cracks. (c,f) Large voids and apparent shrinkage cracks in the inter-tow regions.

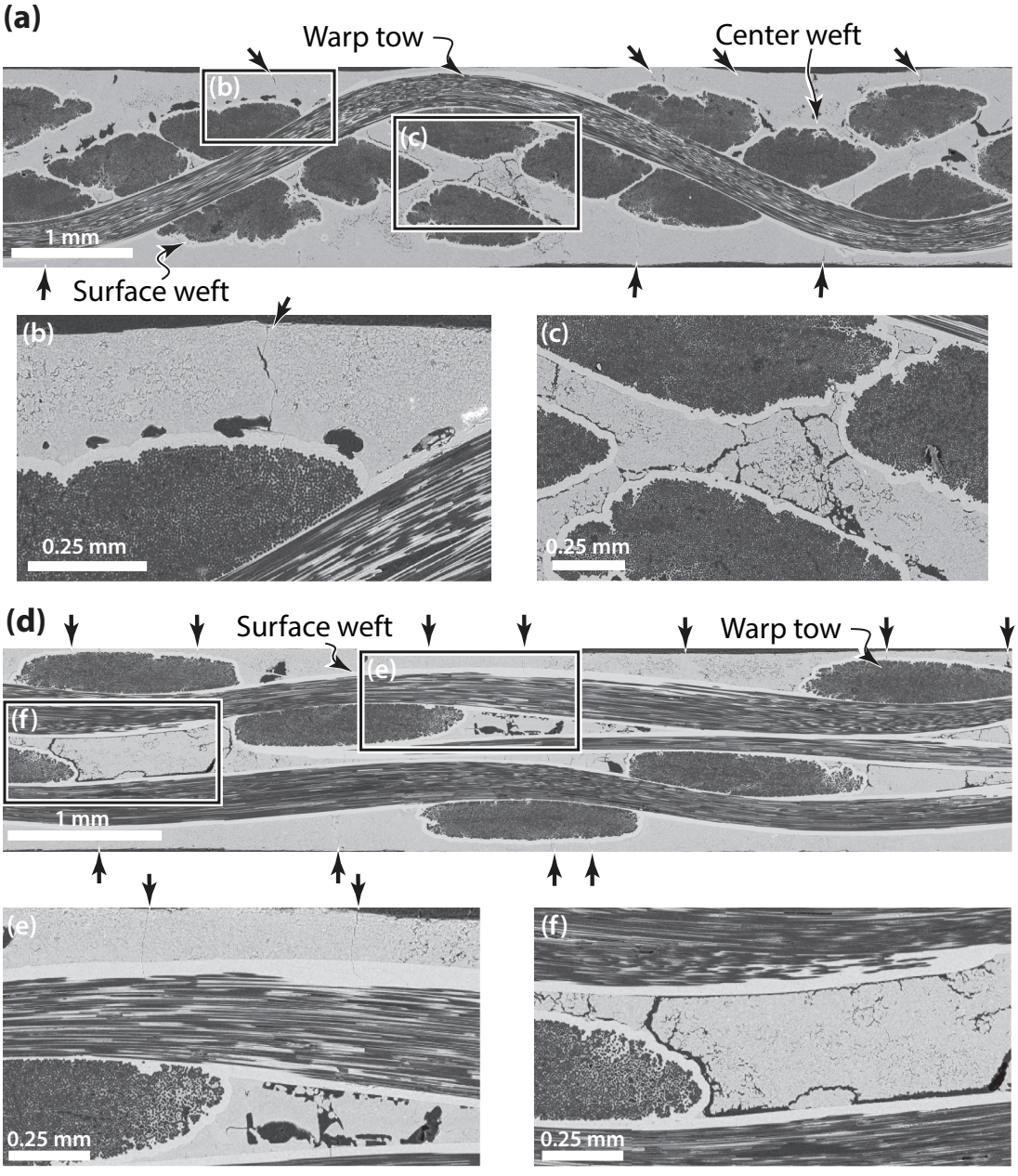

Figure 2.4: SEM micrographs of the small unit cell composite after final densification by slurry and PIP processing sectioned along the (a) warp and (d) weft directions. Arrows indicate locations of cracks intersecting the surface. (b,e) Closer views of surface cracks. (c,f) Large voids and apparent shrinkage cracks in the inter-tow regions.

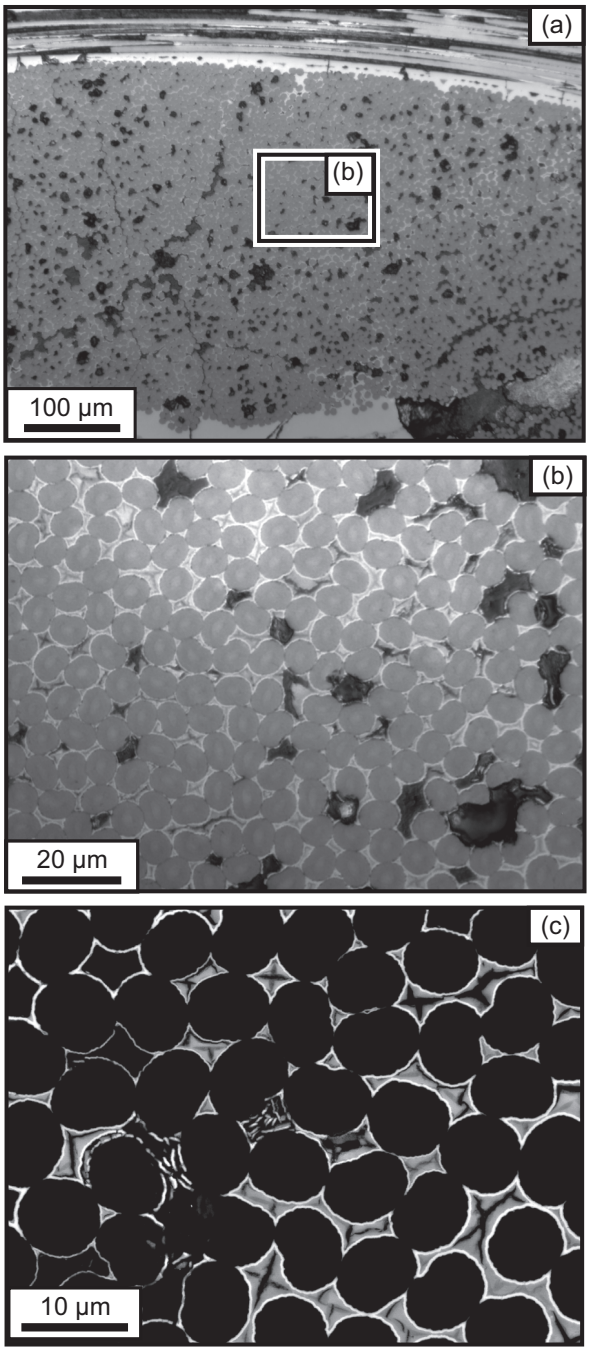

Figure 2.5: (a,b) Optical micrographs of the interior of a weft tow in the small unit cell composite. (c) PIP-derived SiC is visible within the tows in a higher resolution SEM micrograph of the tow interior.

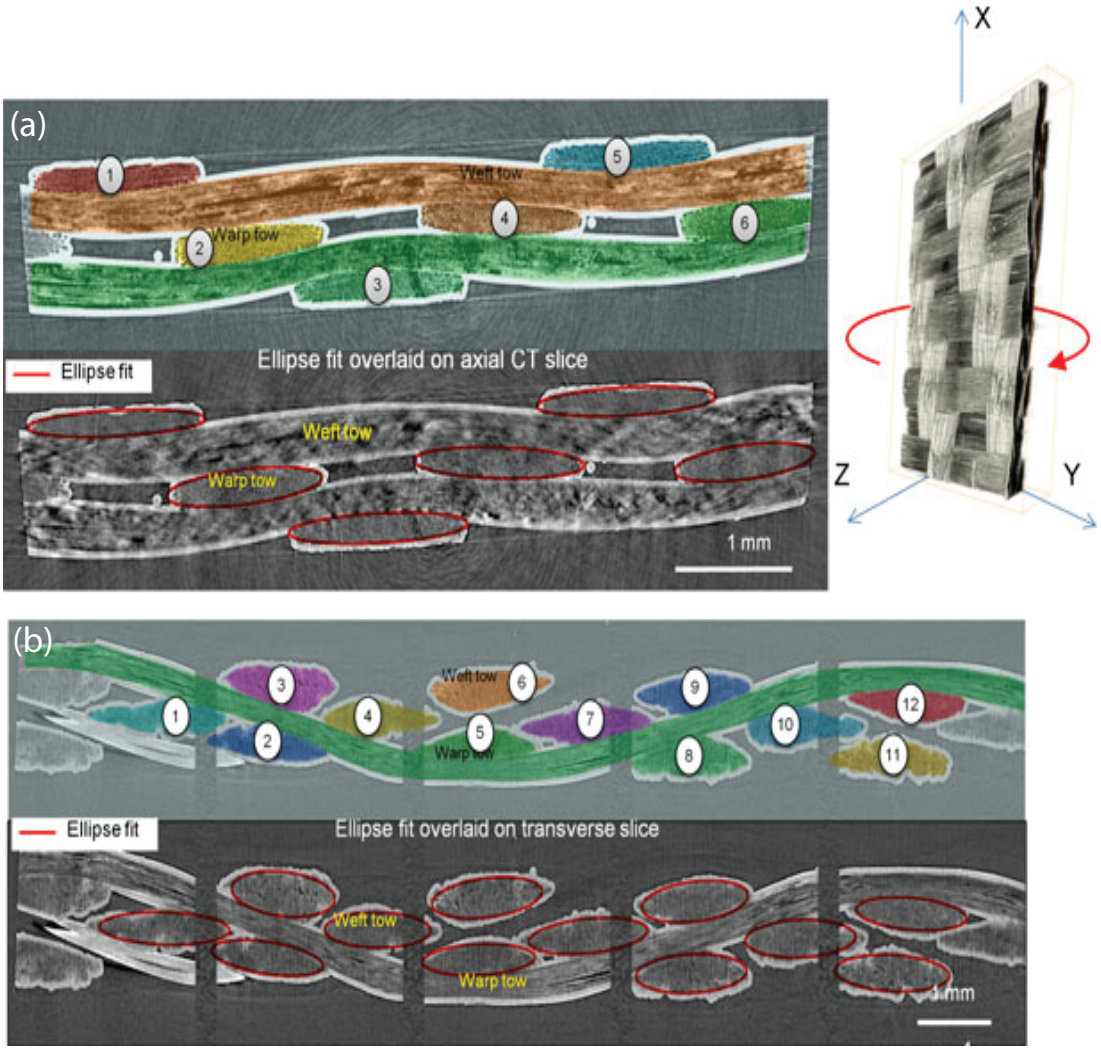

Figure 2.6: X-ray CT sections along the (a) weft and (b) warp directions. Colored areas represent individual tows identified by image segmentation procedures. Best-fit ellipses to out-of-plane tows are also indicated. (Bale et al., 2012)

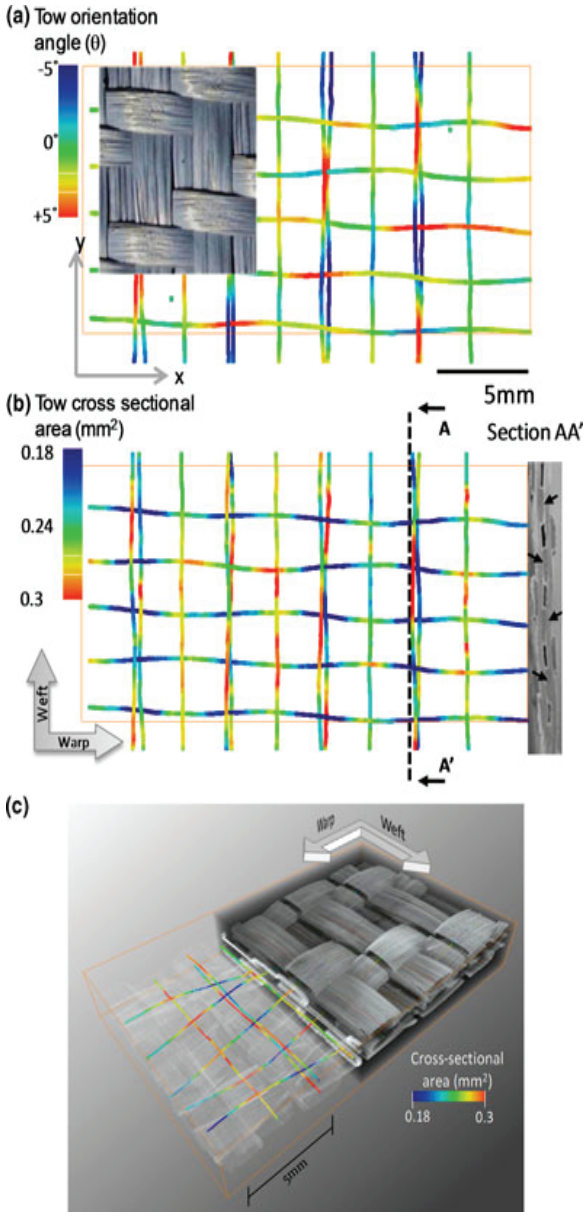

Figure 2.7: Spatial variation of the tow shape parameters for (a) orientation angle and (b) cross-sectional area plotted along the path of each tow. (c) Schematic representation of the relationship between tow shape parameters and the imaged structure. (Bale et al., 2012)

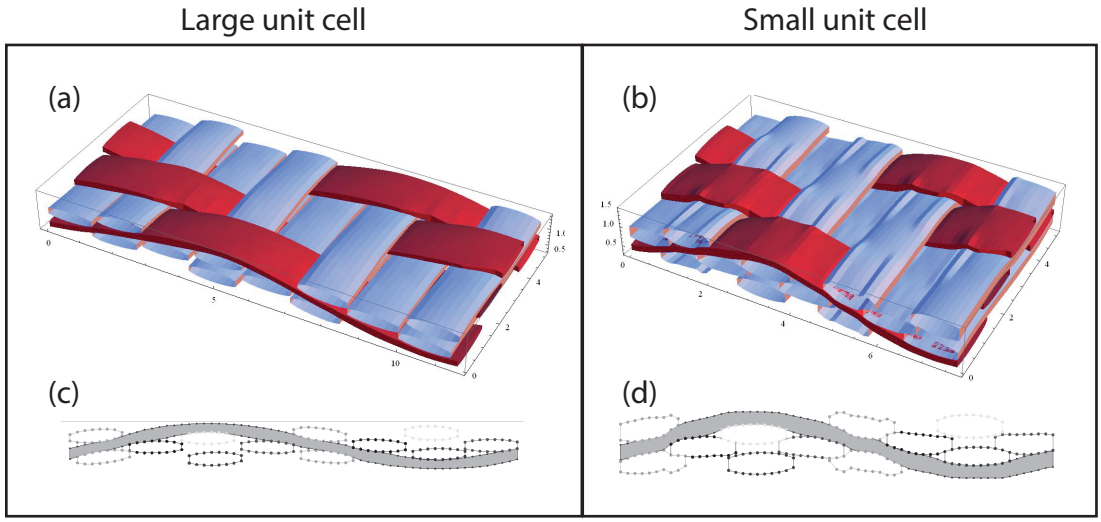

Figure 2.8: Virtual specimens generated for the (a) large and (b) small unit cell composites. Weft tows are plotted in blue; warp tows are plotted in red. (c&d) Representative section of the virtual geometry along a warp tow of (a) and (b), respectively, indicating final shape of the weft tows after completion of the interpenetration resolution algorithm.

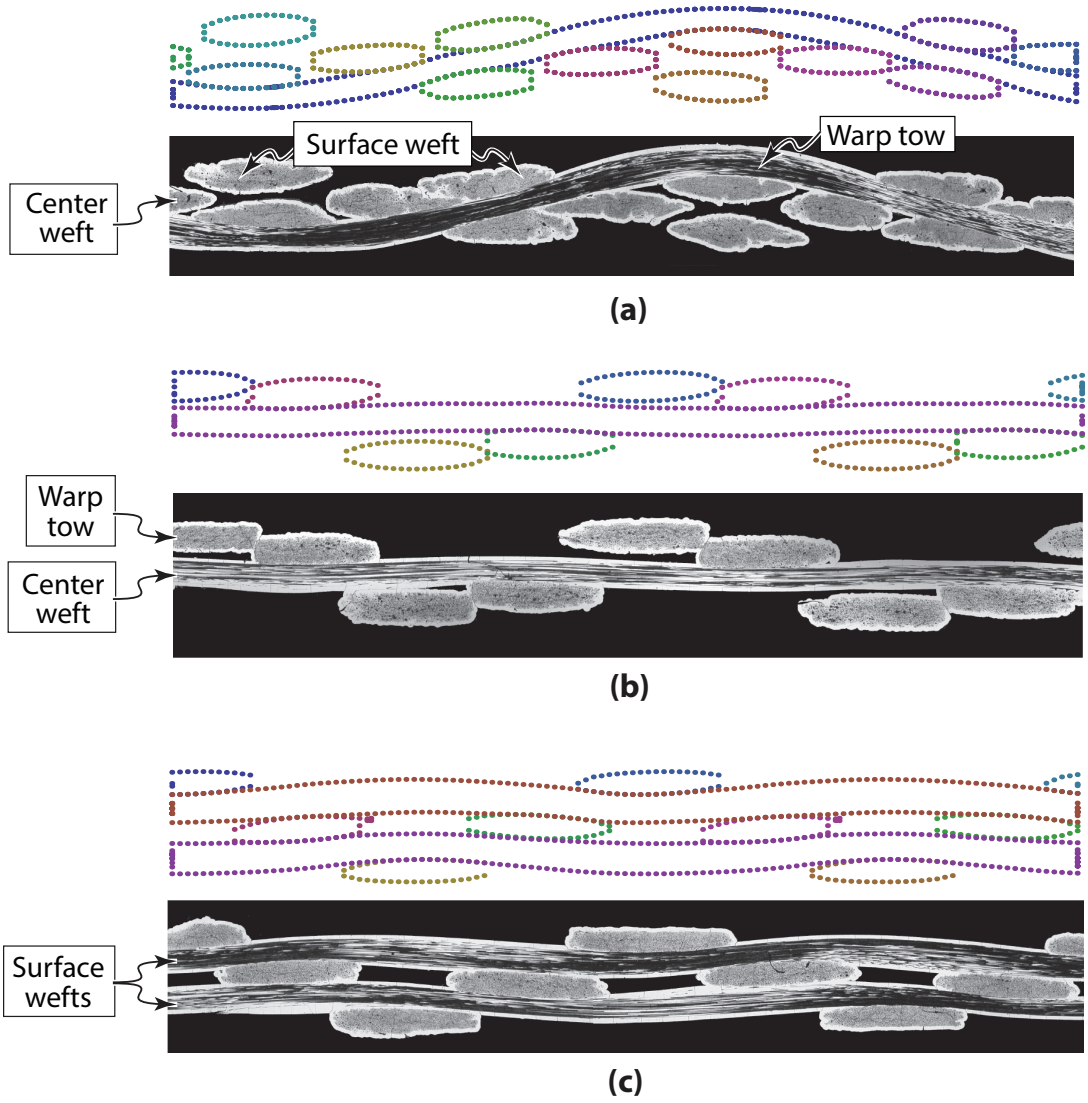

Figure 2.9: (a–c) Sections along each of the tow populations in the partially-processed large unit cell composite. Corresponding arrays of surface nodes defining the tow boundaries of the virtual model are plotted above the micrographs.

Chapter 3

Architecture-dependence of strains and damage under tensile loading

3.1 Introduction

As discussed in Chapter 1, a virtual test requires explicit knowledge of material properties and failure phenomena (Cox and Yang, 2006). This information must be obtained experimentally for the system being modeled. Several phenomena have been shown to occur in certain textile composites. Tow waviness has been shown to influence strength and stiffness of composites (Berbon et al., 2002; Cox and Dadkhah, 1995; Cox and Flanagan, 1997). Periodicity in full-field surface strains has been correlated with the underlying tow architec-

ture (Berbon et al., 2002; Daggumati et al., 2011; Ivanov et al., 2009; Qin et al., 2012; Rajan et al., 2012). The path of cracks has been shown to follow the tow architecture (Berbon et al., 2002; Chawla et al., 1998; Siron and Lamon, 1998).

Each of these phenomena need to be incorporated in a virtual model. Effects of tow waviness and periodicity in surface strains can only be captured if the tow path is explicitly represented. The virtual model introduced in Chapter 2 accounts for this by modeling the full 3D shape of each tow. One additional complexity is that the virtual model, as presently constructed, requires material properties for the tows. Since tows are transversely isotropic and their microstructure is complex, these properties are not readily predicted; they will need to be calibrated.

This study is a critical assessment of the properties and failure phenomena of the prototypical composite presented in Chapter 2. Local strain patterns and global stress-strain response are measured using digital image correlation (DIC) and correlated with fabric architecture. These experimentally-obtained strain measurements are used in combination with a virtual tensile test (developed by Blacklock et al. (2014a)) to calibrate elastic properties of the tows. Full-field strain measurements are also used to determine where, and when, matrix cracks initiate. Approximate analytical models are also used to rationalize effects of architecture on elastic response.

3.2 Experimental observations

3.2.1 Material and experimental methods

The four composites described in Chapter 2—fully- and partially-processed versions of the large and the small unit cell composite—were compared in a study of the effects of weave architecture on tensile response. Pertinent microstructural features are shown in Figures 2.1–2.5. The effects of warp tow shape and weft tow packing density on elastic and inelastic response were evaluated by comparing the response of the partially- and fully-processed composites. Specimens without a slurry- and PIP-derived matrix were used in combination with a virtual test to ascertain tow-scale material properties. The influence of fabric architecture on the initiation of matrix cracking was determined by monitoring surface damage on the fully-processed composites.

Test procedures

Dogbone-shaped tensile specimens were cut from all four composites along both the warp and the weft tow directions. Their gauge sections were 25.4 mm long and 12.7 mm wide. Fiberglass tabs were bonded to the ends of each specimen with epoxy. In preparation for strain mapping by digital image correlation (DIC), one face of each specimen was painted white; a black

speckle pattern was then created using an airbrush. The regions probed by DIC were 16–17 mm long (centered along the gauge length) and encompassed the full specimen width. The length of the region of interest represents at least one unit cell length in the warp direction and about three times the unit cell length in the weft direction. The resulting magnification of the DIC images was 7.1–8.3 µm/pixel. Successful correlation was obtained over the entire area of interest using a subset size of 43–45 pixels (320–360 µm). Two specimens of each type and orientation[1] were tested in uniaxial tension at a nominal strain rate of $1 \times 10^{-5}\,\mathrm{s}^{-1}$ at room temperature. All specimens failed within the gage section.

Strain analysis of the partially-processed material

Global axial strains were computed from displacement measurements made by DIC using linear fits of the axial displacement field $V(x, y)$ for all nodal locations within the correlated region. One potential problem with using the full displacement field is that the effect of a discontinuous surface (and the resulting loss of correlation at tow edges) on displacement measurements is unknown. To ensure that strains based on the displacement field were accurate, they were compared to strains calculated from virtual extensometers.

[1] Only one weft oriented specimen of the partially-processed, small unit cell composite was tested; the second specimen was damaged during machining.

Global extensometer strains were taken as the average of 3–4 virtual extensometers. The endpoints of the extensometers were positioned on an axial tow at identical points within the unit cell. For all weft oriented specimens, and warp oriented specimens of the small unit cell composite, the virtual extensometers were two unit cell dimensions in length. For the warp oriented specimens of the large unit cell composite the extensometers were one unit cell in length (the unit cell dimension is comparable to the size of the correlated region). Figure 3.1 compares the two methods of strain measurement for a warp oriented specimen with a small unit cell; there is excellent agreement between the two. For the purpose of comparison between the four composites, global strains of all specimens are calculated using their full displacement field.

Comparisons to the virtual model were made on the basis of two measurements. The first was lines of axial displacement V with respect to y. The second was average local strains. For this purpose contiguous visible segments of tow surface were identified for each tow population. Representative segments are shown in Figure 3.2 for a warp oriented specimen. A rectangular region was first drawn manually over the full visible region of an axial tow, or the region of a transverse tow directly above the axial tow. The rectangle is then retreated by half a subset size along each edge, to avoid any potential edge effects from data points lying near a surface discontinuity. The displacement field $V(x, y)$ is extracted from each region and the axial strain within the region is taken as

$\partial V / \partial y$.

Strain analysis of the fully-processed material

Global axial strains were calculated from the full displacement field as described above. These were found to be in good agreement with strains measured by axial virtual extensometers as well as the values obtained by averaging axial strains computed by the DIC software (VIC-3D 2010, Correlated Solutions Inc., Columbia, SC) at all nodal locations. At high applied stress, however, some discrepancies were found with the field-averaged strains. These discrepancies may be due to the presence of large cracks skewing the average strain upwards.

The DIC data were also used to characterize local deformation patterns associated with the fiber architecture. For this purpose, the data were analyzed as full-field strain maps over the entire correlated area, with strains computed at each nodal location from the measured displacements. Despite considerable smoothing of the preform surface after PIP processing, the underlying tiber tows could be discerned from topographic DIC data. The tow boundaries, obtained from the topographic data and from the optical scans of the preform after CVI, are subsequently superimposed on all strain maps. Regions of high strain ($> 1\,\%$) may be interpreted as cracks, as they are typically the result of

displacement discontinuities averaged over a gage length equal to the subset size (Rajan et al., 2012). In fact, the location of displacement discontinuities correlate very well with the locations of surface cracks in this material. A comparison of displacement fields in tensile specimens of the small, fully-processed composite with crack locations on the polished surface of the specimen after testing shows excellent agreement between the two (Fig. 3.3).

An alternative method of characterizing local deformation is to directly examine the displacement fields. Two approaches were used. The first was line scans of axial displacement V with axial position y. The location of cracks (apparent as displacement discontinuities) can be identified in this way as a function of applied load. The second approach tracks crack opening displacement (COD) explicitly using a procedure detailed by Rajan et al. (2012). A rectangular region known to contain a crack is first identified from contour plots of strain or displacement. Next, axial displacement data $V(x, y)$ is extracted from that region. For each value of x in the region, $V(y)$ is differentiated to find the maximum slope. The value of y at which this occurs is assumed to be the center-point of the displacement discontinuity y_{cen}. A threshold distance related to the subset size ($\sim 0.67 h_{sub}$) is used to separate the data into the region above the crack ($y > y_{cen} + 0.67 h_{sub}$) and below the crack ($y < y_{cen} - 0.67 h_{sub}$). Linear fits are made to the $V(y)$ data in these two regions. The two linear fits are evaluated at y_{cen}, and the difference between the two is taken as the COD.

This results in a data set of the form (x, COD) for each correlated image. The average value of the COD within the region is taken to be representative of the region as a whole.

3.2.2 Experimental results

Partially-processed composites

Under loading in the *warp* direction, the tensile stress-strain curves for test specimens of both composites are initially linear. The small unit cell composite has an initial Young's modulus of E =12 GPa; the modulus of the large unit cell composite is E =17 GPa (Fig. 3.4). There is some uncertainty in measuring the Young's modulus, as there are only 5–25 strain measurements in the elastic regime of each specimen (and all other specimens in this study). Interestingly, the modulus of the large unit cell composite is 50 % higher than that of the small unit cell composite even though the volume fraction of fibers oriented in the loading direction is identical. Evidently, the shape of the warp tow influences stiffness. The matrix cracking stress, σ_{MC}, of the composites is defined by a 0.05 % strain offset (ASTM Standard C1275, 2005) shown schematically in Figure 3.1. The matrix cracking stresses of the small and the large unit cell composites are $\sigma_{MC} = 43$ MPa and $\sigma_{MC} = 48$ MPa, respectively.

After the onset of nonlinearity, composites of both unit cell sizes have a tan-

gent modulus of approximately zero. Their negligible stiffness suggests that deformation is dominated by straightening of the warp tows. Tow straightening would likely be resisted by frictional forces between the weft and the warp tows, allowing the composite to bear load. The maximum expected strain from straightening of the warp tows is given by $\varepsilon = 1 - s/\lambda$, where s is the path length of the tow and λ is its wavelength. The path length of a continuous function $y(x)$ between points a and b in its domain is given by the integral:

$$s = \int_a^b \sqrt{1 + \left(\frac{\mathrm{d}y}{\mathrm{d}x}\right)^2}\,\mathrm{d}x \tag{3.1}$$

Assuming that the path of a warp tow is approximately sinusoidal with a wavelength λ in the x direction and an amplitude d in the y direction, it may be described by the equation:

$$y = d \sin\left(\frac{2\pi x}{\lambda}\right) \tag{3.2}$$

Substituting equation 3.2 into equation 3.1 yields the path length s of a tow over its period λ:

$$s = \int_0^\lambda \lambda^{-1}\sqrt{\lambda^2 + 4d^2\pi^2\cos^2(2\pi x/\lambda)}\,\mathrm{d}x \tag{3.3}$$

Using the values of d and λ for the warp tows of each composite (Table 2.1) the maximum extensional strain is 2.6 % and 5.7 % for the large and the small unit cell composites, respectively. These values are much larger than the failure strains of the composites. Interestingly, the small unit cell composite fails at a lower strain despite the larger potential extensional strain.

When loaded in the *weft* direction composites of both unit cell sizes are much stiffer than in the warp direction (Fig. 3.4). The specimen of the small unit cell composite had an initial Young's modulus of $E = 64\,\text{GPa}$, a matrix cracking stress of $\sigma_{MC} = 93\,\text{MPa}$ and a terminal tangent modulus of 28 GPa. The average Young's modulus of the specimens of the large unit cell composite was $E = 32\,\text{GPa}$. They had no apparent nonlinearity.

By comparison, the modulus calculated on the basis of the volume fraction of weft tows (assumed to be straight) and the reported modulus of T300 fibers ($E_f = 231\,\text{GPa}$) is $f_{weft}E_f = 35\,\text{GPa}$ for the large unit cell composite and $f_{weft}E_f = 51\,\text{GPa}$ for the small unit cell composite. Evidently, the response of the large unit cell composite is dominated by the fibers. In contrast, the terminal tangent modulus of the small unit cell composite is much lower than the expected fiber contribution. Additionally, the fiber bundle strength, taken as σ_{ult}/f_{weft} (σ_{ult} being the ultimate strength), is 1.3 GPa and 1.5 GPa for the small and the large unit cell composites, respectively (Fig. 3.5). The bundle strength of the large unit cell composite is in close agreement with the reported bundle strength of T300 fibers ($1.8 \pm 0.2\,\text{GPa}$) (R'Mili et al., 1996). These two discrepancies between the large and the small unit cell composites suggest that the test on the small unit cell composite specimen was invalid. One possibility is that the close packing of the tows in the small unit cell fabric (Fig. 2.2) inhibited infiltration of epoxy to the specimen interior when the specimens were

tabbed. This may have prevented load transfer to the central weft tows, thus reducing the apparent stiffness of the specimen.

Local strains were calculated for the large unit cell specimens loaded in the warp and the weft direction using the procedure outlined above (Fig. 3.6). In both loading directions the average strain in each population of tow segments is less than the global strain. This may be attributed to two different mechanisms, depending on whether a given population of tows is aligned with the loading direction. For tows aligned to the loading direction the lower segment strains (relative to the global strain) are attributed to tow waviness. Both populations of tows are sinusoidal in shape, and the correlated surface only includes convex surfaces of tows. Thus, there is a compressive strain component on the visible surface due to bending. For tows transverse to the loading direction the lower segment strains are attributed to poor load transfer between the axial and transverse tows. The CVI SiC coating bonding the tows together is thin and likely breaks early in the test.

Fully-processed composites

Under loading in the *weft* direction, the tensile stress-strain curves for test specimens of the small unit cell composite are initially approximately linear with a Young's modulus of E =103–113 GPa (Fig. 3.4). The matrix cracking

stress of this composite is ∼115 MPa. Beyond the matrix cracking stress and through to fracture, the response is again approximately linear with a tangent modulus of 42 GPa. The corresponding values for the large unit cell composite are an initial linear regime of E =74–90 GPa, a matrix cracking stress of 83 MPa and a terminal tangent modulus of 33 GPa.

In both composites the measured terminal terminal tangent modulus is comparable to the fiber contributions calculated above. The inference is that the matrix has attained a nearly fully-damaged state that precludes significant additional load transfer from the fibers to the matrix (Budiansky et al., 1986). Additionally, the fiber bundle strength at fracture is in close agreement with the reported bundle strength of T300 fibers for both composites (Fig. 3.5).

The stress-strain response in the *warp* direction (Fig. 3.4) is more compliant (E =60–65 GPa for both composites), owing mainly to the lower fiber volume fraction in this direction (11 % in the warp direction vs. 15 % or 22 % in the weft direction). The matrix cracking stress is ∼50 MPa for both composites. A second nearly-linear domain is obtained at stresses above the matrix cracking stress. The terminal tangent modulus is 17 GPa and 13 GPa for the large and the small unit cell composites, respectively. Assuming that the fibers are initially straight, the expected fiber contribution is $f_{warp}E_f$ = 23 GPa for both composites. As a proportion of the expected fiber contribution, neither com-

posite's terminal tangent modulus is as high in the warp direction as in the weft direction. This suggests that the matrix undergoes progressive damage and/or the undulating warp tows undergo some straightening. Interestingly, the terminal tangent moduli are approximately equal to the Young's moduli of the partially-processed composites. Evidently the inelastic response of the composites in the warp orientation is also governed by the elastic response of the tows (as was observed in the weft orientation).

Furthermore, the inferred fiber bundle strength (σ_{ult}/f_{warp}) in the small unit cell composite is only 1.0 GPa (about half that obtained in the weft direction) and the composite fracture strain is significantly lower than that obtained in the weft direction (0.6 % vs 0.8 %). By comparison, the inferred fiber bundle strength in the large unit cell composite is 1.3 GPa with a fracture strain of 0.75 %. The lower values of fracture strain and fiber bundle strength in the warp direction relative to the weft are tentatively attributed to bending loads imparted to the warp tows as these tows attempt to straighten. The lower fracture strain and fiber bundle strength measured for the small unit cell composite, which has a higher level of tow waviness, supports this theory.

Matrix cracking in the fully-processed composites

Full-field maps of axial strain $\varepsilon_{yy}(x, y)$ at three global strain levels are shown in Figure 3.7. In both orientations, the strains exhibit distinct periodic banded patterns. They are characterized by narrow bands of high apparent strain (well over 1 %) and intervening regions with negligible strain. However, the width of the high-strain regions ($\sim$ 300 µm) is comparable to the subset size used for correlating the DIC data. As discussed earlier, this indicates that the strain concentrations are in fact cracks. In both composites and orientations, cracks appear to initiate over transverse tows and are present even at low global strains. At higher global strains the cracks appear to extend horizontally and bifurcate. Since average surface strains are dependent on the location of cracks and their COD, average strains over regions corresponding to architectural features were not calculated as they were for the partially-processed material.

Displacement discontinuities are seen more vividly in line scans of axial displacements $V(y)$ shown in Figure 3.8 for the small unit cell composite. The scans reveal regions of constant displacement (corresponding to the unstrained regions in Fig. 3.7) bounded by regions over which the displacement changes from one level to another over a distance comparable to the correlation subset size. Also shown in Figure 3.8 are shaded bands indicating the

inferred locations of matrix cracks. They are broadly categorized as being either pre-existing (determined to be such if the displacement discontinuity was evident from the onset of loading) or as being formed during loading. The former are indicated by the pink-shaded rectangles and the latter by the yellow-shaded rectangles; their width represents the correlation subset size.

This interpretation of the displacement scans was confirmed by micrographs of polished longitudinal cross-sections following testing, also shown in Figure 3.8. Each displacement jump correlates with a crack seen in the micrograph at the same location, as indicated on the figures. Furthermore, the locations of the cracks seen in the tested specimens appear to correlate well with the locations of cracks or incipient (filled) cracks evident in cross-sections of pristine material, shown in Figure 2.4. The micrographs also show that the cracks propagate along the tow-matrix boundary. This is particularly true in the region near the fracture plane.

A closer examination of the development of cracking was conducted by tracking COD in the manner outlined previously. In one instance, several cracks were identified from a full-field strain map in the elastic regime of the fully-processed, large unit cell composite (Fig. 3.9(a)). These cracks appear to initiate almost immediately upon loading; positive COD is calculated below the matrix cracking stress and the curves extrapolate to the origin. Additional

cracks were then identified that were not present in the elastic regime (Fig. 3.9(b)). The calculated COD for this group of cracks is zero below ∼50 MPa. Most show an abrupt increase in COD at stresses clustering around the matrix cracking stress. Evidently, the onset of nonlinearity is characterized by the bifurcation or extension of existing cracks. This is consistent with the development of cracking shown in Figure 3.8; some cracks are present initially, but the number of cracks increases above the matrix cracking stress and remains relatively stable through to fracture.

3.3 Virtual test

Virtual tensile tests of the partially-processed, large unit cell composite were developed by Blacklock et al. (2014a) to calibrate tow elastic properties. A summary of the methods and results of the study follows.

3.3.1 Specimen and mesh generation

Virtual specimens were created using the procedure outlined in Chapter 2. The models employed in the present study included only the mean tow geometry parameters. One specimen was generated in each loading direction with dimensions identical to the gage section of the dogbones used for the

tensile tests.

Using the three-dimensional surface profile for each tow (consisting of triangular facets joined together to form a continuous surface), solid three-dimensional meshes comprising four-noded tetrahedral elements were generated using *TetGen* (Version 1.4.3) (Hang). This meshing algorithm allows specification of constraints on element volume and aspect ratio, thereby facilitating construction of a range of numerically feasible meshes with varying degrees of mesh refinement. The output from *TetGen* is an array of (x, y, z) nodal points and a list of element nodes describing tetrahedrons for each tow. Each tow is meshed individually and can be collated into a single model mesh for use in FE simulations. Tow interactions are governed by prescribed contact conditions, as described below. Surface topography was compared for physical and virtual warp specimens (Fig. 3.10); there is strong agreement between the two. The slight discrepancies are due in part to the elliptical idealization of the tow cross section in the translation of the CT images into the virtual sample (Bale et al., 2012). Some error also derives from the fact that stochastic variation in the geometric parameters was not included in the virtual model.

Finite element simulations were conducted in ABAQUS Standard (Version 6.9-EF1; Dassault Systèmes, Vélizy-Villacoublay, France). Following a successful mesh convergence study, meshes comprising 2.4×10^6 and 5.6×10^5 first-

order tetrahedral elements (C3D4) were used in the warp and the weft loading directions, respectively. For each element, a local coordinate system was defined so that the 1-direction was aligned with the local trajectory of the tow.

Displacement boundary conditions were used to simulate the tensile test. All nodes on the bottom face ($y = 0$) of the tensile specimen were constrained from displacing axially ($v = 0$); those on the top face ($y = 25.4$) were incrementally displaced. To prevent rigid body motion of the entire specimen, off-axis degrees of freedom for the central node on the top and bottom faces were constrained ($u = w = 0$). Surface-to-surface interactions were specified between neighboring tows to capture the effect of the SiC matrix (discussed at greater length below).

3.3.2 Constitutive behavior

The strains are assumed to be elastic and, because of symmetry, the tows are treated as being transversely isotropic. For consistency with previous descriptions of the microstructure (Bale et al., 2012), the tow surface is taken to be the interior surface of the SiC jacket. The jacket material and the SiC within the tow interior are homogenized and represented by an effective medium that yields the same tow response. As the model only captures the architecture of the composite at the tow-scale, fine-scale microstructural features within the

tows are ignored. The elastic constants of the tows were estimated using a combination of micromechanical models (Christensen and Lo, 1979; Hashin, 1979; Hashin and Rosen, 1964), mechanical tests, and FE simulations. The models are based on the assumption that each tow comprises unidirectionally aligned fibers in an effective medium that embodies the properties of the SiC and the intratow porosity. The effective medium properties were determined through comparisons of virtual tests of uniaxial tensile loading with corresponding experimental measurements. The models and calibration procedures are detailed in Appendix A. The resulting elastic constants are summarized in Table 3.1.

3.3.3 Tow contacts and interactions

As evident in the micrographs in Figures 2.1 and 2.9, the individual tows are connected to their neighbors only in select regions. For instance, in Figure 2.9(a), the surface wefts situated directly across from the crowns of the warp tows are not connected to the other tows in the plane of this section. The remaining wefts exhibit some contact with both the warp tows and the neighboring wefts. In another case (Fig. 2.9(c)), in a section taken along the weft direction through the center of a surface weft, the warp tows are in intimate contact with the weft tows. In contrast, in parallel sections away from

the weft mid-line (Fig. 2.9(b)), the outermost warp tows make minimal contact with the wefts. These contacts were treated in the FE simulations using two approaches, intended to bound the realistic range of expected behavior.

In the first, the contacting regions between warp and weft tows were treated as being unbonded and constrained from moving only by normal forces between the tows: a limiting condition that would be obtained if all interfaces between tows were cracked. A friction coefficient of 0 was chosen to model this contact condition. In the second, the tie interaction property in Abaqus was used between the nodes on the surfaces of the warp and weft tows, simulating a perfectly bonded interface. This interaction property takes as an argument a threshold nodal separation distance, hereafter referred to as the tie tolerance, below which any pair of nodes is considered to be rigidly attached throughout the simulation. A tie tolerance of 1–5 μm was used in the simulations presented here.

3.3.4 Virtual test vs experimental results

The global response of the composite was captured well once the effective medium properties were calibrated (Fig. A.1). At this stage, further comparison between the average local strains of tow populations may serve to validate the model's assumption that strain heterogeneity is explained by the weave

geometry. A representative line scan of axial displacement of a warp-oriented specimen is shown in Figure 3.10(b). Displacements are approximately linear within a tow segment; sharp discontinuities are present at the boundaries of different tow segments. The discontinuities in displacement are present because the surface itself is discontinuous; individual weft tows move away from each other during the test. The model captures this well. However, there is some discrepancy in the strains measured within the tow.

Calculated local strains for each population of tow segments in the warp- and weft-oriented specimens are shown in Figure 3.6. In these simulations tow interaction was represented with tied surfaces. As in the experimental data, all populations of tow segments have a lower average strain than the macroscopic strain. Strain variation within a given population is captured well by the virtual model; it is almost identical to the variation observed in experiments in the warp orientation. There is, however, a discrepancy between the average calculated and measured strains in all tow populations. In both loading directions the calculated average strain in axial tows is too high. One potential reason for this is that the interaction between the warp and the weft tows is too strong.

In the warp loading direction the model with frictionless contact was unstable and no results were obtained. In the weft loading direction the friction-

less model ran successfully (Fig. 3.11). Frictionless contact has two effects on strain populations. For one, there is much stronger agreement between the average values of strains in the simulations and the experiments. The second effect is a reduction in strain variation within each population of segments. The computed strain variation is now much smaller than the measured strain variation.

The results from the weft and the warp loadings suggest that interaction between the tows is approximately frictionless. Furthermore, the fact that the simulations capture strain variation within a given population of segments suggests that one component of the variation is the geometry of the tows. If variation in tow geometry were to be included in the model, a simulation with frictionless contact may be in even closer agreement with experimental results. This remains an area for future study.

3.4 Analysis and Discussion

3.4.1 Elastic regime

The global response of the *partially-processed* composites loaded in the weft direction indicate that they are approximately elastic up until fracture. In the warp direction, however, the large and the small unit cell composites exhibit a

50 % difference in their Young's moduli despite having an equal volume fraction of fibers oriented in the loading direction. One approach to understanding this difference in moduli is to approximate the warp tows as curved beams with finite bending stiffness. That is, under an applied load some component of the macroscopic composite strain is due to straightening of the curved warp tows.

González and LLorca (2005) have developed an applicable model to compute the axial stiffness of a curved beam. The model considers a load applied to one end of a beam with initial radius of curvature R_0, initial length l_0, height h and thickness b. The beam is assumed to be isotropic with Young's modulus E. To apply this model to the warp tows, the warp tows were approximated as beams with initial length $l_0 = \lambda/4$ (Fig. 3.12). Their initial radius of curvature was determined by fitting one quarter of their period to a circle. The cross-sectional shape of the tows was determined from the micrographs and x-ray CT data presented in Chapter 2. The axial Young's modulus of the tows is assumed to be 179 GPa, as calculated by the virtual test.

The derivation of the model is lengthy and is therefore not reproduced here. Operationally, an applied load is specified and used to determine the angle of the curved end of the beam θ_l relative to the x axis. Once determined, this angle is used to solve for the extension at the end-point of the beam. Re-

peating this procedure for the two warp wavelengths in the present composites yields the axial response of each. The calculated stress-strain response for the composites is shown in Figure 3.13. The predicted reduction in modulus due to tow waviness (relative to the expected fiber contribution) is $\sim$50 % for both warp tow wavelengths. This is approximately the reduction observed experimentally for the small unit cell composite. The large unit cell composite is calculated to be stiffer than the small unit cell composite, but the increased stiffness is negligible below strains of 1 %. Evidently, the increased stiffness of the large unit cell composite is not explained solely by the geometry of the warp tow. Weft tows may resist the straightening of the warp tows, but it is unclear why this effect would be larger for the large unit cell composite.

The elastic response of the *fully-processed* composites may be interpreted with an analysis based on classical laminate theory. Here the material is idealized as a symmetric, unbalanced laminate in which the fiber volume fraction is the same in each ply (33 % and 26 % in the small and the large unit cell composites) and the ratio of ply thicknesses equals the ratio of fiber volume fractions in the warp and weft directions. In the small unit cell composite ($f_{weft} = 22\,\%$ and $f_{warp} = 11\,\%$) the plies representing the weft tows are twice as thick as those of the warp tows. In the large unit cell composite ($f_{weft} = 15\,\%$ and $f_{warp} = 11\,\%$) the plies representing the weft tows are 36 % thicker than those of the warp tows. The elastic properties of the fibers are well-established and

are summarized in Table A.1. The matrix Youngs modulus E_m is treated as a variable; the porous nature of the matrix precludes accurate prediction of its modulus. Details of the analysis are presented in Appendix B.

Operationally, the matrix modulus is first inferred by fitting the prediction of a model for a cross-ply laminate to the measured Youngs modulus of the small unit cell composite in the weft direction; this yields $E_m = 80\,\text{GPa}$. Following this calibration (with estimates of all constituent properties in hand), the modulus in the warp direction is calculated for the same idealized laminate. The procedure is repeated for the large unit cell composite, assuming the same matrix modulus.

Applying the procedure to weft-oriented loading yields composite Youngs moduli of 103.0 GPa and 92.0 GPa in the small and the large unit cell composites, respectively. Although the matrix modulus of the large unit cell composite was not calibrated, it is in close agreement with the measured modulus.

Applying the procedure to loading in the warp direction yields essentially the same conclusion, but with one complication. Here the predicted Youngs moduli in the small and the large unit cell composites are 74.8 GPa and 81.7 GPa, respectively. But, because of tow waviness, the predictions overestimate the measured moduli (60–65 GPa) by a significant margin. Analyses of tow waviness effects on axial stiffness have been presented in earlier ar-

ticles, focused on polymer matrix composites (Cox and Dadkhah, 1995; Cox and Flanagan, 1997). The analyses show that, when the axial tows follow a sinusoidal trajectory with amplitude d and wavelength λ, the ratio η of the modulus of the wavy tow to that of a straight tow is given by:

$$\eta = \left\{ 1 + 2 \left(\frac{\pi d}{\lambda} \right)^2 \left[\frac{E_x}{G_{xy}} - 2(1 + \nu_{xy}) \right] \right\}^{-1} \tag{3.4}$$

where E_x, G_{xy}, and ν_{xy} are the elastic properties of the tow. Applying this result to the notional cross-ply material yields a composite modulus E_C in the warp direction of:

$$E_C = \phi E_{weft} + \eta(1 - \phi) E_{warp} \tag{3.5}$$

where

$$\phi = f_{weft} / (f_{weft} + f_{warp}) \tag{3.6}$$

Using the properties of the straight tows obtained from the virtual test (Table 3.1) and the geometric characteristics of the warp tows (Table 2.1), the calculated values of η are 0.83 and 0.70 for the large and the small unit cell composites, respectively. When the knockdown factor is applied to the warp ply of each composite, the predicted composite moduli become $E_C \approx 62\,\text{GPa}$ and $E_C \approx 73\,\text{GPa}$ for the small and the large unit cell composites, respectively. These are in much closer agreement with the measured moduli of the composites. The calculated value of η for the weft tows is approximately 0.97 (for $d/\lambda = 0.02$); due to the negligible effect of tow waviness in this orientation,

the knockdown factor was omitted for the weft plies.

3.4.2 Inelastic regime

In the *partially-processed* composites loaded in the weft direction there is essentially no inelastic regime. For composites loaded in the warp direction, as discussed above, the response is approximately linear with zero modulus after the onset of nonlinearity. One possible interpretation is that the CVI SiC surrounding the tows cracks at the onset of nonlinearity. The tows, now free of constraint, are able to straighten. Their straightening is likely resisted by normal and frictional interaction with the transverse weft tows, allowing load to be carried by the warp tows. Eventually, lockup of the fabric occurs. At this point, the axial strain in the tows reaches a critical value and the fiber bundles fail. Evidently, this occurs at a lower global strain in the small unit cell composite. The tighter packing of the weft tows may prevent them from accommodating the motion of the warp tows.

In the *fully-processed* composites loaded in the warp and the weft direction the response after the onset of non-linearity is approximately linear. A comparison of the partially- and fully-processed composites suggests that the matrix still supports load; in the warp oriented specimens this is a large fraction of the total load. Evidently, after the onset of matrix damage the response of

the tows is similar to the response observed in the partially-processed state. In the weft direction, fracture occurs at a similar bundle stress and fracture strain as those observed in the partially-processed composites (Fig. 3.5). In the warp direction the fracture strain is much lower than in the partially-processed composites. One possibility is that the tows are well constrained by the surrounding matrix. This results in the fibers bearing the applied strain, rather than accommodating it through straightening. They ultimately fracture at a strain similar to that of the weft oriented specimens.

3.5 Summary and conclusions

Each of four composite systems were loaded in two directions in tension. The results help to guide the path of development for virtual models.

The elastic response of the partially-processed composites was found to be represented well by a homogenized tow; in the weft direction the response was equivalent to the fiber contribution and in the warp direction there was an additional contribution of tow waviness. Indeed, the virtual model, once calibrated, captures the elastic response of the partially-processed composites well. It outperformed the curved beam model in predicting the elastic response of the large unit cell composite. This may be due to the more complex warp tow shape and the explicit inclusion of weft tows which inhibit out of

plane motion of the warp tows.

Development of a model for the inelastic response of the partially-processed composites loaded in the warp direction would require considerable modifications. One way to capture the onset of softening would be to explicitly mesh the CVI SiC surrounding the tow with elements capable of discrete damage. After the CVI SiC cracks, the tow interior would need to be given a very low bending stiffness. Therefore a new calibration of the tow properties would be required. Contact with neighboring tows would need to be explicitly modeled so that lockup of the fabric can occur.

The elastic response of the fully-processed composites should be represented well by homogenized tows embedded in a matrix. A laminate model of the composite captured the elastic response in both the weft and the warp orientations well when the influence of tow waviness was included in the warp loading direction. Since the virtual model already includes tow shape and a local coordinate system, all that would be required is a calibration of the matrix properties.

The inelastic response of the fully-processed composites should be captured well with a couple of modifications to the elastic model. In both the warp and the weft loading directions the response is essentially bi-linear, with a terminal tangent modulus equal to the modulus of the corresponding partially-

processed composite. Meshing the matrix with elements capable of discrete damage would capture the onset of nonlinearity. Cohesive elements added to the tow-matrix interface would enable the matrix to carry a near-constant load throughout the inelastic regime, as observed in experiments. Including debonding between the tows and the matrix would also be consistent with the debond cracks observed near the fracture plane of the fully-processed specimens (Fig. 3.8). The development of a model, based on the augmented finite element method (AFEM), that incorporates these features will be discussed in Chapter 6.

One additional observation of the response of the fully-processed composites is that the cracks appear to be present in the elastic regime (Fig. 3.9). This is in agreement with the cracks observed in Figures 2.3 and 2.4 of the composites in their as-processed state. A faithful model of the tensile response of the composite would need to include these cracks. Therefore, a model which captures thermal stresses that occur during processing needs to be developed. One such model based on the discrete element method (DEM) will be presented in Chapter 6. A necessary component to a thermal stress model is the calibration of thermoelastic properties for the tows, analogous to the calibration of elastic tow properties presented here. Calibration of the thermoelastic tow properties will be addressed in the following chapter.

Table 3.1: Elastic Properties of Tows

E_x	E_y	G_{xy}	G_{yz}	ν_{xy}	ν_{yz}
179 GPa	29 GPa	29 GPa	10 GPa	0.23	0.47

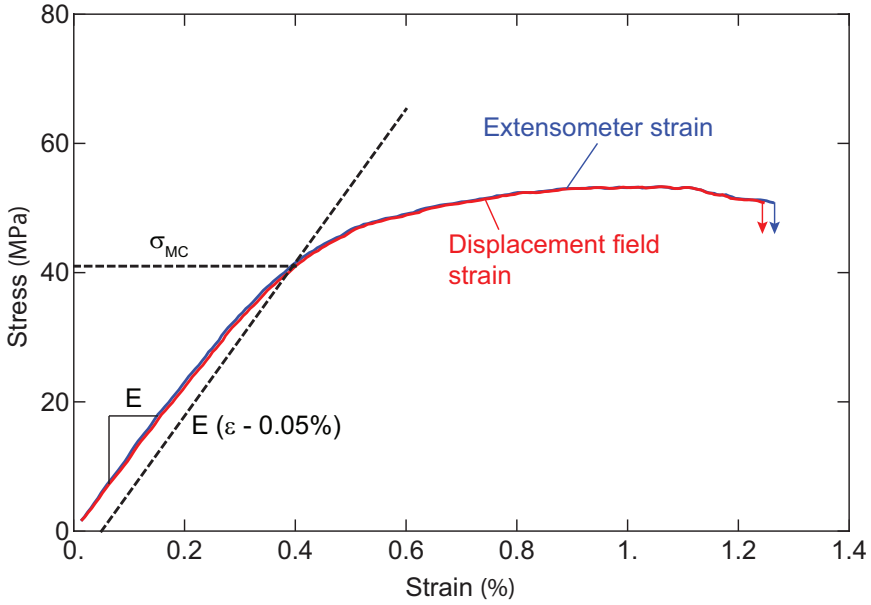

Figure 3.1: Comparison of global strains calculated with virtual extensometers and displacement fields in a partially-processed, warp oriented, small unit cell specimen. Dashed lines indicate the strain offset method for determining the matrix cracking stress σ_{MC}.

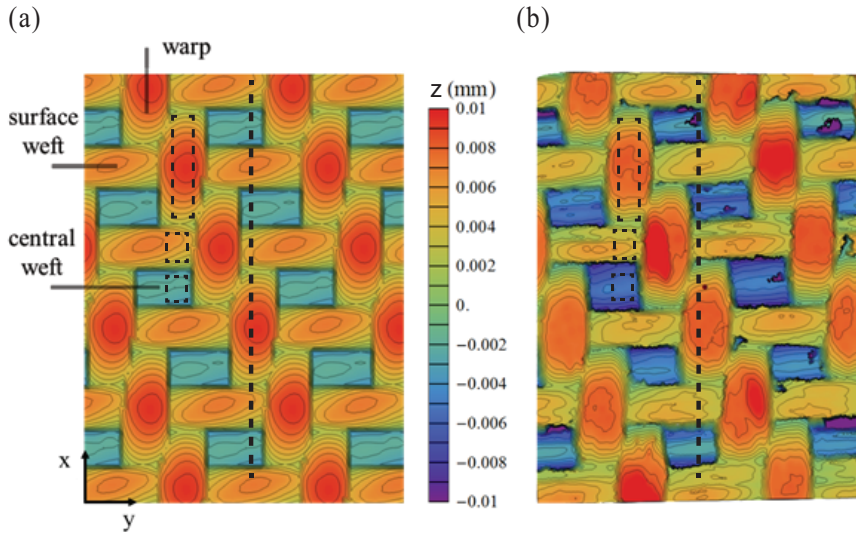

Figure 3.2: Surface topography of partially-processed, large unit cell (a) virtual and (b) physical tensile specimens as identified by surface nodes and DIC, respectively. Dashed boxes indicate representative tow segments. Dashed lines indicate the location of the line scans shown in Figure 3.10. (Blacklock et al., 2014a)

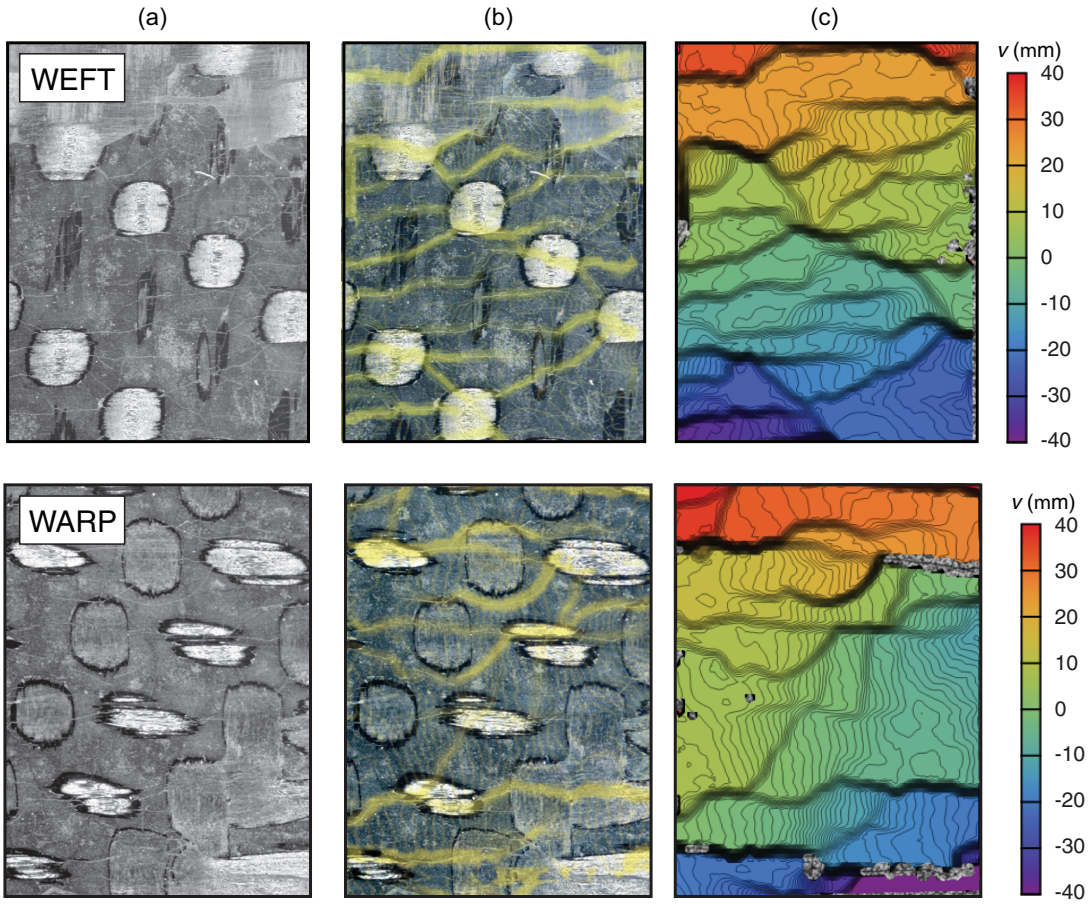

Figure 3.3: Crack locations on (a&b) the polished surface of tensile specimens of the fully-processed small unit cell composite tested in both the warp and weft orientations. The observed crack locations are in excellent agreement with (c) displacement discontinuities measured by DIC in the image before failure.

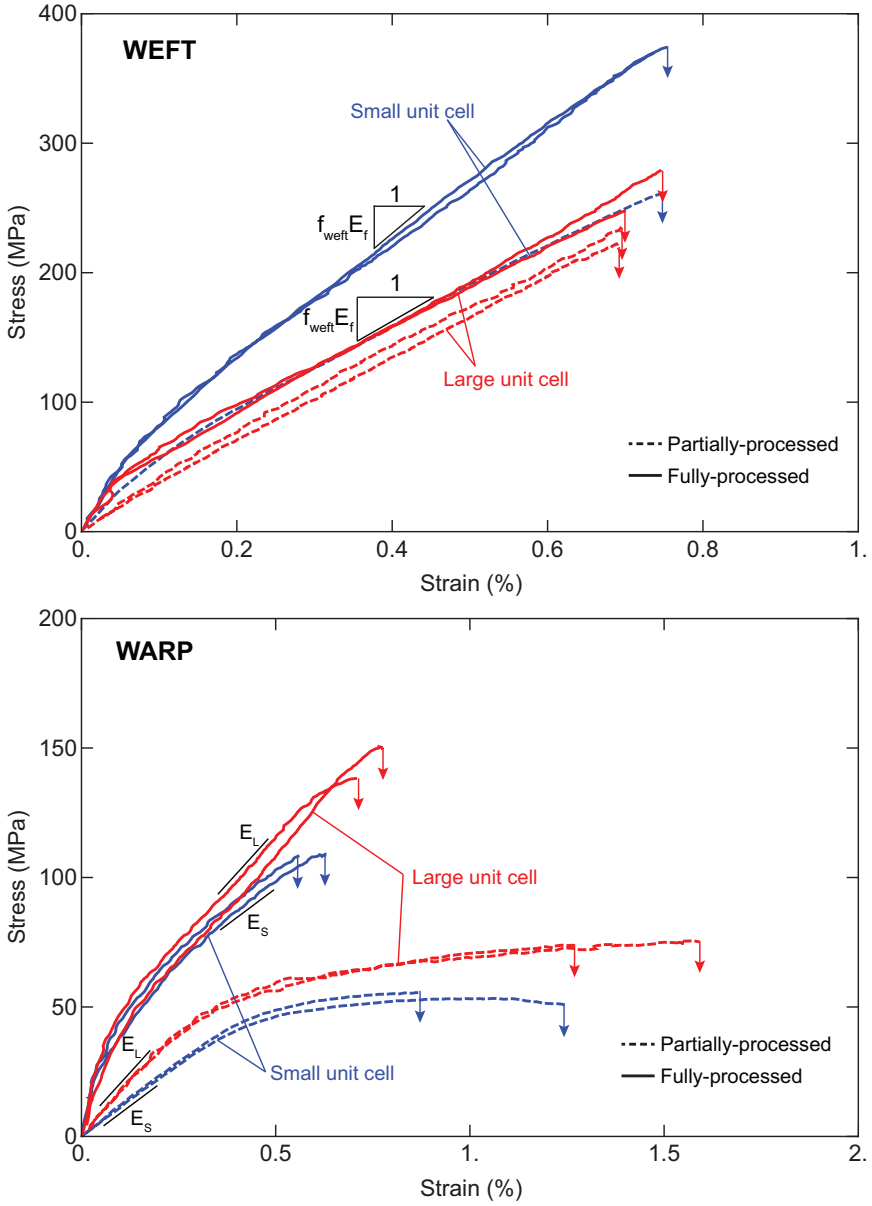

Figure 3.4: Global stress-strain response for partially- and fully-processed composites with large and small unit cells. E_L and E_S denote the initial elastic modulus of the large and the small unit cell partially-processed composites, respectively. Note the different scales in the warp and the weft loading directions.

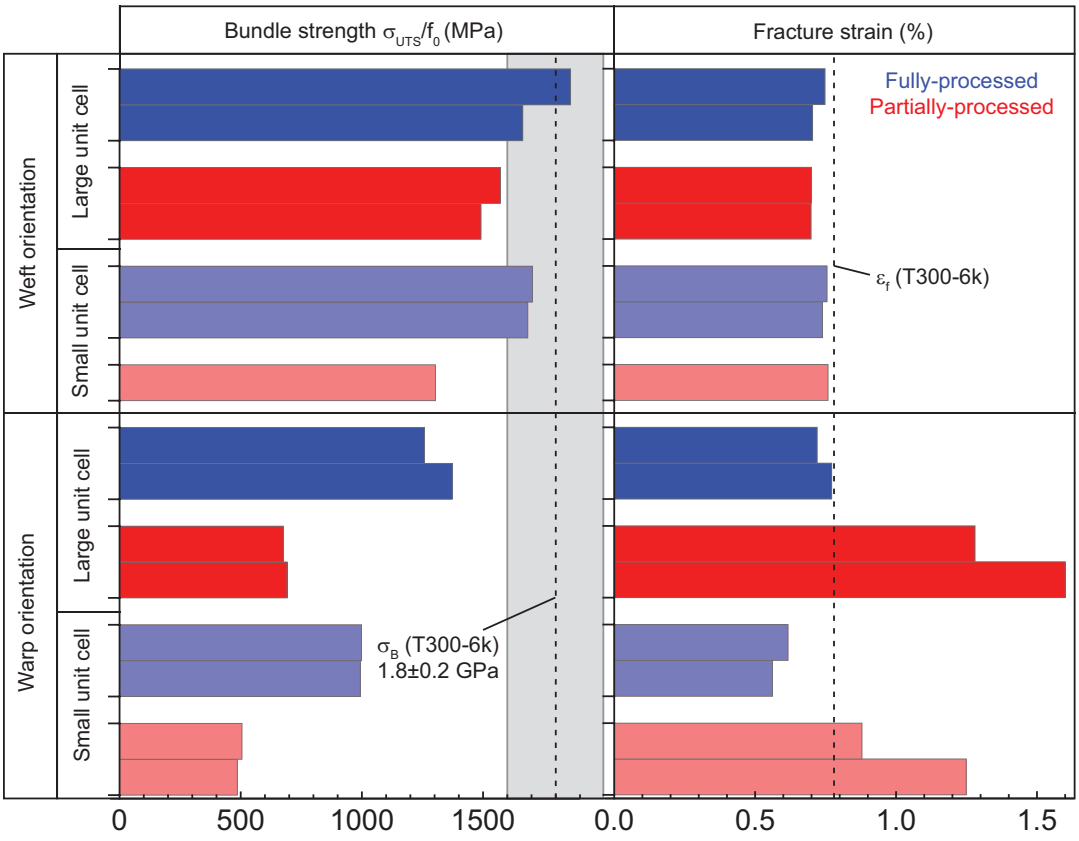

Figure 3.5: Bundle strength and fracture strain of all composites in both loading orientations. Axial fibers are assumed to carry all load at failure.

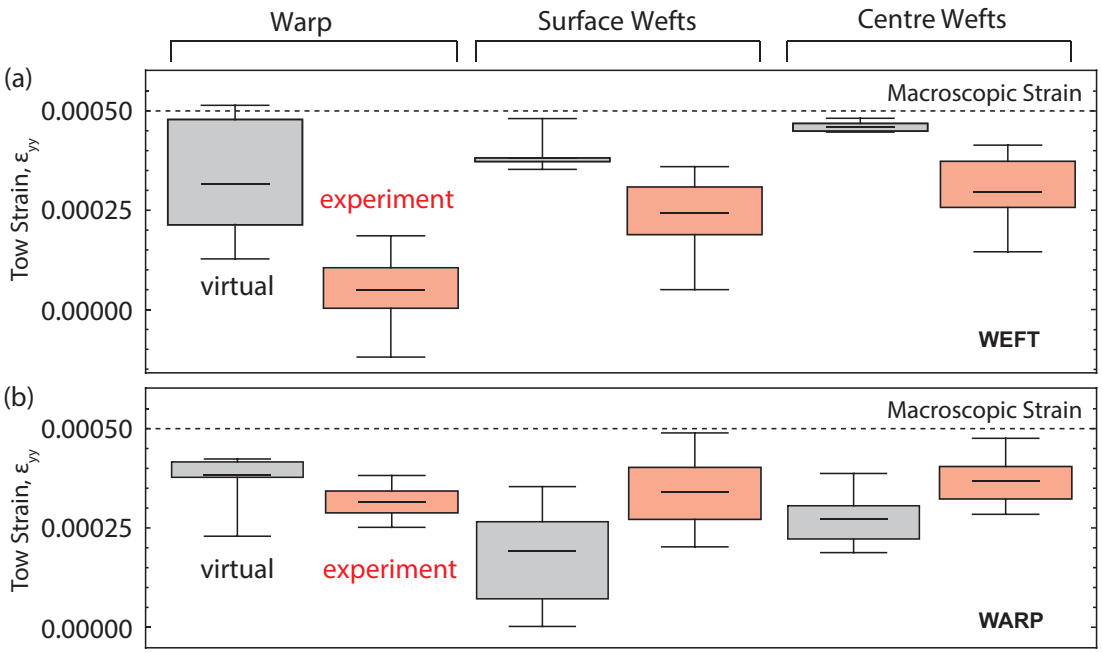

Figure 3.6: Local strains for populations of tow segments of (a) weft- and (b) warp-oriented specimens at 0.05 % global strain. Tow interaction is tied. (Blacklock et al., 2014a)

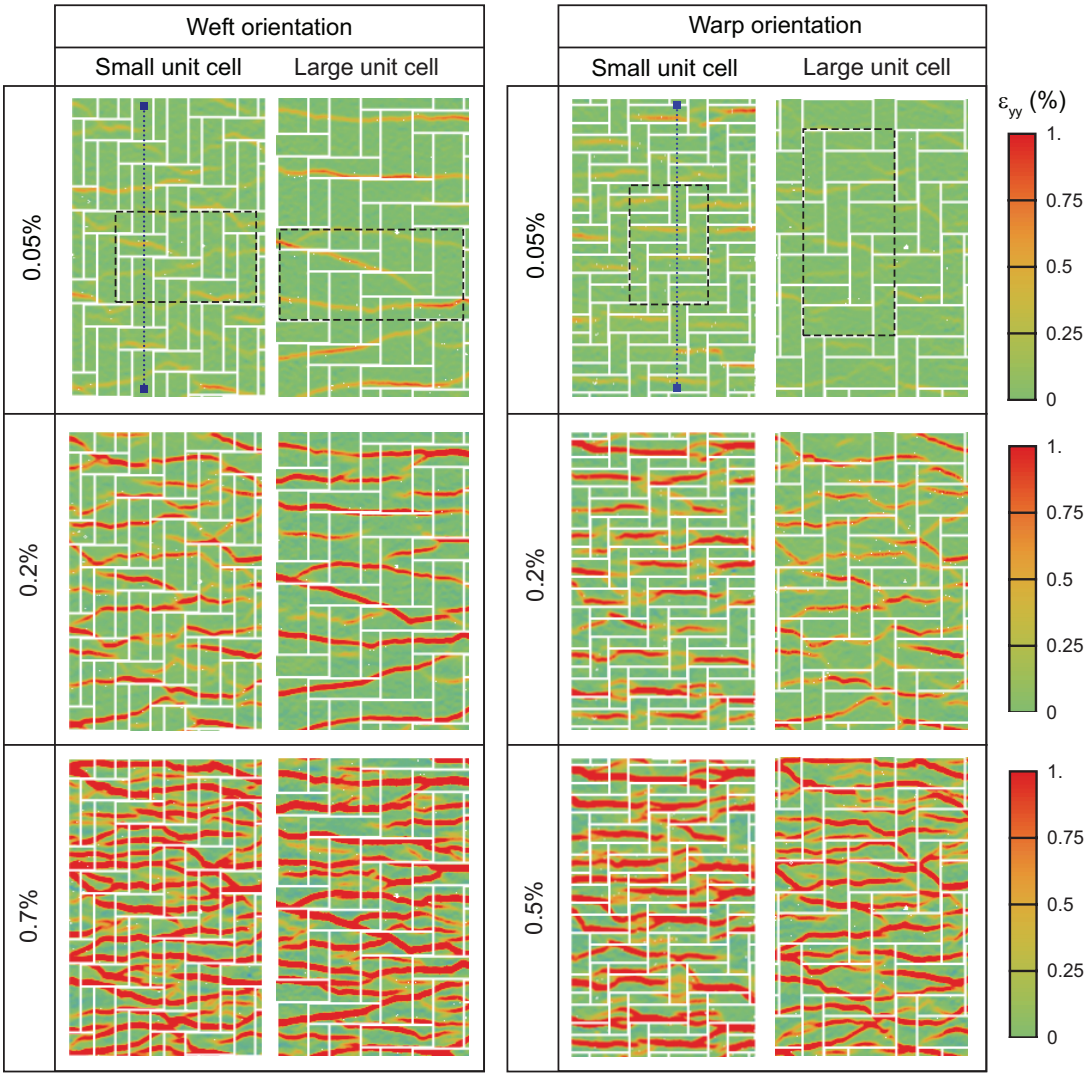

Figure 3.7: Contour plots of full-field axial strain for fully-processed tensile specimens. Dashed boxes indicate unit cell size. Dotted lines indicate location of line scans and cross-sections shown in Figure 3.8.

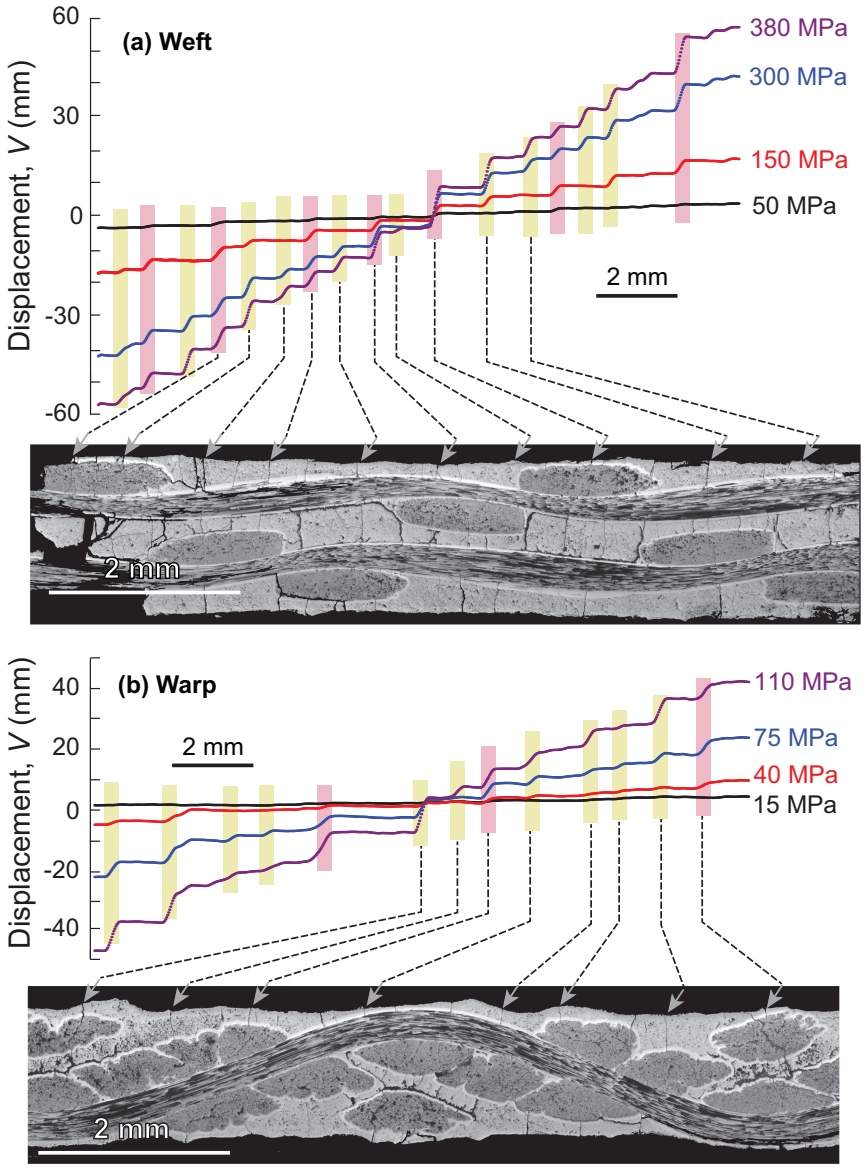

Figure 3.8: Line scans of axial displacement, v, highlighting the development of cracks at representative stress levels. Also shown are micrographs of optical cross-sections of the fractured small unit cell specimens and the correlations between the cracks and the displacement jumps. (a) Weft direction ($\sigma_{MC} = 115\,\text{MPa}$); (b) warp direction ($\sigma_{MC} = 50\,\text{MPa}$).

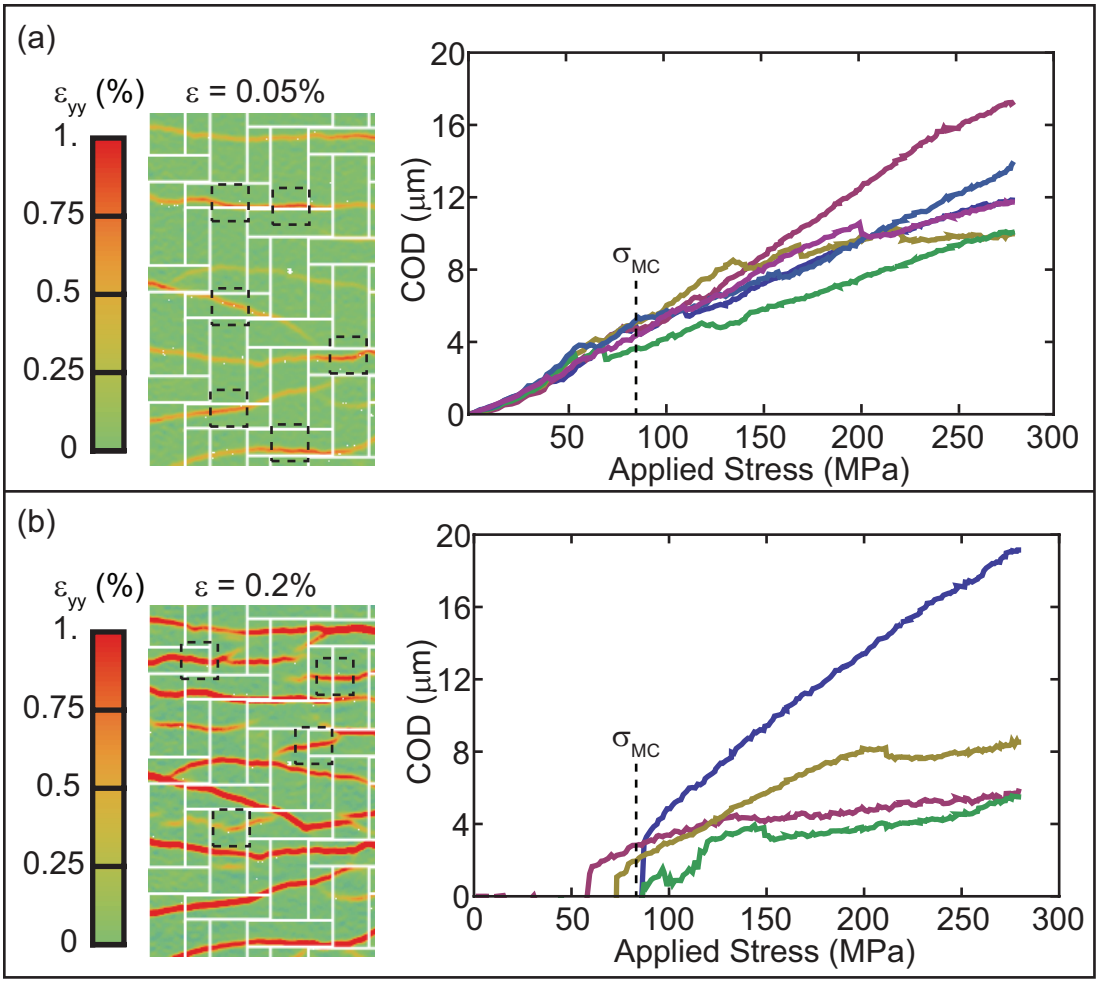

Figure 3.9: Average crack opening displacement in a fully-processed, large unit cell composite loaded in the weft orientation. Average COD is calculated within regions identified by dashed boxes for (a) cracks present in the elastic regime and (b) cracks present only after the global onset of nonlinearity.

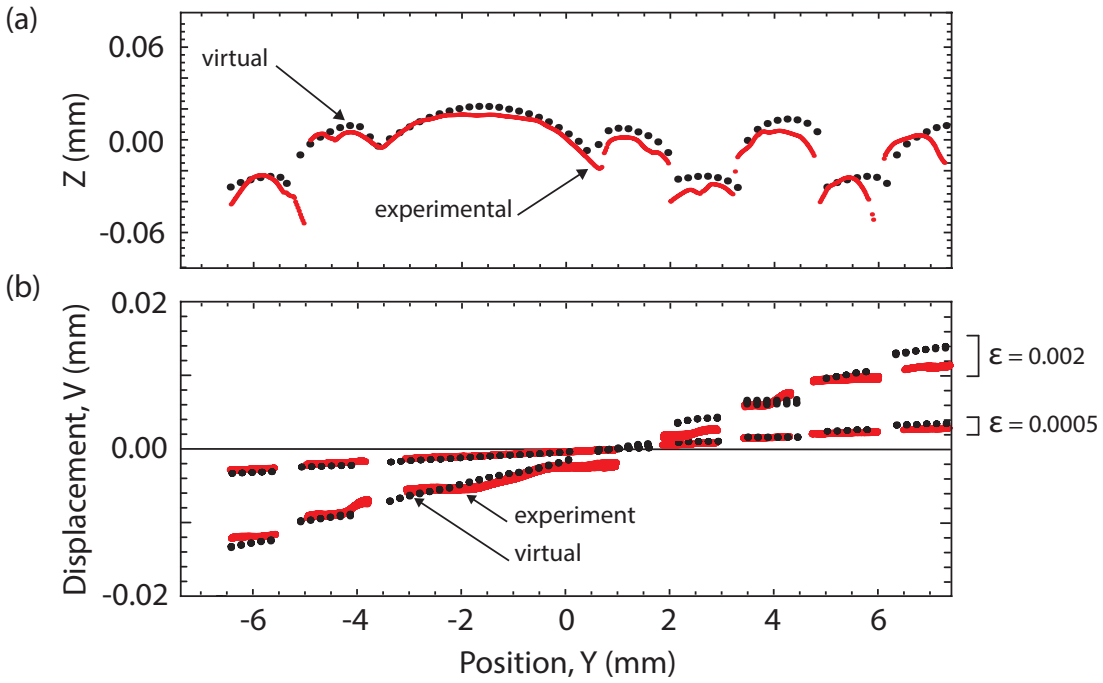

Figure 3.10: Line scans of (a) surface topography and (b) axial displacement of physical and virtual tensile specimens of the large unit cell composite. The position of the line scan on each specimen is indicated in Figure 3.2. Line scans of displacement have finite width equal to the size of the segments in Fig. 3.2 ($\sim$1 mm). (Blacklock et al., 2014a)

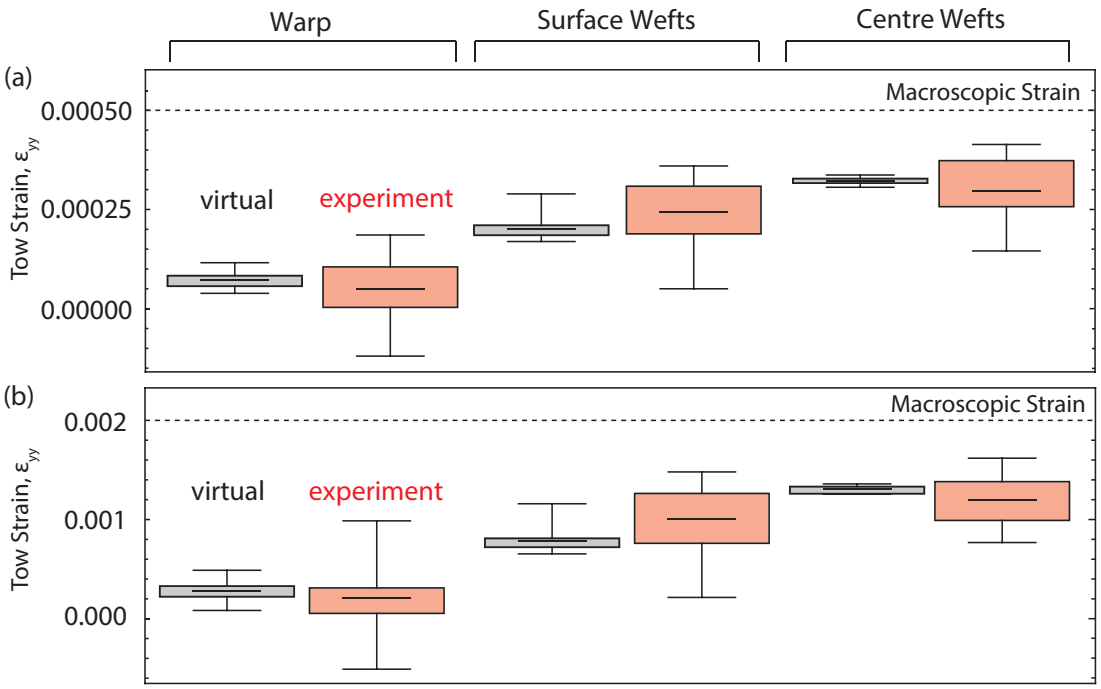

Figure 3.11: Local strains for populations of tow segments of physical and virtual weft-oriented specimens at (a) 0.05 % and (b) 0.2 % global strain. Tow interaction is frictionless. (Blacklock et al., 2014a)

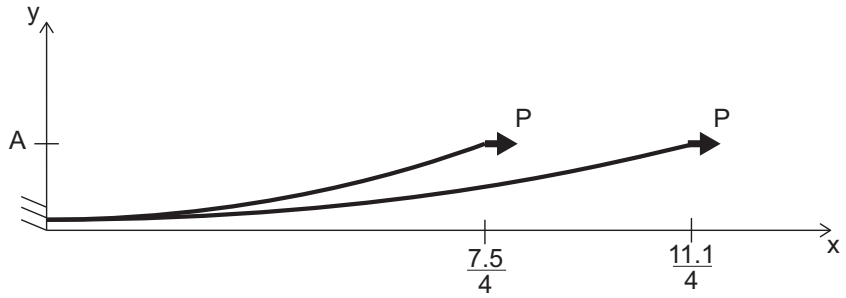

Figure 3.12: Schematic of curved beam model of warp tows. Tows have initial length $\lambda/4$, where λ is their wavelength, and amplitude $A = 0.58\,\text{mm}$.

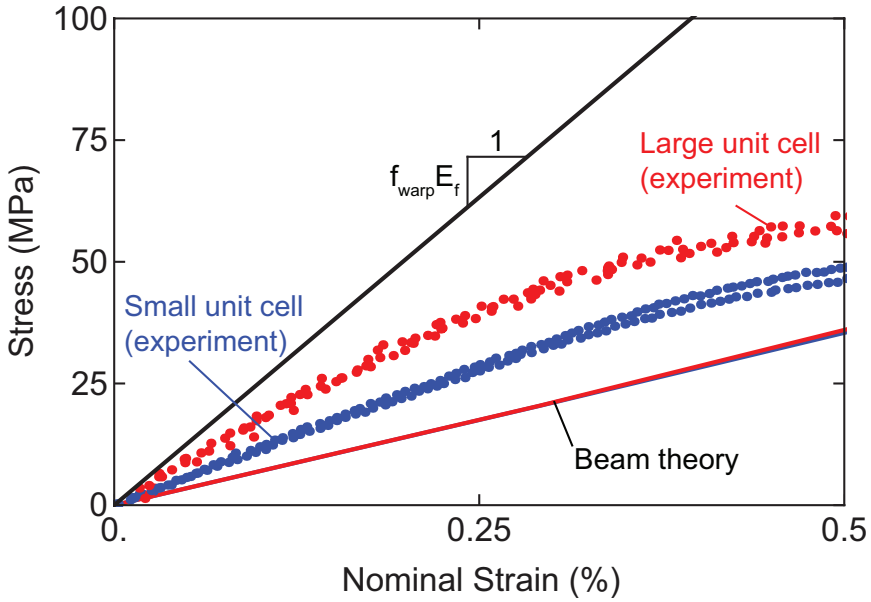

Figure 3.13: Nominal strain given by the extension of the endpoint of a curved beam for the large and the small warp wavelength composites. The expected fiber contribution to modulus (assuming straight fibers) is plotted for comparison.

Chapter 4

Calibration of thermoelastic tow properties

4.1 Introduction

The present study is focused on advancing one specific facet of the virtual test: that of the thermal expansion behavior of a highly anisotropic C/SiC composite. This composite exhibits complexity over a range of length scales and

This chapter is adapted from a peer-reviewed publication: J. H. Shaw, V. P. Rajan, M. Blacklock and F. W. Zok. Towards Virtual Testing of Textile Composites: Calibration of Thermoelastic Tow Properties. *Journal of the American Ceramic Society*, 97(4):1209–1217, 2014. Available at: http://dx.doi.org/10.1111/jace.12829

with respect to several physical and mechanical phenomena. First, as with all textile composites, internal stresses resulting from a uniform macroscopic thermal or mechanical load are inherently nonuniform and depend on the weave architecture. Second, the constituents exhibit large mismatch in their respective coefficients of thermal expansion (CTE); typically, the axial and radial CTE of the fibers are about zero and $9 \times 10^{-6}\,\mathrm{K}^{-1}$, respectively, whereas that of SiC is about $4 \times 10^{-6}\,\mathrm{K}^{-1}$. Thus, for a thermal excursion of 1500 K, the axial misfit strain between the constituents is about 0.006: likely sufficient to initiate local failure. Third, because of the nature of the methods employed in CMC processing, the matrix material tends to be distributed nonuniformly. For instance, during the chemical vapor infiltration (CVI) process commonly used in forming a SiC matrix, the tows can become pinched off from their surroundings once a sufficiently thick shell of SiC has formed on the tow surface, thereby preventing further ingress of the gases needed for densification. This has important implications regarding the anisotropy of the CTE and the stiffness of the tows as well as the anisotropy of thermal conductivity. Virtual tests are therefore highly desirable for probing the many facets of thermomechanical response of these composites.

The specific goal of the present study is to assess the capability of a virtual test in predicting the tow-scale thermal strains in a partially- and fully-processed C/SiC composite. The study builds on recent advancements in test-

ing capabilities: notably, full-field strain mapping at sub-tow length scales, at temperatures up to 1500 °C (Novak and Zok, 2011).

The chapter is organized in the following way. In the first section, the materials of interest, the testing and analysis protocols, and the experimental measurements are described. The second section focuses on the virtual tests. Here, the goal is to identify the thermoelastic constants of the fiber tows that yield predicted fields that are consistent with the experimental measurements. One practical challenge is that the calibration is essentially underconstrained: the number of unknown variables exceeding the number of discriminating tests. Following the identification of the thermoelastic constants, the effect of the presence of a slurry- and PIP-derived matrix on composite thermal expansion is examined.

4.2 Experimental investigations

4.2.1 Material

The materials examined in this study are the partially- and fully-processed large unit cell composites introduced in Chapter 2. Pertinent microstructural features are shown in Figures 2.1 and 2.3. In the partially-processed state the effects of the anisotropic thermoelastic properties of the tows are manifested

strongly in the spatial distributions of the thermal strains measured on the external surfaces (the presence of a dense matrix between tows would mask such effects). The fully-processed composite was studied to ascertain the degree of constraint imposed on the anisotropic thermal expansion of the tows by a slurry- and PIP-derived matrix.

4.2.2 Heating and thermal strain measurements

Thermal strains were measured using a laser heating and imaging system, shown in Figure 4.1 and described elsewhere (Novak and Zok, 2011).

Briefly, heating was accomplished with a 2 kW CO_2 laser operating at a wavelength of 10.6 µm. Custom optics were utilized to homogenize the beam. Temperature measurements were made using a combination of a two-color pyrometer operating at 800 nm and 950 nm, a two-color spot pyrometer operating at 800 nm and 1.7 µm, and a single-color infrared camera operating at 3–5 µm.

Illumination for optical imaging and strain mapping was accomplished using an array of blue LEDs operating in the wavelength range 440–460 nm. Imaging was performed with a pair of optical cameras fitted with 100 mm macrolenses. Band-pass filters were attached to the lenses to limit the wavelength of reflected and emitted light to a narrow band bracketing the LED

output. Effects of thermal turbulence were minimized using an Ar gas knife blowing tangentially to the sample surface. The Ar also mitigates to some extent the rate of sample oxidation. In the present experiments, the magnification of the optical imaging system was 11 µm/pixel at a standoff distance of 32 cm. Following the experiment, the sequence of images was correlated using the VIC-3D DIC software (Correlated Solutions Inc., Columbia, SC).

Test samples 12 mm × 12 mm in size were machined from the composite plates. The samples were speckled using an alumina slurry (Pyro-Paint 634-AL; Aremco Products Inc., Valley Cottage, NY) sprayed through an airbrush. The average speckle size, measured using an autocorrelation technique, was 100 µm. The samples were placed in a 12.7 mm × 12.7 mm × 2 mm deep well cut into a sheet of graphite. The well dimensions were selected to be slightly greater than the sample size to prevent intimate contact between the sample edges and the graphite (and hence minimize heat conduction) as well as allow thermal expansion to occur without constraint. The graphite sheet was backed by a plate of low-conductivity porous SiC.

Samples were heated at a rate of 300 K/min up to a target maximum temperature of 1000 °C, held at fixed heat flux for 3 min (to reach thermal equilibrium), and then allowed to cool. The strains were measured after thermal equilibrium had been attained. The average temperature was 1026 ± 10 °C

for three samples from the partially-processed panel; the average temperature for the four samples from the fully-processed panel was slightly higher at $1045 \pm 10\,^{\circ}\mathrm{C}$. The temperature profile on the sample surface was monitored using the IR camera and was verified to be uniform within $\pm 10\,\mathrm{K}$. In combination with a thermocouple placed between the specimen and the back plate, the thermal images showed that the through-thickness temperature difference was no greater than 90 K for the partially-processed samples. The through-thickness temperature difference for the fully-processed samples was not measured. Weight measurements before and after testing revealed only a small mass loss: 4 %–7 % for the partially-processed composite and $\sim$1 % for the fully-processed composite. Inspection of the samples after testing indicated that the loss was due mainly to oxidation of the C fibers that had been exposed at the cut edges. Correlations of images taken at ambient and peak temperatures were performed using a subset size of 41 pixels (0.47 mm) and a step size of 4 pixels.

4.2.3 Analysis procedures

Following correlation, the displacement data were imported into Mathematica® (Wolfram Research, Champaign, IL) for segmentation and strain analysis. For quantitative comparisons with the virtual tests (described

below), the DIC results were used to compute separately the average in-plane thermal strains within individual segments of both warp and surface weft tows on the sample surface. (Although narrow segments of central wefts were also visible, their area proved to be insufficient to make reliable strain measurements). To facilitate the latter computations, the DIC data were segmented using the following procedures.

For specimens from the partially-processed panel, weft tows were identified manually by inspecting surface height maps. Each segment was assigned a rectangular domain defined by the tow edges. Then, to eliminate the effects of neighboring tows on the displacement data within any one tow segment, each region of interest was pared by an amount equal to half the subset size around its periphery. In this way, none of the nodal data are affected by points residing in neighboring segments. Figure 4.2 shows an example of the resulting segmented wefts. An alternative technique was employed for segmenting the warp tows. With the warp crowns lying above the other tow segments, the warp segments were isolated from all others by thresholding the surface height (z) data accordingly. A clustering algorithm was then employed to identify the data points that belong to each warp tow segment. The z-threshold was selected to remove regions lying within half the subset size of the tow edges. Finally, to remove segments that intersect the sample edges, segments with areas less than 80 % of their respective genus average were excluded from fur-

ther analysis. The results of the latter segmentation are also shown in Figure 4.2.

The additional matrix in the fully-processed samples prevents tows from being located in the manner described above. Instead, small protrusions in the sample surface corresponding to the warp crowns were used to identify their approximate positions. First, an array of points corresponding to the ideal spacing of warp crowns was created. The array was then overlayed on a topographic map of each sample. The DIC data from each sample were rotated and translated in (x, y) so that the surface protrusions aligned with the ideal array of warp crowns (Fig. 4.3(a)). Once the approximate centers of warp crowns had been identified, the surface was segmented into regions lying above warp and weft tows (Fig. 4.3(b)). The segment positions were calculated based on the measured unit cell parameters and the tow width ($\sim$1.4 mm).

The average in-plane strains in each tow segment were determined by first performing a linear fit to the displacement–position data, $u(x, y)$ and $v(x, y)$. The average in-plane strains, ε_{xx}, ε_{yy}, and ε_{xy}, were computed from displacement gradients in the usual way. The two normal strains (expressed in terms of the global $x - y$ coordinate system) were then classified according to their directions with respect to the local fiber direction: *axial*, if parallel to the tow trajectory and *transverse*, if perpendicular to it. Thus, in total, six populations

of strain measurements were obtained: three each (axial, transverse, and shear) for the warp and the weft tows. Data for all test specimens of each composite were pooled together, yielding about 20 individual measurements for each distribution from partially-processed samples and 25 from fully-processed samples.

Comparisons of sequential image pairs of the partially-processed samples at peak temperature indicated a root mean squared (RMS) displacement error (ν_{RMS}) of 0.01–0.02 pixels, consistent with previous estimates (Rajan et al., 2012). The resulting strain error scales with ν_{RMS}/h_f, where h_f is a characteristic dimension used for strain averaging (*i.e.*, the gauge length) (Orteu et al., 2007; Rajan et al., 2012). For gauge lengths employed in computing the average tow-segment strains, the strain error is estimated to be in the range of 1×10^{-4} to 3×10^{-4}.

The RMS displacement error for samples of the fully-processed composite was considerably higher ($\nu_{RMS} \approx 0.08$ pixels). Thermal turbulence was determined to be the cause of the increased error; distortions were apparent in the raw images of the composite surface. The thermal turbulence was assumed to be spatially and temporally random; its effects were mitigated by averaging the displacement fields of each sample over $\sim$ 35 sequential images. This is the entire set of images captured during the dwell period, with the exception

of those taken during the first 30 seconds of the dwell (to allow some time for thermal equilibration). Using this procedure, the estimated strain error in computing average tow-segment strains is 2×10^{-4} to 6×10^{-4}.

4.2.4 Experimental results

Maps of normal strains and surface height for a representative sample of the *partially-processed* composite are shown in Figure 4.4. Superimposed on the maps are the approximate locations of the boundaries of the surface wefts and the warp tows. Upon inspection, it is apparent that the tows exhibit anisotropic thermal expansion. For instance, the strain ε_{yy} in the weft tows is about twice that in the warp tows (left image of Fig. 4.4(b)). Conversely, the strain ε_{xx} in the weft tows is about half that in the warp tows. Indeed, these patterns coupled with the fine-scale intratow variations served as the impetus to compute area-averaged strains within individual tow segments; the latter were then used in comparisons with virtual test results.

The strain values obtained by fitting the displacement fields over individual tow segments are summarized in Figure 4.5. They are presented in two forms. In (a) and (b), axial and transverse normal strains in both warp and surface weft tows are plotted against the distance from the sample center to the point of interest. The objective was to assess whether some of the vari-

ation was due to edge effects and, if so, the spatial extent to which the edge effects persist into the sample. Within the scatter in the measurements, no such effects are observed. In (c), normal and shear strains are represented by box-and-whisker plots. Here, each shaded box represents the middle 50 percentile of the distribution, the central line is the median, and the whiskers extending from the box encompass the first and fourth quartiles. The average axial and transverse strains for both tow types are about 0.002 and 0.0045, respectively. The variations over the full range fall within about ± 0.001 of the respective median. These variations are larger than those expected from measurement error alone (the latter would be of the order of twice the estimated error in strain measurement: 2×10^{-4} to 6×10^{-4}). The inference is that the measured strain variations are likely intrinsic to the composite and not solely a manifestation of measurement error.

Average surface strains in the *fully-processed* samples were homogenous across both warp and weft segments and axial and transverse directions (Fig. 4.6). The measured strain in all cases was $\sim$0.004—approximately the expected thermal strain of silicon carbide ($\alpha = 4.3 \times 10^{-6}\,\mathrm{K}^{-1}$ (Lara-Curzio et al., 1993)) subjected to a temperature change of 1000 °C. Evidently, the presence of a matrix between the tows constrains their anisotropic thermal expansion. The average surface strains also exhibit greater variation within each population of segments; this variation is attributable to the higher measurement error in tests

on the fully-processed samples. The expected strain variation, again taken to be twice the measurement error, is 4×10^{-4} to 12×10^{-4}: approximately the same as the observed variation within each population of segments.

4.3 Virtual tests

4.3.1 Specimen and mesh generation

A finite element (FE) mesh of the partially-processed, large unit cell composite was generated following the same procedure outlined in Chapter 3. The virtual specimen generator (Blacklock et al., 2013) was used to create a geometry of the same size as the samples used in the experiments. Comparisons of surface topographies obtained from this generation procedure and measured via DIC are shown in Figure 4.7. The agreement is excellent over most of the area. The slight discrepancies are due in part to the elliptical idealization of the tow cross section in the translation of the CT images into the virtual sample (Bale et al., 2012). Some error also derives from the inability of DIC to correlate near surface discontinuities (e.g., edges of tows).

The tows were then meshed with *TetGen* (Version 1.4.3) (Hang) and imported into ABAQUS (Version 6.9-EF1; Dassault Systèmes, Vélizy-Villacoublay, France). Following a successful mesh convergence study, a mesh

comprising 2.2×10^6 first-order tetrahedral elements (C3D4) was used. For each element, a local coordinate system was defined so that the 1-direction was aligned with the local trajectory of the fiber tow. To prevent rigid body translation and rotation of the entire specimen, select translational degrees of freedom for three nodes within the mesh (each belonging to a different tow) were constrained. Surface-to-surface interactions were specified between neighboring tows to capture the effect of the SiC matrix (discussed below). Surfaces were not adjusted[1] prior to application of the temperature change ($\Delta T = 1000\,\mathrm{K}$, to match the experimental temperature profile). The effects of a through-thickness temperature gradient of 90 K were also simulated. These yielded surface strains that differed from those for isothermal simulations by $< 1\,\%$.

Meshing of the fully-processed virtual specimen proved to be difficult using meshing algorithms built into Abaqus. Evidently the geometry of the tows results in numerous small-angle regions which are difficult to efficiently mesh. A voxel-based meshing algorithm developed by Blacklock et al. (2014b) was used to reduce the number of elements required to mesh the specimen. First, a grid of nodes spaced 50 µm apart was generated over the region occupied by the virtual specimen geometry. The nodes were used to define a mesh of 8-

[1] A commonly employed feature in ABAQUS is the strain-free adjustment for surfaces that are to be tied together; nodes/elements on adjacent surfaces that are roughly, but not exactly, coincident are brought into closer contact without imposing any strain on the elements.

noded quadrilateral elements. Next, a position vector was calculated between the center-point of each element and the nearest triangular facet defining a tow surface in the virtual specimen. The dot product of the position vector with the facet normal vector was used to determine whether or not a given element was within a tow. Elements lying within a tow were assigned a local coordinate system aligned with the tow trajectory. Elements not lying within a tow were taken as part of the matrix. The thickness of the model was selected such that the matrix was at least two elements (100 µm) thick above all tows, as observed in the physical material. The final mesh (1.1×10^6 C3D8 elements) sacrifices some geometric accuracy in representing the tow shapes (see Fig. 4.9).

An additional benefit of the voxel-based mesh, applicable to more complex virtual models, is that element faces and nodes are matched at interfaces between different regions (*i.e.* a tow and the matrix). This is not readily accomplished with unstructured tetrahedral meshes. The shared nodes and element faces between different regions make it possible to mesh the interface. A model making use of a meshed interface is discussed in Chapter 6.

4.3.2 Constitutive behavior

The elastic constants of the tows were determined using the virtual test discussed in Chapter 3; they are listed in Table 3.1. The thermal expansion coefficients of the tows were determined using analogous micromechanical models (Hashin, 1979), detailed in Appendix C. The models take as inputs the CTEs and elastic properties of the composite constituents, where the constituents are now the fibers and the effective medium determined from the mechanical analysis. Two cases were considered, distinguished by the fiber axial CTE. In the first, the axial CTE was taken to be $-0.6 \times 10^{-6}\,\mathrm{K}^{-1}$ (reported by the manufacturer, for near-ambient temperatures). This yields tow CTE values of $\alpha_1 = 0.5 \times 10^{-6}\,\mathrm{K}^{-1}$ and $\alpha_2 = 6.5 \times 10^{-6}\,\mathrm{K}^{-1}$. Other studies have shown a slight temperature sensitivity, with values of fiber axial CTE of about zero (Trinquecoste et al., 1996). Using this value, the composite CTEs are $\alpha_1 = 1.0 \times 10^{-6}\,\mathrm{K}^{-1}$ and $\alpha_2 = 6.5 \times 10^{-6}\,\mathrm{K}^{-1}$. As noted in forthcoming discussion, virtual tests based on these two sets of CTE values yield transverse strains that agree well with the measurements when the tow contact interaction is selected accordingly (as described in the following section); but the axial strains remain low compared to experimental measurements.

Motivated by this discrepancy, an alternative selection was made for the tow axial CTE. Here, the variations in the predicted axial strains with the ax-

ial tow CTE ($0.5 \times 10^{-6}\,\mathrm{K}^{-1}$ and $1.0 \times 10^{-6}\,\mathrm{K}^{-1}$) were extrapolated linearly to the point where the predictions coincided with the measurements for the axial strains of the warp population of tow segments. The resulting inferred axial tow CTE is $\alpha_1 = 1.6 \times 10^{-6}\,\mathrm{K}^{-1}$. Although the absolute value of this CTE remains small relative to those of most ceramics (including SiC), it exceeds the micromechanically based predictions by a measurable amount ($(0.6\text{–}1.1) \times 10^{-6}\,\mathrm{K}^{-1}$).

The matrix filling the space between the tows in simulations of the fully-processed material were assumed to be isotropic. Since the matrix is porous, micro-cracked, and contains both crystalline SiC particulates and amorphous PIP-derived SiC (Fig. 2.3), values for its modulus E_m, Poisson's ratio ν_m and thermal expansion coefficient α_m are not readily calculated. The values of ν_m and α_m are assumed to be 0.2 and $4.3 \times 10^{-6}\,\mathrm{K}^{-1}$, respectively: the same values assumed for the CVI SiC within the tows in the micromechanical models. The Young's modulus of the matrix phase was calibrated using the virtual test.

4.3.3 Tow contacts and interactions

As was done in the mechanical virtual tests on the partially-processed composite, tow contact was simulated in FE using two approaches. To simulate the case where the CVI SiC bonding the tows was assumed to be cracked, fric-

tional contact using a friction coefficient of either 0 or 0.5 was used. The choice proved unimportant, however, as demonstrated in a subsequent section. Simulations of the case where the SiC coating was assumed to be intact used a surface tie interaction between warp and weft tows. Tie tolerances (as defined in Chapter 3) were varied over the range 0.5–75 µm. By comparison, the physical characteristic that most closely relates to the tie tolerance—notably, the thickness of the SiC coating on the tows—is about 30–40 µm. If the CVI process produced a uniform SiC coating of this thickness, tows within 60–80 µm of one another would be expected to be bonded. Thus, 75 µm represents a physically realistic upper limit on the tie tolerance. In all cases, the nodes between adjacent warp tows were tied to one another where they were in contact with one another.

The effects of tie tolerance on the contact patches formed between adjacent tows are illustrated in Figure 4.8 for the three representative tow types. Each of the tows has been bisected along its longitudinal axis and the two halves separated to reveal the contacts on both top and bottom surfaces. The contact patches are color-coded, as indicated by the legend. For a tie tolerance of 0.5 µm, the contact patches (in red) are typically about half a tow width. For the central weft, the locations of the patches made by contact with the warp tows alternate between the fore and the aft regions of the tow. A similar pattern is evident on the bottom side of the surface weft. However, on its top side,

the contacts are made in the central region of the tow. For the warp tows, the contact patches made with the wefts are somewhat more irregular in size and shape, reflecting variations in trajectories of the weft tows. As the tie tolerance is increased to 5 µm, the contact patches expand only very slightly, now encompassing the regions shown in both red and green. The areas grow progressively but nonlinearly with tie tolerance. The degree of contact increases by a factor of about two as the tie tolerance is varied over the full range. Its effect is manifested in the thermal strains predicted by the virtual tests, presented in the following section.

The virtual model of the fully-processed composite is a single body with variable material properties. Since interfaces between different tows (and between the tows and the matrix) share nodes, their displacements are inherently tied.

4.4 Virtual tests versus experimental measurements

4.4.1 Partially-processed composite

The first set of virtual tests was designed to probe the effects of tie tolerance on thermal strains in the warp and the surface weft segments, all for $\alpha_1 = 0.5 \times 10^{-6}\,\mathrm{K}^{-1}$ and $\alpha_2 = 6.5 \times 10^{-6}\,\mathrm{K}^{-1}$ (as determined from the mi-

cromechanical models and the initial estimates of tow properties). These results and the experimental measurements are plotted in Figures 4.10(a) and (b). When the tows are allowed to slide (either without friction or with a friction coefficient of 0.5), the *transverse* tow strains are grossly over-estimated and the axial strains are grossly underestimated. Furthermore, in contrast to the experiments, the virtual tests predict virtually no strain variations. Consequently, this set of tow property values and tie conditions were deemed inadequate. The correlations improve as the contacts are tied and as the tie tolerance is increased. When the most realistic estimate of tie tolerance (75 μm) is used, the computed transverse strains are comparable to the experimental measurements. Furthermore, the computed variations in transverse strains appear to be remarkably similar to those obtained experimentally. However, the computed axial strains remain in rather poor agreement with the experimental measurements.

The results of the virtual tests based on the tow axial CTE obtained by extrapolation are plotted in Figs. 4.10(c) and (d). Here, the computed axial strains for both warp and weft tows appear to be in good agreement with the measurements. The computed strain variations also appear to be of the correct magnitude (though slightly smaller than those obtained in the experiments, the difference being approximately equal to the magnitude of the strain measurement error of ± 0.0001–0.0003). In addition, the computed transverse tow

strains are only very slightly affected, and hence, remain in agreement with the measurements. The inferred axial tow CTE is only very slightly higher than that obtained from micromechanical models and best estimates of the constituent properties ($1.6 \times 10^{-6}\,\mathrm{K}^{-1}$ vs $1.0 \times 10^{-6}\,\mathrm{K}^{-1}$).

Despite the seemingly small amount of SiC in the present C/SiC composite, its effect on thermal strains is significant. The values expected of the fabric alone would be virtually identical to those of the individual fibers in the axial and radial directions: in the range of -0.0006 to 0 in the axial direction and about 0.009 in the transverse direction. The differences between these strains and those measured on the composite indicate a significant role of the SiC matrix.

4.4.2 Fully-processed composite

The virtual test of the fully-processed material illustrates the way in which tows are constrained by the addition of a full matrix. Surface strains on the matrix lying over the tows was calculated for a range of matrix Young's moduli (50 GPa, 100 GPa and 200 GPa). When the matrix is relatively compliant ($E_m = 50\,\mathrm{GPa}$) the anisotropic thermal expansion of the tows is still evident at the sample surface. Figure 4.6 shows that in the warp segments there is minimal difference between axial and transverse surface strains at all values

of matrix modulus. In the weft segments, however, the average transverse surface strains are ∼30 % higher than the average axial surface strains. This is likely due to the three-fold higher stiffness of the underlying tows in the axial direction. The difference between axial and transverse surface strains diminishes with increasing matrix modulus. At a value of $E_m = 200\,\text{GPa}$, the matrix effectively constrains the tows and surface strains are nearly identical in both directions.

The simulations serve as a crude estimate of the matrix Young's modulus. They suggest that a compliant matrix ($E_m < 100\,\text{GPa}$) would be insufficient to mask the anisotropic thermal expansion of the underlying tows. A value of $E_m = 200\,\text{GPa}$ captures the simulations reasonably well, with computed strains equal to the experimental measurements in three of the four combinations of segments and orientations. This is well in excess of the matrix modulus calculated with a laminate analysis in Chapter 3 ($\sim 80\,\text{GPa}$). It is likely that the virtual tests overestimate the matrix modulus. Since the thermal expansion coefficient of the matrix exceeds the axial thermal expansion coefficient of the tows, some of the cracks present in the matrix are likely to close at elevated temperatures. This would have the effect of increasing the stiffness of the matrix. The matrix modulus at room temperature would necessarily be lower than that at high temperature.

4.5 Conclusions

A methodology for calibrating the thermoelastic properties of constituent tows in an anisotropic C/SiC composite based on a combination of real and virtual tests has been presented. Because of the non-uniformity of the matrix phase and the presence of micro-cracks, tow properties cannot be reliably predicted *a priori* using micromechanical models alone; instead, some can only be inferred from coupled experimental/numerical studies of the kind presented here. A small number of iterations of FE simulations is required to achieve satisfactory agreement in all thermal strain components. The number of iterations is minimized by first performing simulations using model-based estimates of the effective tow properties, followed by judicious adjustments to select property values.

The study reveals that although each segment of a particular tow genus is nominally equivalent to all others, the strains within each group exhibit considerable variations. This is attributable to variations in both tow geometry and connectivity between adjacent tows. The virtual tests predict strain variations of comparable magnitude.

Further slurry and PIP processing of the composite resulted in an inter-tow matrix which masked the anisotropic thermal expansion of the underlying tows. The virtual model of the fully-processed specimen indicates that this is a

function of the relative moduli of the tows and the added matrix. As the matrix modulus approaches the axial tow modulus the anisotropic thermal expansion of the tows is masked and surface strains are found to be nearly homogenous.

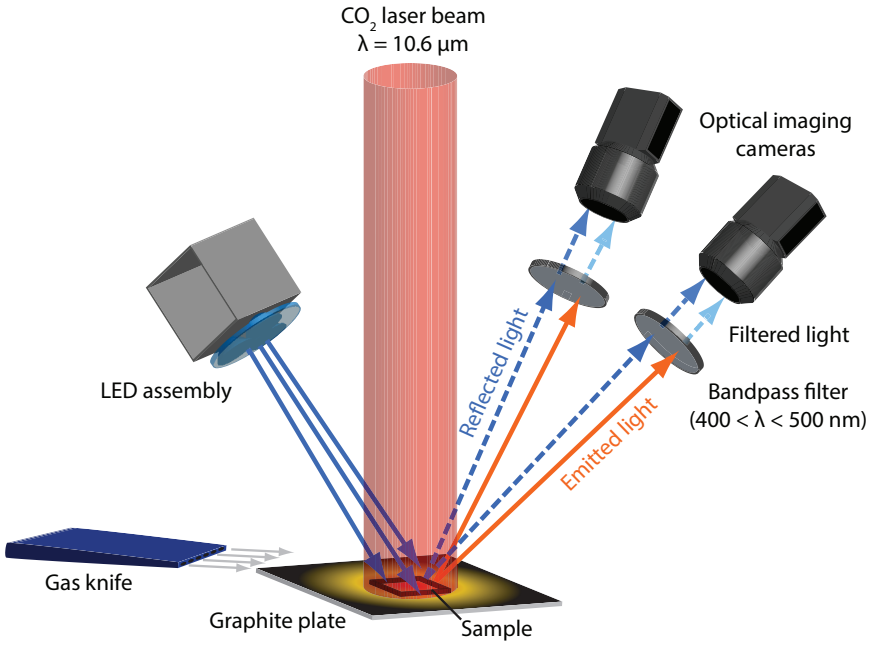

Figure 4.1: Schematic of test apparatus used to map thermal strains.

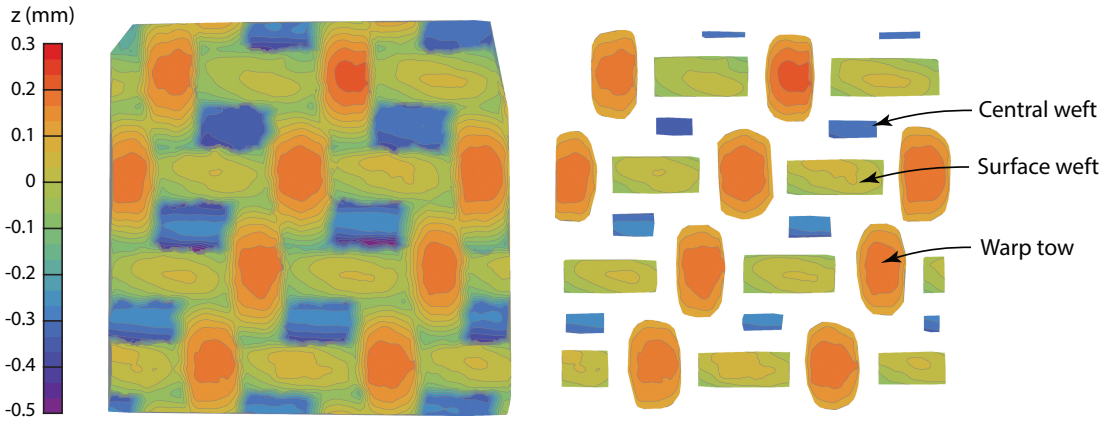

(a) Original topographic map **(b)** After segmentation

Figure 4.2: Topographic map of (a) an entire partially-processed test coupon and (b) the same coupon after segmentation and segment paring.

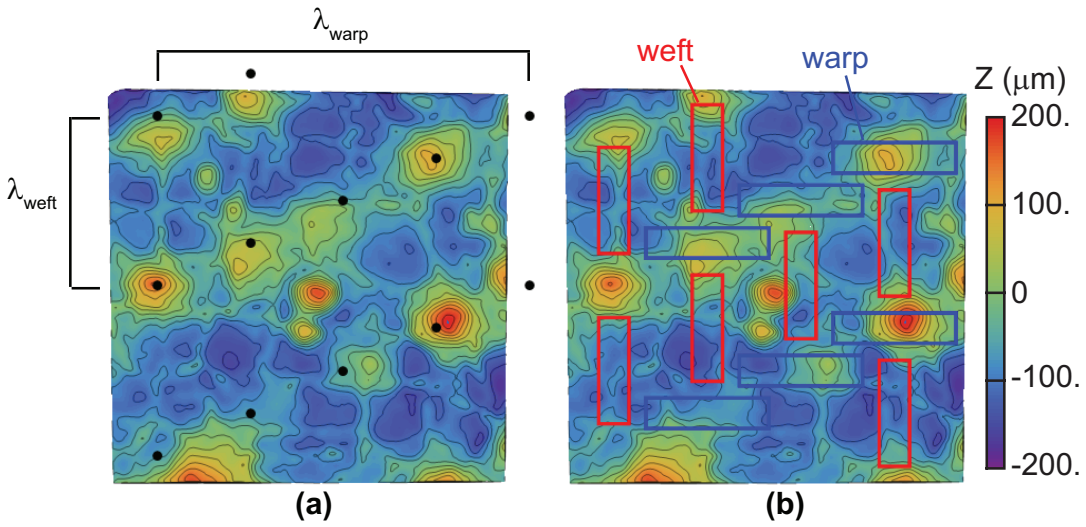

Figure 4.3: (a) Protrusions on the fully-processed sample surface are used to align the sample to an ideal array of warp crown positions. (b) Using measured tow widths and unit cell dimensions, segments are constructed over the approximate locations of tows.

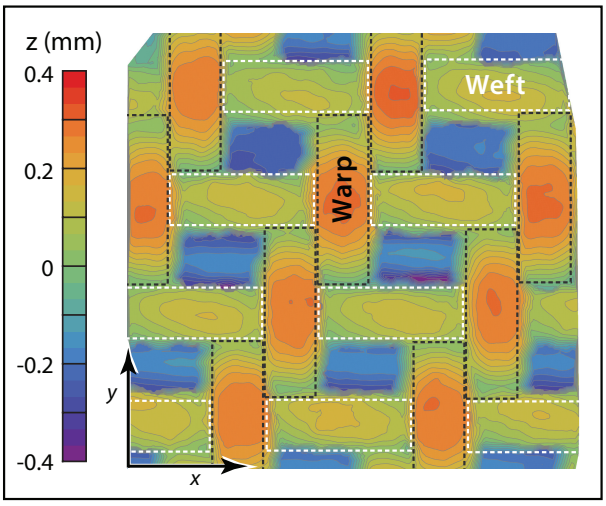

(a)

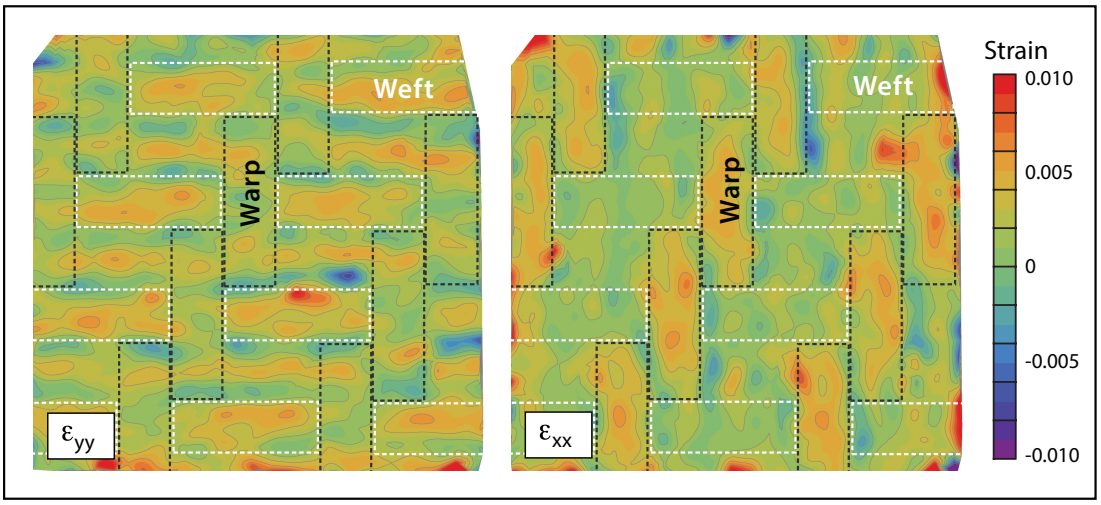

(b)

Figure 4.4: (a) Topographic and (b) thermal strain maps of a representative partially-processed test sample after heating from ambient temperature to 1026 °C.

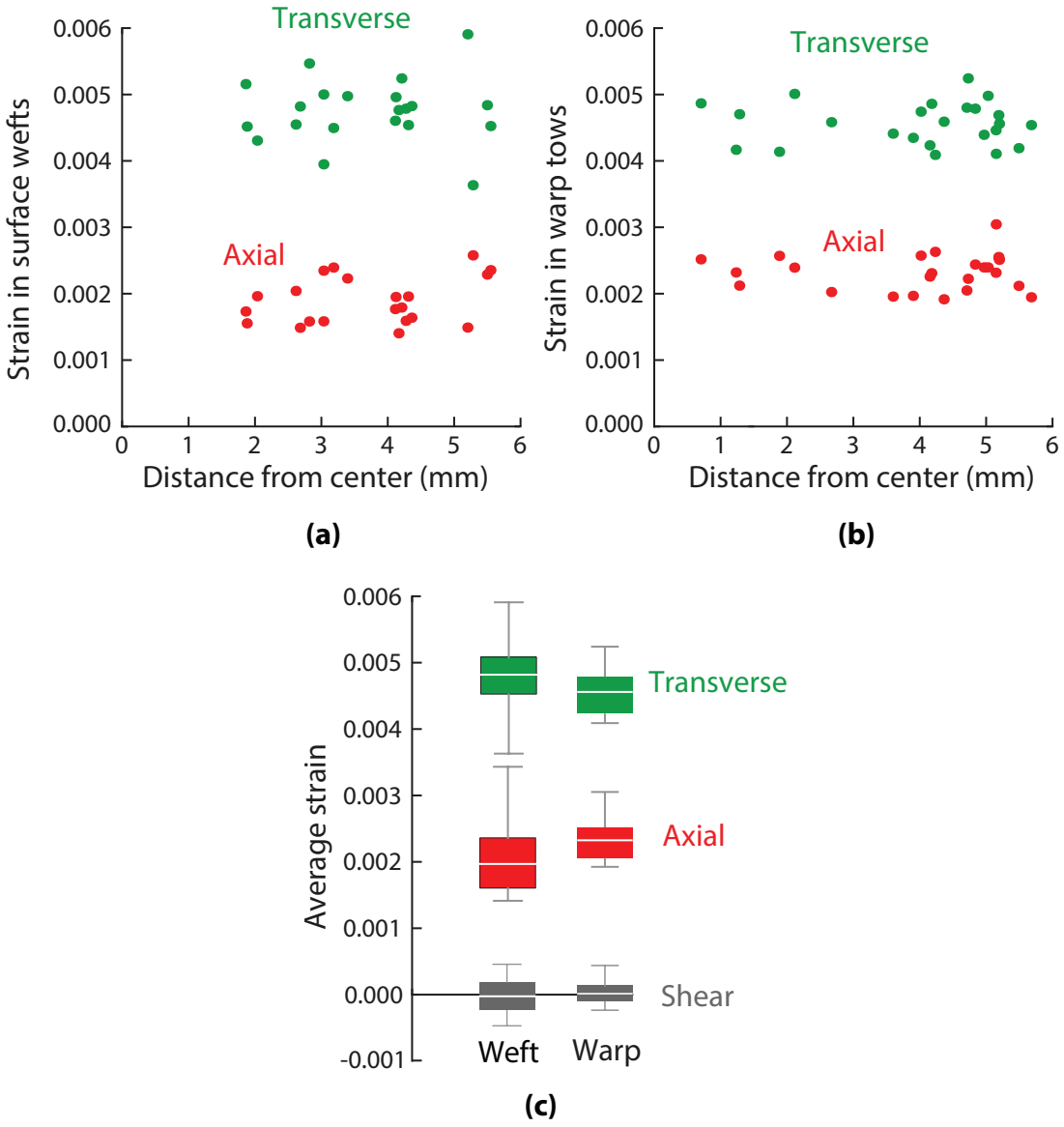

Figure 4.5: Effects of measurement location on strains in (a) surface weft and (b) warp tows of partially-processed samples. (c) Box-and-whisker plot summarizing all distributions.

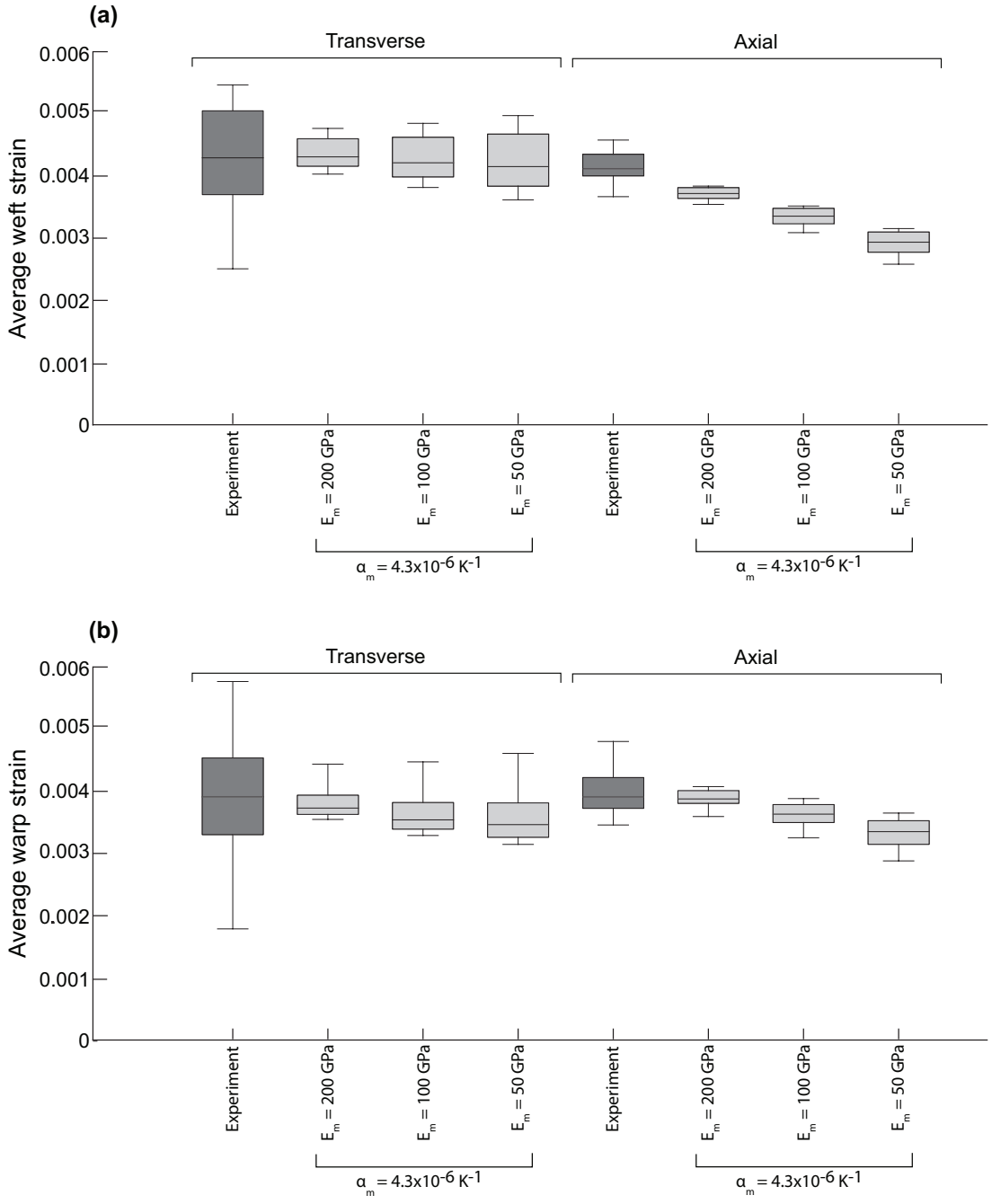

Figure 4.6: Effects of matrix modulus E_m on computed tow segment strains of fully-processed samples. (a) Warp direction; (b) weft direction.

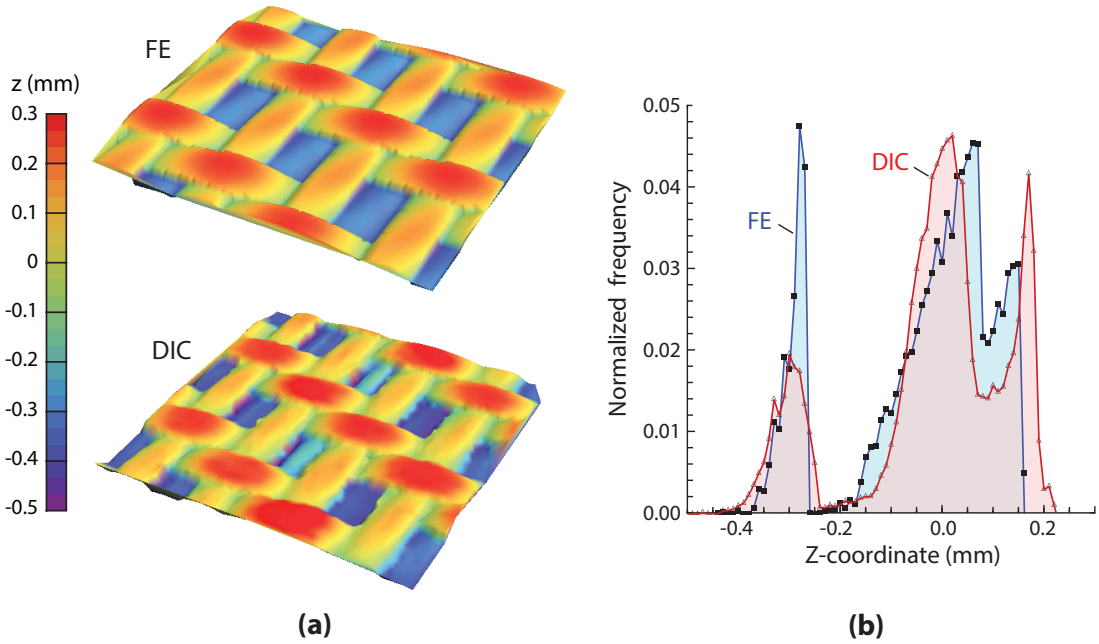

Figure 4.7: (a) Comparison of the partially-processed sample's surface topography obtained from the DIC measurements and the virtual geometry generator. (b) Quantitative assessment of the resulting surface height distributions.

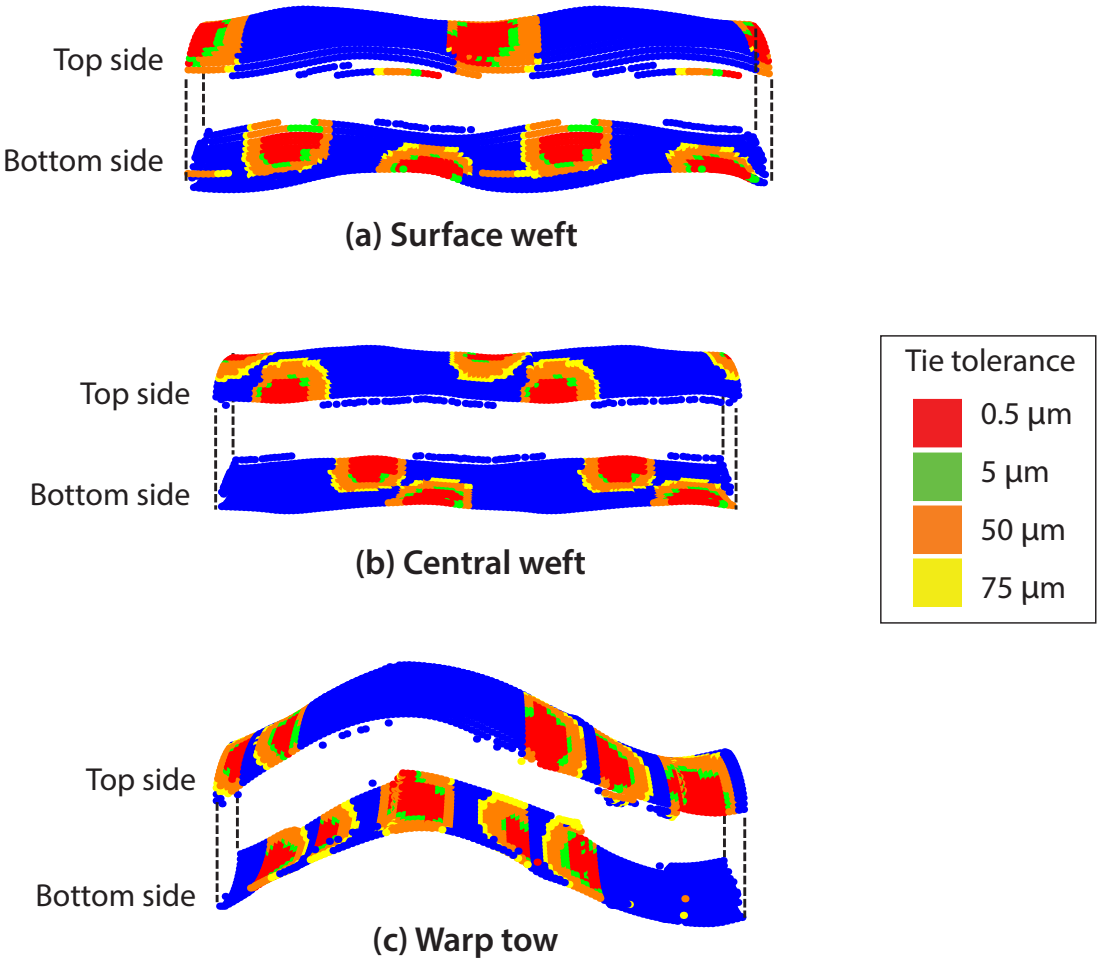

Figure 4.8: Effects of tie tolerance on regions of tow contact.

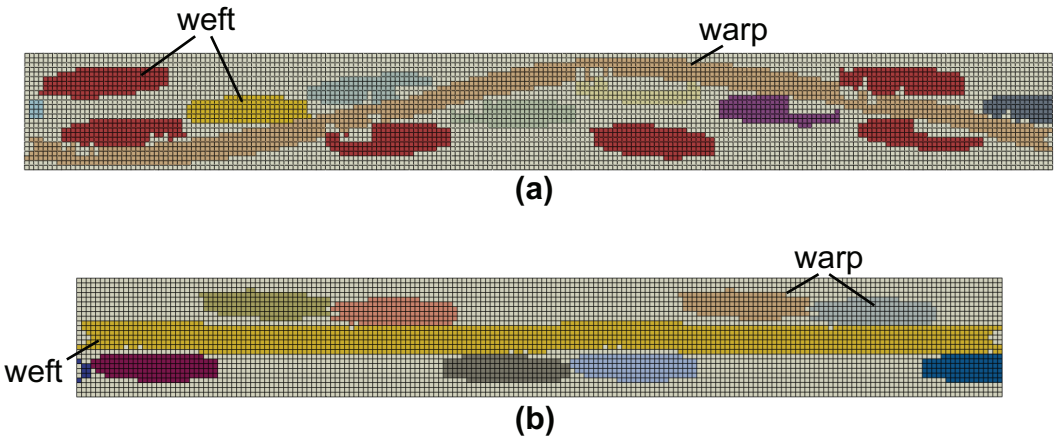

Figure 4.9: Sections of a voxel-based mesh along the (a) warp and (b) weft directions. Note the stepped interface between the tows and matrix.

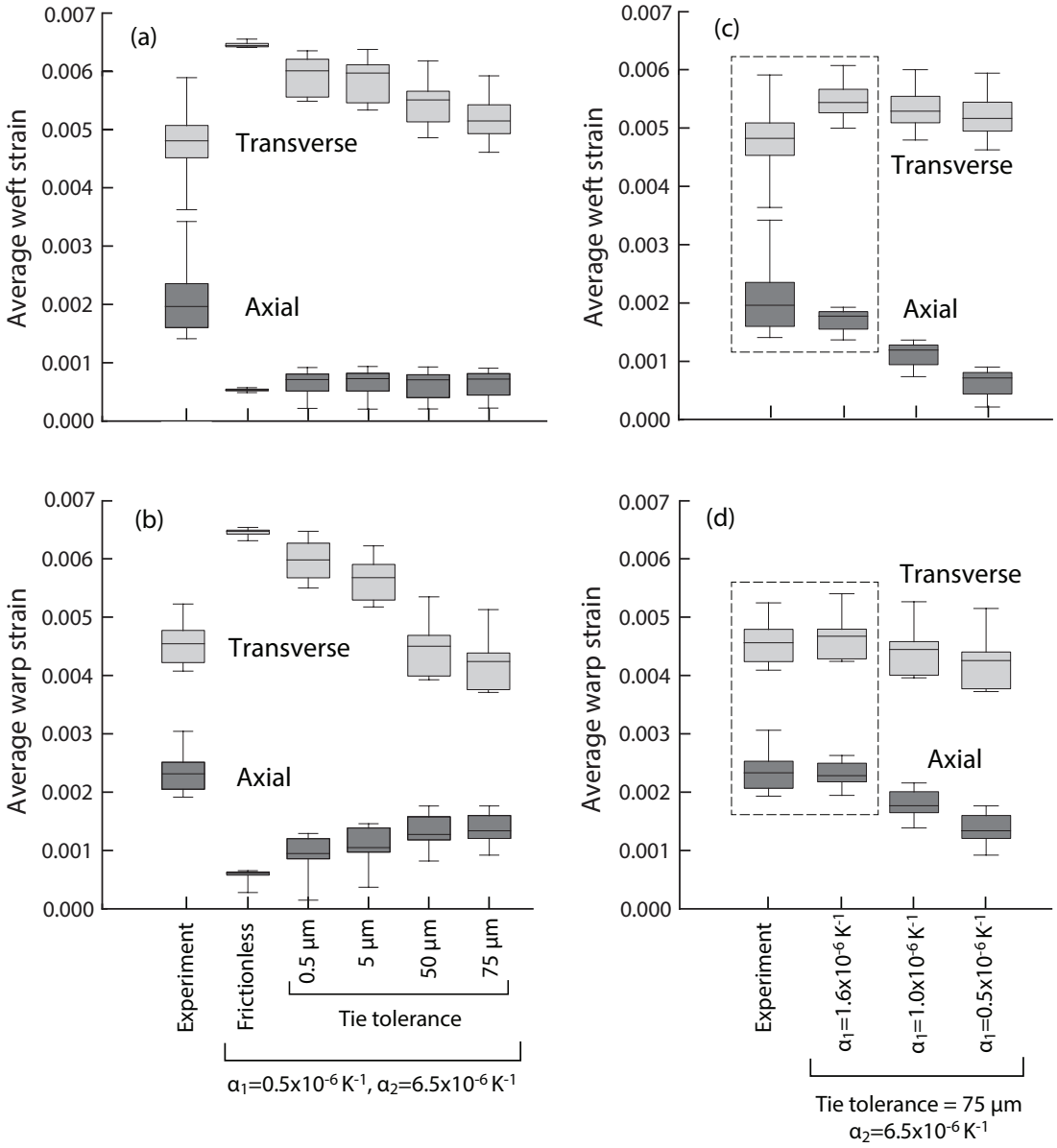

Figure 4.10: Effects of (a) and (b) tie tolerance and (c) and (d) tow CTE values on computed tow segment strains of partially-processed samples (the results for frictional sliding with friction coefficient of 0.5 are identical to those for the frictionless case and thus have not been plotted here). The best correlations between experiments and simulations are contained within the dashed boxes.

Chapter 5

The role of weave features and defects in composite response

5.1 Introduction

As discussed in Chapter 1, one of the desirable aspects of textile-based CMCs is their ability to accommodate features such as holes for cooling, fuel passage or attachment. Marshall and Cox (2008) have shown that by using complex weaves (similar to those used in this study) and fabrication processes such features can be incorporated directly into a fabric preform. However, when using complex weaves, accurate placement of tows and retention of this placement during subsequent processing become increasingly more challeng-

ing; in turn, these challenges increase the likelihood for introducing weave defects. Defects can arise during the weaving operation itself—especially when the preform has complex geometry and the tow densities vary from point to point—or, more importantly, during subsequent handling of the preform after it is removed from the loom. With respect to handling-induced defects, the angle interlock weave is particularly susceptible to shear deformation parallel to the fiber directions, since this deformation is resisted only by inter-tow friction; extension or contraction along the fiber directions are more heavily constrained by the fibers. Rossol et al. (2014) have shown that, for the same fabric preforms used in this study, the magnitude of defects introduced only during weaving and handling can be on the order of 2 %.

Motivated by the desire to incorporate features in components, a great deal of study has been undertaken previously to characterize the notch-sensitivity of strength of a wide range of CMCs. Systems including C/C, C/CAS, oxide/oxide and SiC/SiC have been studied (Cady et al., 1995; Haque et al., 2005; Heredia et al., 1994; Keith and Kedward, 1997; Kogo et al., 1998; Levi et al., 1998; McNulty et al., 1999). Despite popular notions of notch-insensitivity, even the toughest CMCs exhibit some dependence of ultimate tensile strength (UTS) and other performance metrics on notches or holes. The degree of sensitivity depends on: (i) the intrinsic properties of the composite, notably its (generally-anisotropic) elastic, plastic and fracture characteristics; and (ii) the

notch size and shape, characterized by the principal radii a and b (for elliptical holes) and the ratios a/b and a/w (w being the half specimen width) (Haque et al., 2005). The UTS generally decreases with increasing a (for fixed a/b and a/w) and increasing a/w (for fixed a and a/b). Such effects have been found in most composite systems for specimens with circular holes of size $a \geq 1\,\text{mm}$ (Haque et al., 2005; Heredia et al., 1994; Levi et al., 1998; McNulty et al., 1999). Where attempts have been made to compute the stress and strain distributions ahead of holes at the onset of fracture (using an appropriate elastic/plastic constitutive law), the local conditions appear to be consistent with a point stress failure criterion. That is, fracture occurs when the local tensile stress exceeds a critical value (notably the unnotched UTS) at a characteristic distance from the hole, typically about 1 mm. While perhaps fortuitous, the characteristic dimension appears to coincide approximately with the in-plane dimensions of the constituent tows. In systems that exhibit oxidative degradation, notch sensitivity can also be manifested in a reduced lifetime under static loading conditions (McNulty et al., 2001; Ruggles-Wrenn and Kurtz, 2013).

In most cases, holes are introduced into composite components or specimens by conventional machining methods after processing has been completed. Alternatively, they can be introduced into the woven preform without cutting fibers prior to densification. This method has been used successfully in fiber-reinforced polymer matrix composites (PMCs) (Lin and Lee, 1992; Nakai

et al., 2001) and in ceramic composite (Marshall and Cox, 2008). One way of achieving this goal is to insert fugitive rods of prescribed diameter into the fiber preform at the intended locations of holes, and then introduce the matrix with the rods in place. The rods can be inserted either (i) after weaving, by deflecting fiber tows around the rod (without causing significant damage to the fibers), provided the rod diameter is comparable to the fiber tow size, or (ii) during weaving, using a modified local weave structure around the rod for larger holes (Marshall and Cox, 2008). The end result is a composite with continuous, unbroken fibers around the holes. When introduced in this manner in PMCs, the holes have been found to have a smaller effect on the knockdown in tensile strength relative to that when holes are machined after processing has been completed (Lin and Lee, 1992; Nakai et al., 2001). In CMCs, there is an additional benefit of avoiding exposure of cut fibers to the service environment. These benefits are especially important in applications where rows of closely spaced holes are needed, as in many turbine combustors and blades.

In this study, the effects of small holes and shear defects on the tensile properties of a woven, anisotropic C/SiC CMC are investigated. The holes are introduced by the two methods described above: notably, by insertion of rods into the woven preform before adding the matrix and by conventional machining after fabrication. Systematic shear defects are introduced into a woven preform (after weaving) by manually shearing the preform up to the

point of lock-up. The effects of rod insertion and shear defects on local tow distortions are probed through analysis of high-resolution optical scans of the partially-processed composite. Following this, tensile tests are performed using digital image correlation (DIC) to characterize the surface displacement and strain fields of specimens containing features and defects. Their performance is evaluated in comparison to that of pristine specimens (presented in Chapter 3).

5.2 Material system and weave characterization

5.2.1 Material structure and fabrication

The materials of interest in this study are variants on the fully-processed, small unit cell composite described in Chapter 2. Details of the composite microstructure are shown in Figures 2.4 and 2.5. Weave defects and features were introduced either by manipulation of the fabric preform or machining of the fully-processed composite.

Small holes were introduced into the composite in two ways. In the first, holes were machined into specimens using a 1 mm-diameter diamond jewelers drill in a CNC mill. The mill had been programmed to make 5 µm advances with intervening coolant flushes to minimize damage. The resulting

holes were 1.0–1.2 mm in diameter.

In the second, holes were created within the fabric preform *prior to CVI*. This was accomplished by gently inserting graphite rods, with smoothly pointed ends and diameter 2 mm, through the fabric preform at select locations. Through this operation the tows surrounding the rod were displaced laterally by a small amount with minimal fiber damage. The rods were removed after the pyrolytic carbon coating step, leaving behind approximately circular holes within the partially processed preform (Fig. 5.1(a)). The resulting holes were 1.6–2.0 mm in diameter.

A sheared preform was created by first taking a pristine fabric preform and clamping it along the two edges parallel to the weft tows. While fixing one edge, the opposite edge was displaced parallel to the weft tows. The preform was sheared until "lock-up": the point at which it resists further motion due to contact between neighboring tows. Graphite rods were subsequently inserted through the sheared preform at the locations seen in Figure 5.2 to secure the preform during subsequent CVI processing.

Processing of the sheared preform and the preform containing holes was halted after the CVI processing stage. The panels were then characterized using procedures outlined below. Following characterization, the panels were densified using the same slurry and PIP processes used for the pristine com-

posites.

5.2.2 Characterization of weave structure

The effects of weave distortions—due to insertion of rods into the preform or introduced shear defects—on tow locations were characterized by measuring the deviations of the warp crown locations from their ideal positions in a perfect panel (Rossol et al., 2014). The locations of the warp crowns were identified from high resolution (1200 dpi) scanned optical images of the partially-processed panel (after the CVI SiC processing step mentioned above) using a computational feature-finding algorithm and analyzed following a procedure developed previously by Rossol et al. (2014).

The features of interest—in this case the warp crowns—were identified in the following way. First, a set of n representative images of warp crowns were selected randomly from the entire image. Next, using a template matching algorithm, potential matches for each of the n images (or templates) with features on the image were identified. For each successful match, the template location (once aligned with the features) was used as an estimate of the warp crown location. Positive matches were grouped spatially and the average position of each group was computed. Additionally, the match probability (i.e. the fractional number of templates that had been matched to each

warp crown) was also computed. Features with a match probability of $< 10\,\%$ were deemed to be false positives and were therefore excluded from further analysis. Following this procedure, about 99 % of warp crowns were correctly identified; the remaining crowns and their locations were identified manually. Segments of incomplete tows at the panel edges were excluded from the analysis, thereby yielding a rectangular data array.

Once identified, the warp crown locations were used as fiducial markers of the underlying tow locations. The coordinates (x_i, y_i) of each crown were compared with the expected coordinates $(\overline{x}_i, \overline{y}_i)$ in an ideal orthogonal weave in order to calculate the local deviation (u_i, v_i), defined by:

$$(u_i, v_i) = (x_i, y_i) - (\overline{x}_i, \overline{y}_i) \tag{5.1}$$

The parameters characterizing the unit cell of the ideal weave were computed from a corresponding set of measurements on a separate panel (without holes or intentional defects) made in the same weaving run, as detailed by Rossol et al. (2014). The cell dimensions of the latter panel were taken as the average separation distances between nodes in the x- and y-directions and taking the ideal angle between warp and weft tows to be 90°. Once such cell is illustrated in Figure 2.2.

Local variations in the tow positions were amplified using spatial differentiation as a filter (Rossol et al., 2014). The spatial derivatives were calculated

at each nodal location within the data array from the slopes of linear fits to the deviation fields, $u(x,y)$ and $v(x,y)$, over an area equivalent to one unit cell of the weave structure centered on each nodal location (Fig. 2.2(a)). The spatial derivatives $\delta_{xx} = \partial u/\partial x$ and $\delta_{yy} = \partial v/\partial y$ give direct measures of the local variations in packing density of weft tows and warp tows, respectively.[1] The other derivative, $\delta_{xy} = (\partial u/\partial y + \partial v/\partial x)/2$, is a measure of the rotation of the two tow populations with respect to each other relative to that in a perfect orthogonal weave (Rossol et al., 2014).[2] Maps of these spatial derivatives are show in Figures 5.1 and 5.2(b-d) for the panel with holes and the sheared panel, respectively. For comparison, results for a smaller pristine panel made from the same weaving run are shown in Figures 5.2(f-h). Measurements of average values and standard deviations of these derivatives for three composite panels—one with an array of holes introduced using graphite rods, one with intentional shear defects, and the third without holes or intentional shear defects (from an earlier study by Rossol et al. (2014))—are summarized in Figure 5.3.

[1] $\delta_{xx} = \rho^0_{weft}/\rho_{weft} - 1$, where ρ_{weft} is the packing density of the weft tows and ρ^0_{weft} is the average packing density of the weft tows. Similarly, $\delta_{yy} = \rho^0_{warp}/\rho_{warp} - 1$.

[2] δ_{xy} = half of the cotangent of the angle between warp and weft tows.

Panel with holes

The variations in δ_{xy} in all panels are predominantly long-range in nature. In the panel with holes a nearly-uniform gradient is evident from the top left to the bottom right in Fig. 5.1(b). As discussed by Rossol et al. (2014), the non-zero values of δ_{xy} are attributable to shear of the panel from handling after weaving, which causes the angle between warp and weft tows to deviate from 90°. Its average value ($\delta_{xy} = -0.014$) corresponds to an angle of 88.4° between the warp and the weft tows, whereas its standard deviation corresponds to a range from 87° to 90°. These values are only slightly larger in this panel than those in the panel without holes. It is evident from Figure 5.1(b) that local deformation of the preform due to the presence of the holes does not contribute significantly to the mean and standard deviation of δ_{xy} since the disturbance to the δ_{xy} field due to the holes is small in magnitude and localized to a very small area surrounding each hole.

The spatial variations in δ_{xx} and δ_{yy} are characterized predominantly by periodic *short-range* fluctuations over length scales of a few multiples of the unit cell dimensions. These fluctuations are manifested in the form of bands of either dilation (positive δ) or compaction (negative δ). Additionally, very near the holes, δ_{yy} (≈ 0.05) is about an order of magnitude greater than average; the effect persists over an apparent distance of about one unit cell away

from the holes (see inset on Fig. 5.1(d)). (Since the strains are computed over distances equal to the unit cell dimensions, the apparent strain within an individual cell can be the result of a large displacement of *a single warp crown* adjacent to the hole. Indeed, this appears to be the case for many of the holes in Figure 5.1(a)). In contrast, the local values of δ_{xy} and δ_{xx} are elevated only very slightly relative to their respective averages (insets in Figs. 5.1(b) and (c)).

The fact that the local deviation of the warp packing density (δ_{yy}) adjacent to the holes is significantly greater than that of the weft packing density (δ_{xx}) suggests greater positional correlation between neighboring warp tows than that between neighboring weft tows. This occurs because of the topology of the weave. The warp weavers lie on the relatively straight weft tows allowing for lateral sliding, resisted mainly by compression of neighboring warp tows. The weft tows, on the other hand, are constrained laterally by the interlocking warps under the crossovers but are unconstrained between these points. Lateral motion of the weft tows must be transmitted to its neighboring wefts through the interlocking warp network over length-scales longer than a unit cell. Within a unit cell, each surface weft is not in direct contact with its neighboring surface wefts. Instead, a sizeable gap (ca. 1 mm) exists between adjacent surface wefts, as evident, for example, in Figure 2.4(a). Consequently, large lateral displacements would be required in any one weft tow in order to cause displacement of neighboring surface weft tows.

Sheared panel

In the sheared panel, δ_{xy} (characterizing tow rotation) appears to be uniform over most of the left side and most of the right side of the panel (Fig. 5.2(b)); here it varies over the range of about -0.04 to -0.05. The central vertical region exhibits lower values. By comparison, measurements on the pristine panel yields an average value of 0.003: more than an order of magnitude smaller. Also present in the central region is a band about 30 mm wide in which δ_{xx} is, on average, about 0.09: much higher than that in surrounding regions. This indicates a local reduction in the weft packing density by about 9 %. It is surmised that the band had formed after shear lock-up had occurred; further deformation was then accommodated by preform *extension* along the warp direction rather than by additional tow rotation.

Apart from the band of extension along the panel center and a corresponding band of contraction on the far left edge of the panel, δ_{xx} does not exhibit obvious long-range variations. Instead, the fluctuations that are present exist as bands of slight contraction or extension oriented parallel to the weft direction; the bands are approximately periodic with a wavelength of a few multiples of the unit cell dimension. The quantity δ_{yy} exhibits similar short-range fluctuations, again manifest in bands of slight contraction or extension, but now oriented parallel to the warp direction. These, too, exhibit a wavelength

equal to several times the corresponding unit cell dimension. In light of these observations, specimens for tensile testing were machined from the left side of the panel where the deviations (especially δ_{xy}) are approximately constant, as indicated on Figure 5.2(a).

The average values of the derivatives were computed for the entire sheared panel and for only the left side of this panel (from which the test specimens were cut). These are compared with the average values obtained for the pristine panel in Figure 5.3. Although the average values of δ_{xx} and δ_{yy} are essentially the same in the two panels, the standard deviations of these quantities in the sheared panel are about twice those in the pristine panel. This suggests that some additional (though small) local variability may have been introduced during the shearing operation. In contrast, δ_{xy} in the sheared panel is significantly higher in magnitude; its average value on the left side of the panel is -0.042. The corresponding tow misalignment angle is $\theta = \tan^{-1}(2\varepsilon_{xy}) = -4.8^{\circ}$. The standard deviation on this quantity is indistinguishable from that of the pristine panel. The implication is that the short-range variations in shear had not been affected by the shearing operation.

The orientations of the test specimens in the sheared panel were selected to probe two effects. The first is the effect of misorientation of nominally transverse tows. It was elucidated from test specimens in two orientations; (i) *paral-*

lel to the weft direction (denoted "|| weft"), with the warp tows inclined at 4.8° to the transverse direction, and (ii) *parallel to the warp direction* (denoted "|| warp") with the weft tows inclined at 4.8° to the transverse direction. The second involves the role of misalignment in nominally axial tows when load is applied normal to the transverse tows. This was achieved with specimens oriented *perpendicular to the warp axis* (denoted "⊥ warp") where the weft tows are inclined at 4.8° to the loading direction. These test orientations and the angles θ_{warp} and θ_{weft} that the warp and weft tows make with the loading directions are summarized in Figure 5.4. (The designations in this figures are employed in analyses presented in a subsequent section.) Tensile test results for these three orientations were compared with those of the pristine panel in the warp and in the weft directions.

5.3 Mechanical Properties

5.3.1 Measurement Methods

The testing procedure used in this study is identical to that used for the tensile tests described in Chapter 3. A brief summary follows.

Dogbone-shaped tensile specimens were cut from the panel with holes along both the warp and the weft tow directions. Specimens were cut from the

sheared panel in the three orientations noted above: (i) parallel to the warp tows, (ii) parallel to the weft tows, and (iii) perpendicular to the warp tows. The gauge sections of all specimens was 25.4 mm long and 12.7 mm wide. The holes (when present) were situated at the center of the gauge section. In preparation for strain mapping by digital image correlation (DIC), one face of each specimen was painted white; a black speckle pattern was then created using an airbrush. The regions probed by DIC were 16–17 mm long (centered along the gauge length) and encompassed the full specimen width. The resulting magnification of the DIC images was 7.1–8.3 µm/pixel. Successful correlation was obtained over the entire area of interest using a subset size of 43–45 pixels (320–360 µm). Two specimens of each type and orientation were tested in uniaxial tension at a nominal strain rate of $1 \times 10^{-5}\,\mathrm{s}^{-1}$ at room temperature. All specimens failed within the gage section.

The global axial strain ε_{yy} was calculated using a linear fit of the axial displacements $V(x,y)$ calculated at all nodal locations within the correlated region ($\varepsilon_{yy} = \partial V(x,y)/\partial y$). These were found to be in good agreement with strains measured by axial virtual extensometers as well as the average value of axial strain at all nodal locations. At high applied stress some discrepancies are found with the field-averaged strain, possibly due to the presence of large cracks skewing the average strain upwards. For consistency, comparisons in macroscopic mechanical response are made on the basis of the

displacement-field strains and the remote tensile stress. In specimens from the composite with shear defects, similar fitting procedures were used to compute the average shear strain ε_{xy} from the displacements $U(x,y)$ and $V(x,y)$, *i.e.* $\varepsilon_{xy} = (\partial V/\partial x + \partial U/\partial y)/2$ and $\varepsilon_{xx} = \partial U/\partial x$.

The DIC data were also used to map the spatial distributions of ε_{yy}, ε_{xx} and ε_{xy}. These strains were computed at each nodal location using commercial software (VIC-3D 2010, Correlated Solutions Inc., Columbia, SC). The results are presented as full-field strain maps. The boundaries of underlying fiber tows (discerned from topographic DIC data and the scanned preform) are superimposed on these maps.

One additional method was used to probe the influence of holes on axial strains measured in their vicinity. In this instance, strains were averaged over areas defined by the specimen width and a length equal to the unit cell dimension in the loading direction, *i.e.* over a length of 5.1 mm in the weft-oriented specimens and 7.5 mm in the warp-oriented specimens (see insets in Fig. 5.8). The latter averaging procedure was repeated at 1 mm increments over the specimen length. The area-averaged strains were then plotted against the distance d from the hole center (or the specimen center) to the center of the averaging area (also defined by the insets in Fig. 5.8).

5.3.2 Tensile response and strain patterns

The tensile response of the fully-processed, small unit cell composite used as a reference in this study is presented in greater detail in Chapter 3. For the purpose of comparison, its global and full-field strain response has been reproduced here.

Tensile response of specimens with holes

The tensile stress-strain curves for specimens containing holes are plotted in Figure 5.5 in two forms: in terms of the remote stress (in Fig. 5.5(a)) and in terms of the nominal net-section stress (in Fig. 5.5(b)). (The latter is defined such that the ratio of the two stresses is $1 - a/w$.) When couched in terms of remote stress, the specimens with holes exhibit slightly higher compliance over the entire strain range and lower ultimate tensile strength relative to those in their respective unnotched specimens. Additionally, the failure strains of specimens with holes are slightly higher.

When couched in terms of the nominal net-section stress, the stress-strain curves for specimens with woven holes appear to collapse onto the curves for unnotched specimens in both warp and weft directions. Specimens with machined holes exhibit similar trends (with their stress-strain curves coming into closer agreement with the unnotched results), although they appear to lie

consistently slightly below those of the woven holes.

Variations in ultimate tensile strength with hole size are plotted in Figure 5.6. The slight strength reductions associated with the holes can be rationalized to first order on the basis of the reduced net-section area. Assuming a critical net-section stress at fracture (without notch sensitivity), the predictions are in broad agreement with the measurements. Examining the results more closely, however, it appears that, in the weft direction, the net-section strength of specimens with woven holes lie slightly above the predictions, by about 5 %; in contrast, those with machined holes exhibit strengths that are about 5 % lower than the predictions. For tests in the warp direction, specimens with both woven and machined holes consistently lie slightly below the prediction, by about 5 %.

Full-field axial strain maps for these specimens are shown in Figure 5.7, at remote stress levels that correspond to those of the specimens without holes. Here, as in the pristine specimens, the strain fields are characterized by banded patterns reflecting the opening of matrix cracks. Within the resolution of the present measurements, the patterns appear to evolve independently of the holes. That is, there does not appear to be an increased propensity for cracking in regions of high stress concentration adjacent to the holes. If the holes behaved as stress concentrators, the strains would be highest along the trans-

verse plane containing the hole and would diminish rapidly with distance from the hole to the far field value: the latter being comparable to the strain obtained in the pristine (unnotched) specimen at the same applied stress.

An additional attempt at quantifying the preceding effects was made by examining the variations in axial strain averaged over one unit cell length with axial distance from the hole center. This exercise is based on the expectation (previously noted) that the strains should be elevated in the vicinity of the holes and should diminish in regions remote from the holes. The results are plotted in Figure 5.8. Interestingly, in both orientations of the pristine specimens, the strains exhibit a periodic (nearly-sinusoidal) pattern with a wavelength that is virtually identical to the respective unit cell dimension (*i.e.* 5.1 mm in the weft direction and 7.5 mm in the warp direction). The amplitude of the variation is about 10 % of the average strain in the weft direction and 20–30 % in the warp direction. The implication is that the computed strains are sensitive to the starting and ending points used in defining the local gauge length (even though their separation distance is constant). This is likely associated with the small number of cracks (typically about 5-8) over the local gauge length as well as the variations in the opening displacements of the cracks (evident in Fig. 3.8).

As with the unnotched specimens, the strain distributions of specimens

with holes exhibit periodic patterns with wavelengths similar to the pertinent unit cell dimension. The patterns also reveal effects of the holes. Specifically, the strain distributions appear to be a convolution of the periodic variations associated with the weave geometry and the more-local effects of the holes near the specimen centers. Although the strains for the unit cells centered on the holes (at $d = 0$ in Fig. 5.8) are elevated somewhat in most specimens, the longer range effects of the holes appear to be masked by the effects of the weave. Furthermore, since the data probe regions that are only a relatively short distance from the hole (selected to maximize strain resolution), the average composite strains remote from the hole could not be ascertained.

Further insights into the operative damage mechanisms were gleaned from maps of the full-field *transverse* ε_{xx} *and shear strains* ε_{xy} at high stresses, shown in Figure 5.9. Several features are noteworthy. First, when loaded in the warp direction, the composite exhibits vertical bands of compressive transverse strains along the center of each warp tow (blue bands indicating strain of $\sim 0.5\,\%$), likely produced by closing of pre-existing matrix cracks aligned with the loading directions (see, for example, Figs. 2.4(b&e)). Conversely, bands of transverse *tensile* strains are obtained in the weft tows, indicative of crack opening. The latter effects appear somewhat more pronounced in the specimens with holes, especially the holes that had been woven. Similar effects are obtained in the weft-oriented specimens. In this case, bands of compressive

strain are obtained at the center of some of the weft tows and bands of tensile strain in some of the warp tows, although their prevalence is lower than those in the warp specimens. The effects become more pronounced in the presence of holes, especially in regions near the hole. Here, again, given the resolution of the measurements, the rather short specimen length and the large unit cell size, the local effects attributable to the holes cannot be readily ascertained.

Similar trends are obtained in the shear strain distributions. They consist of two families of inclined bands of positive and negative shear. Their magnitude increases in the presence of holes, especially in regions close to the hole. Of particular note is the response of the weft coupon with a machined hole, which exhibits a pattern of inclined shear bands extending vertically above and below the hole. This is suggestive of shear transfer to the cut tows passing through the hole.

Tensile response of specimens with shear defects

The tensile stress-strain curves are plotted in Figure 5.10. Maps of axial strain ε_{yy} are depicted in Figure 5.11 for several stress levels: 50 MPa, 150 MPa and 300 MPa for tests performed in the nominally weft direction, and 40 MPa, 75 MPa and 100 MPa in the warp direction. Additional insights are gleaned from maps of the transverse strain ε_{xx} and the in-plane shear strain ε_{xy}, shown

in Figure 5.12 for stress levels close to those needed for fracture: 300 MPa in the weft direction and 100 MPa in the warp direction. Pertinent observations follow.

The tensile stress-strain curves for weft-oriented specimens from the sheared and the pristine panels are indistinguishable from one another. Full-field maps of strains (two left columns in Figs. 5.11 and 5.12) for these two cases are also indistinguishable from one another. The shear strains are small in both cases, indicating minimal rotation of the transverse (warp) tows during testing.

When loaded perpendicular to the weft tows, the stress-strain response of the sheared panel initially follows that of the pristine material, up to about 150 MPa. Thereafter the curves diverge: the sheared panel exhibiting more rapid softening and a failure stress that is about 20 % lower than that of the pristine material.

Maps of the axial strains (middle column in Fig. 5.11) provide corroborating evidence. That is, the bands of intense strain are similar in the pristine and the sheared panel up to about 150 MPa; at higher stresses, the density and the width of the bands in the sheared panel become noticeably greater. The bands are also arranged into diagonal patterns that correlate with the warp crown locations. Interestingly, the shear strains become much more pronounced as

well (Fig. 5.12). Here the strains are again concentrated within narrow bands, coincident with those of the axial strain. Indeed, the local shear strain can be attributed to the opening of cracks that are inclined at a finite angle relative to normal. That is, the displacement jumps at inclined cracks will appear as variations in V with x (and hence shear strain). This mechanism also produces positive transverse strains, as evidenced by Figure 5.12. The average shear strains, plotted against axial strain in Figure 5.13(a), are clearly much higher than those of the two preceding test orientations.

When loaded parallel to the warp direction, the sheared panel exhibits a soft response relative to that in the weft direction, but only slightly below that of the pristine material in the warp direction. Surprisingly, the failure strain in the sheared panel is greater than that of the pristine panel: 0.8 % vs 0.6 %. The axial strain maps for these two cases (in the two right columns in Fig. 5.11) are similar, though the sheared panel exhibits somewhat higher values near fracture. The origin of the strain difference is more apparent in line scans of axial displacement, $V(y)$, plotted in Figure 5.14. The scans indicate that, although the crack densities are virtually indistinguishable, the opening displacements of cracks in the sheared panel are noticeably greater than those in the pristine panel. Here, again, the local shear and transverse strains are elevated in the regions containing cracks; the average shear strains (Fig. 5.13(b)) are also greater.

5.4 Analysis of sheared composite response

Rudimentary analyses have been performed to rationalize the experimental trends, with emphasis on the role of initial tow misorientation and tow rotation during both elastic and inelastic straining. The first is an elastic analysis based on classical laminate theory. A schematic of the laminate idealization is shown in Figure 5.4. Details of the analysis are presented in Chapter 3 and Appendix B.

Following the effective medium calibration and calculation of the warp and weft ply properties, one of the two ply types is rotated by 4.8° to match the misorientation angle between the warp and weft tows in the sheared panel. The engineering elastic constants for the latter laminate are computed for uniaxial tensile loading in the three orientations of interest.

Applying the procedure to nominally *weft*-oriented loading yields composite Youngs moduli of 103.4 GPa, 103.3 GPa and 102.6 GPa in pristine weft, parallel-to-weft and perpendicular-to-warp directions, respectively. Evidently the small misorientations in the warp tows in the starting preform have negligible effect on the Youngs modulus (within about 0.5 %).

Applying the procedure to loading in the *warp* direction yields essentially the same conclusion, but with one complication. Here the predicted Youngs moduli in the pristine and the sheared panels are 74.8 GPa and 75.1 GPa, re-

spectively (within 0.3 % of one another). As with the laminate analysis presented in Chapter 3, the predictions overestimate the measured moduli (60–65 GPa) because tow waviness has not been accounted for. When the knockdown factor η (described in Chapter 3) is applied to the warp ply, the predicted composite modulus becomes $E_C \approx 61$ GPa: much closer to the measured value.

Notwithstanding the discrepancy between the predictions of the simple laminate analysis (assuming straight fibers) and the experimental measurements, the *relative* values of predicted moduli of the pristine and the sheared panels in this orientation are expected to be approximately correct, since the reductions caused by tow waviness are the same in both cases. That is, despite tow waviness, both the sheared and the pristine panels should exhibit essentially the same stiffness in this orientation.

The laminate model also yields predictions of the elastic in-plane *shear strains*; the predictions are compared with the experimental measurements in Figure 5.13. Since the pristine material is represented by a cross-ply laminate without shear-normal coupling, its shear strain is identically zero. The predicted shear strains for loading parallel to the warp or parallel to the weft directions in the sheared panel are positive but exceedingly small in magnitude (*e.g.* the shear strain is about 0.01 % for an axial tensile strain of 1 %).

By comparison, the measured shear strains are as much as an order of magnitude greater. The elastic predictions are somewhat greater for loading of the sheared panel perpendicular to the warp direction (*e.g.* about 0.06 % at a tensile strain of 1 %), but these, too, are an order of magnitude lower than the measured values. The conclusion is that, although the shear-normal coupling in the sheared panel yields a finite elastic shear strain, the predicted values are far too small to rationalize the experimental measurements. The inference is that the shear strains are attributable to *inelastic* phenomenon, probably involving matrix cracks.

To glean some insights into the origin of the shear strains, the laminate model was adapted in an approximate way to the inelastic domain. This was done by considering the effects of matrix damage and in particular the shear stresses that arise from shear-normal coupling on the instantaneous matrix modulus and, in turn, the effects of the modulus change on the pseudo-inelastic shear strain. Absent any information on the evolution of the average matrix modulus with strain, calculations were performed using several (fixed) values of E_m, from 80 GPa down to 10 GPa. The results, plotted in Figure 5.13, show that the shear strain is sensitive to E_m, since the constraints to shearing and tow rotation are controlled largely by the matrix phase. The results suggest that, because of damage, the matrix modulus may have been reduced by as much as an order of magnitude from its initial value. The non-linearity

in the experimental curves is likely due to the progressive increase in matrix damage and, in turn, a progressive degradation in its modulus.

The reduction in the ultimate tensile strength (UTS) of specimens loaded *perpendicular to the warp* direction can be rationalized on the basis of the reduced fraction of continuous weft tows that traverse the entire gauge length, along with the hypothesis that axial load is not transferred to the fibers that do not traverse the entire gauge length. The effect is shown schematically in Figure 5.15. From geometry, the ratio of continuous fibers in the sheared and the pristine panels is given to first order by $1 - 2L\delta_{xy}/W$. Combining with the pertinent numerical values ($W = 12.7\,\text{mm}$, $L = 25.4\,\text{mm}$ and $\delta_{xy} = 0.042$) this yields a ratio of 0.83. That is, 83 % of the weft fibers in the present tensile specimens are continuous along the entire gauge length; the remaining 17 % terminate at one of the two cut edges. The UTS should be reduced proportionately. Indeed, the ratio of the two measured strengths is about 0.8, consistent with the prediction.

The preceding effects can also be used to rationalize (albeit only qualitatively) the stress-strain response in the nominally weft orientation—particularly the initial correspondence with that of the pristine material—in the following way. At sufficiently low stresses, the composite deforms essentially homogeneously with elastic properties that are predictable (at least

approximately) by laminate theory. Furthermore, since the Young's modulus in this orientation is predicted to be essentially the same as that of the pristine material (as demonstrated above), the stress-strain curves should initially coincide. Indeed, the stress-strain curves in this orientation are initially indistinguishable from one another, even following a finite amount of inelastic straining. However, as matrix damage progresses, the fiber segments that are not continuous along the entire gauge length become increasingly de-coupled from the rest of the composite, leaving the regions with continuous fibers dominating the macroscopic response. This de-coupling is manifest in: (i) reductions in axial strains to almost zero in some near-edge regions at the highest stress (Fig. 5.11), indicating axial unloading; and (ii) bands of positive transverse strains near the specimen edges (Fig. 5.12), presumably due to slight splaying of the near-edge segments. As this occurs, the response would be expected to transition to that of a composite with a reduced axial fiber volume fraction, eventually breaking at a reduced axial stress, as described in the preceding paragraph.

The origins of the effects of tow misalignment on the failure strain in the *warp* orientation are not presently understood. The two features of interest are: (i) greater softening in the sheared panel over most of the stress-strain history and (ii) an elevated failure strain (from 0.6 % to 0.8 %). One plausible explanation is that the inelastic shear strains associated with rotations of nominally

transverse (weft) tows result in additional matrix damage and hence increased softening. The softening, in turn, may mitigate the bending stresses that otherwise arise when the warp tows attempt to straighten, thereby allowing a greater degree of straightening to occur before the stresses in the warp tows (from tension plus bending) reach the critical value for fiber bundle rupture.

5.5 Discussion and Conclusions

Holes can be introduced into the fiber preform prior to matrix infiltration, thereby minimizing the extent of fiber damage (relative to that obtained when the holes are machined after processing). The holes produced in this manner cause negligible distortion of the surrounding weft tows and only small changes in warp tow packing density. In light of the resolution of the measurements and the observation that the apparent disturbances in warp packing persist only over distances of about one unit cell, the nature and magnitude of the disturbance cannot be characterized completely using the methods employed here. However, optical examinations of the weave in the vicinity of the holes confirm that the effects are indeed very localized.

The ultimate tensile strength of the composite exhibits only a weak sensitivity to the presence of small holes (1–2 mm in diameter), regardless of the manner in which the holes are introduced. Nevertheless, woven holes appear

to be less detrimental to strength in the weft direction than those that had been drilled (by about 10 %). The effects can be attributed to the fact that the tows in specimens with woven holes are largely displaced laterally (and perhaps in the through-thickness direction) and thus continue to contribute to the load-bearing capacity. Such effects appear to be small for loading in the warp direction.

When averaged over a unit cell length, the axial strains in specimens with holes exhibit convoluted effects of the weave geometry and the concentration associated with the hole. The present experiments are insufficient to properly parse these contributions to the strain distributions. Nevertheless, it is interesting to note that when the tensile response is couched in terms of net-section stress and average strain, the results for the woven holes collapse onto those for the unnotched specimens, suggesting a rather long range effect of the holes (at least up to distances of about 1–1.5 unit cells away from the holes). The strains obtained in specimens with drilled holes are consistently higher, a consequence of the absence of fibers in the region of the holes.

The composite has also been found to be insensitive to shear defects. The shear defects have negligible effect on the elastic in-plane properties. This is consistent with the predictions of classical laminate theory. For loadings parallel to one of the two principal tow directions, the tensile response is largely

dictated by the tensile properties of the axial tows; the transverse tows play a decidedly secondary role. Misalignment of the transverse tows is manifest mostly in shear and transverse normal strains. Otherwise, the tensile properties of the composite are not significantly compromised.

For loadings perpendicular to one of the two tow populations, such that the axial tows are slightly misaligned, the effects of misalignment are more pronounced. They give rise to accelerated strain softening (relative to the pristine composite) and a reduced failure stress. The failure stress can be rationalized on the basis of the reduced fraction of nominally axial tows that are continuous along the gauge length. The softening is attributable to progressive decoupling and unloading of the near-edge regions where the tows intersect the cut edges and hence are not continuous along the gauge length. Misaligned axial tows also give rise to fiber rotations that are reflected in elevated shear strains. The magnitude of the shear strains coupled with predictions of a laminate analysis suggest that the average matrix modulus undergoes significant reductions, by as much as an order of magnitude.

Finally, when axial strains are averaged over lengths equal to the unit cell dimensions in the pristine composite, the strains exhibit periodic variations along the loading direction with a wavelength that corresponds closely to the pertinent unit cell dimension. Evidently the representative volume elements

needed to capture the macroscopic material behavior are greater than the unit cell dimensions. The effect is attributable to the rather small number of cracks within each unit cell that control the degree of inelastic strain.

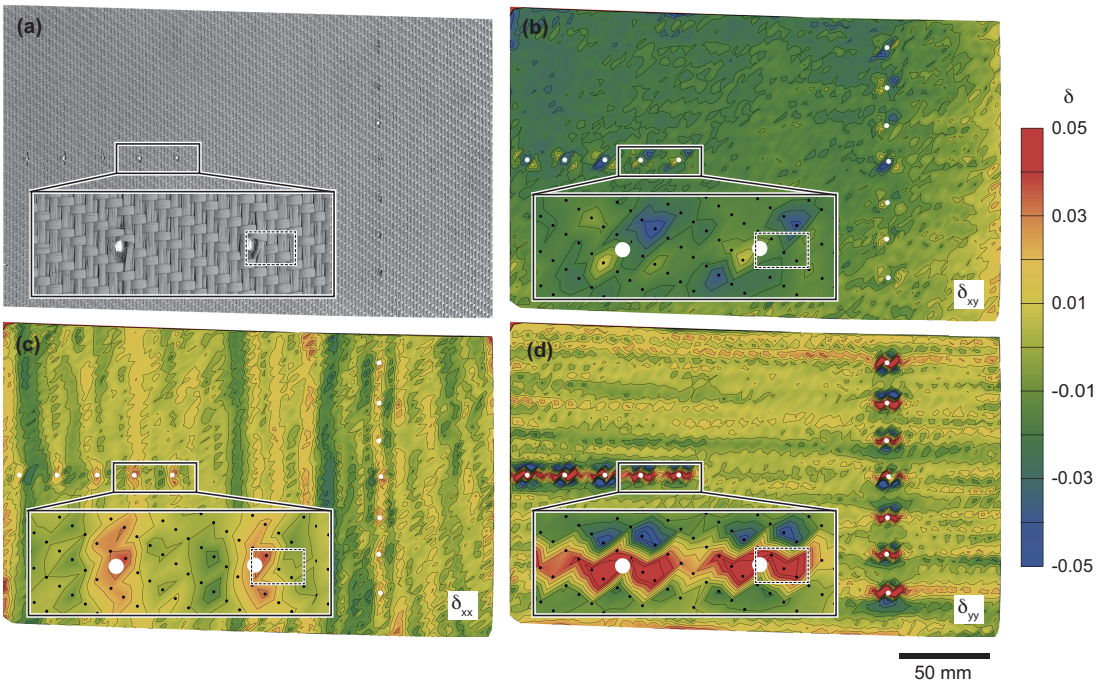

Figure 5.1: (a) Plan view of the panel with woven holes. (b,c,d) Spatial variations of computed δ_{xy}, δ_{xx} and δ_{yy}. Dashed rectangles in the insets represent one unit cell of the weave.

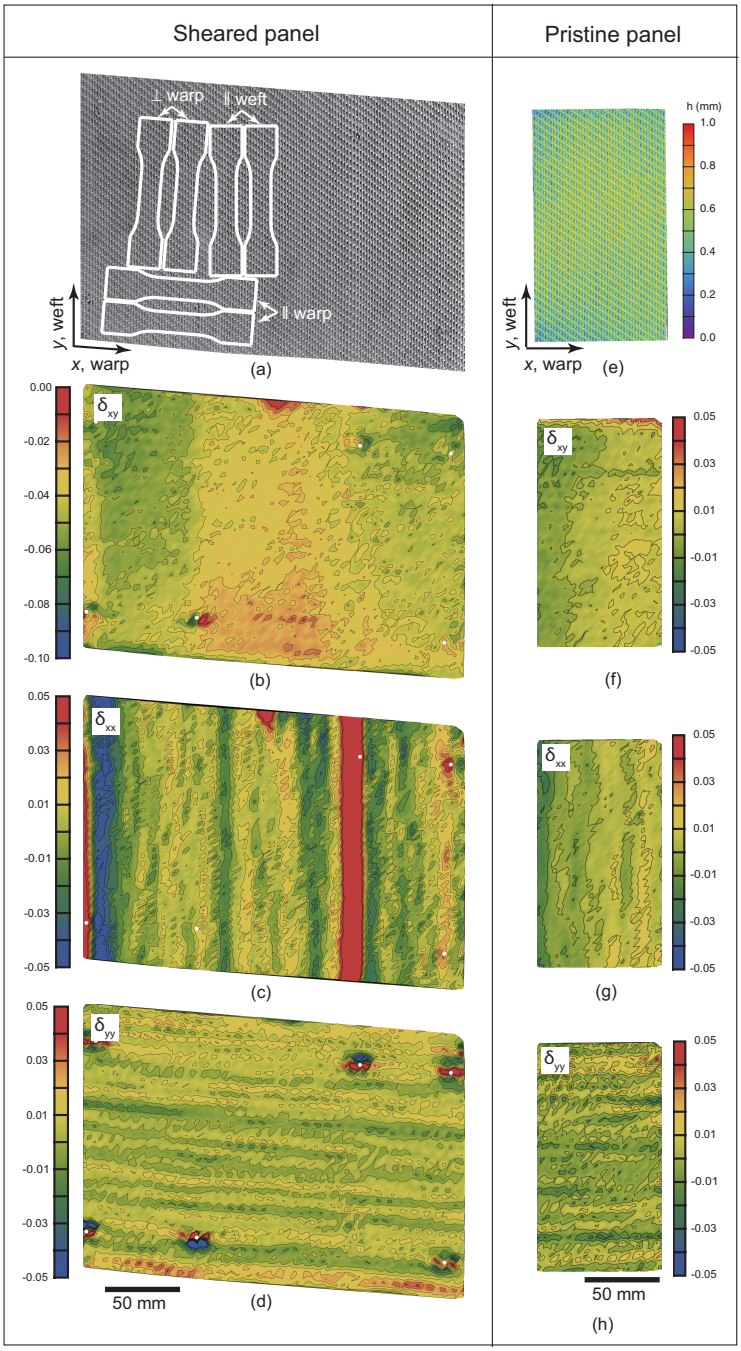

Figure 5.2: (a) Plan view of the sheared panel with dogbone locations indicated and (bd) maps of δ_{xy}, δ_{xx} and δ_{yy}. (eh) Corresponding results for a (smaller) pristine panel prepared from the same weaving run. Image in (e) was constructed using 3D digital image correlation. All figures are at approximately the same scale.

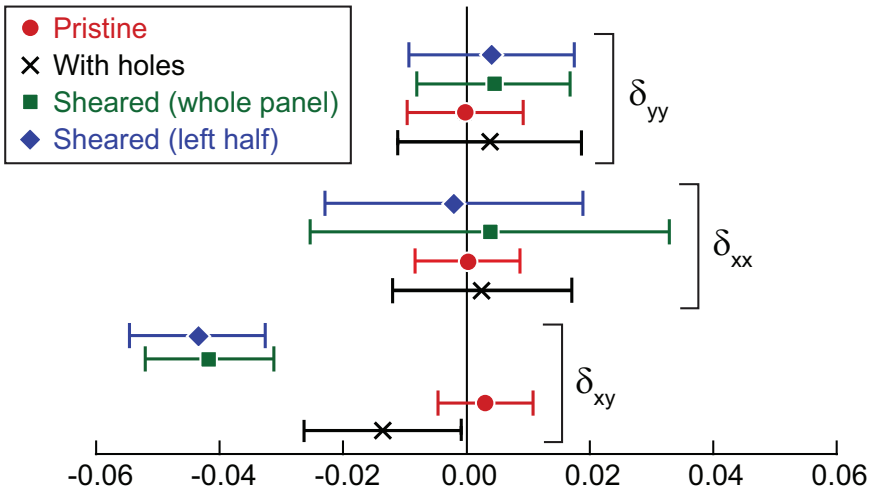

Figure 5.3: Summary of averages and standard deviations of derivatives δ_{xx}, δ_{yy}, and δ_{xy} for panels with holes and shear defects. Data for the whole sheared panel and only the left half of this panel (from which samples were obtained) are shown separately. Also shown for reference are the values for a pristine panel (without holes or shear defects) (Rossol et al., 2014).

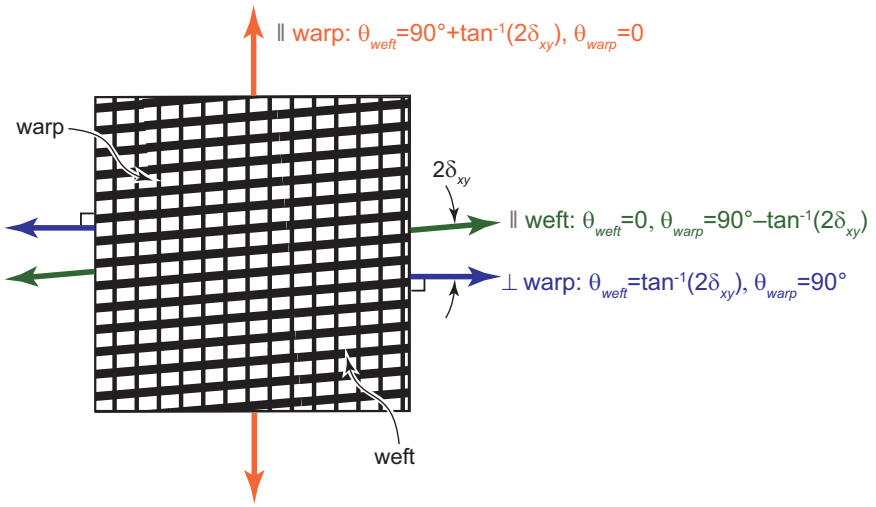

Figure 5.4: Schematic of the laminate idealization of the sheared panel, the loading scenarios of interest, and the angles between the loading directions and the tow axes. The analysis is in Appendix B.

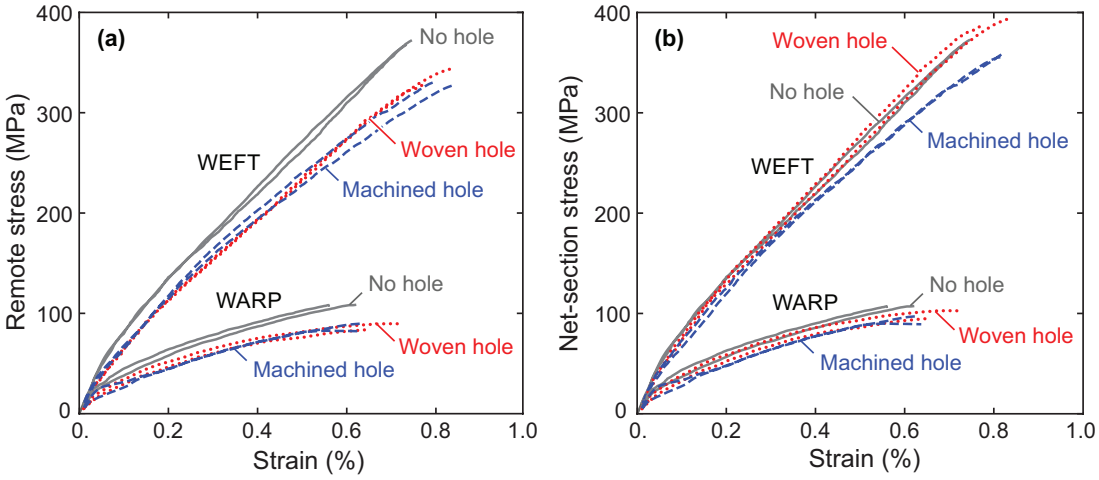

Figure 5.5: Tensile stress-strain response of weft- and warp-oriented specimens containing holes, couched in terms of (a) remote stress and (b) nominal net-section stress. Tensile response of pristine specimens have also been plotted for reference.

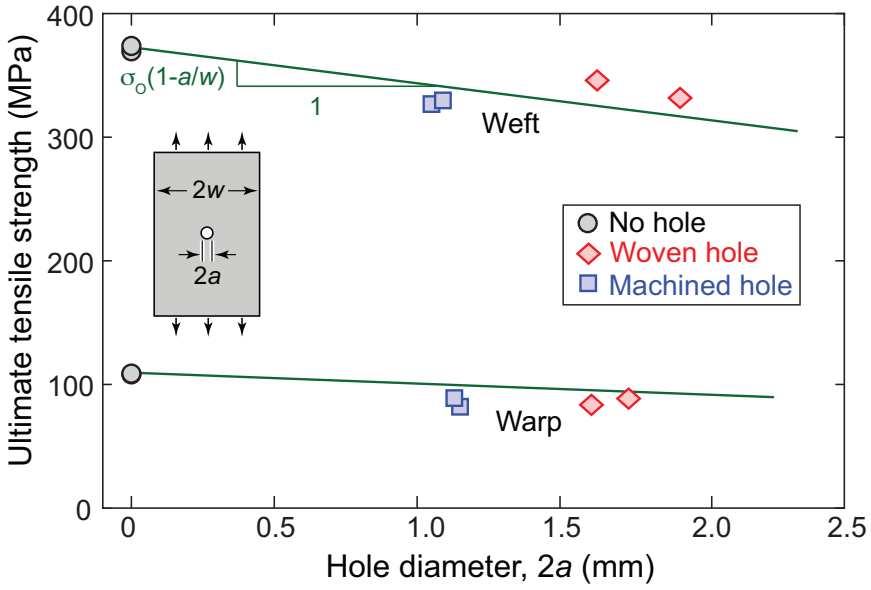

Figure 5.6: Variation in ultimate tensile strength (based on remote stress) with hole diameter in warp and weft orientations. Solid lines represent predictions based on a critical net-section stress at fracture, calibrated using the unnotched tensile strength, σ_0 (at $a = 0$).

Figure 5.7: Full-field axial strains of tensile specimens in weft and warp directions at the stress indicated for specimens containing holes. Underlying tow boundaries are overlayed in white. Dashed rectangles represent the unit cell. Full-field axial strains of the pristine composite have also been plotted for reference.

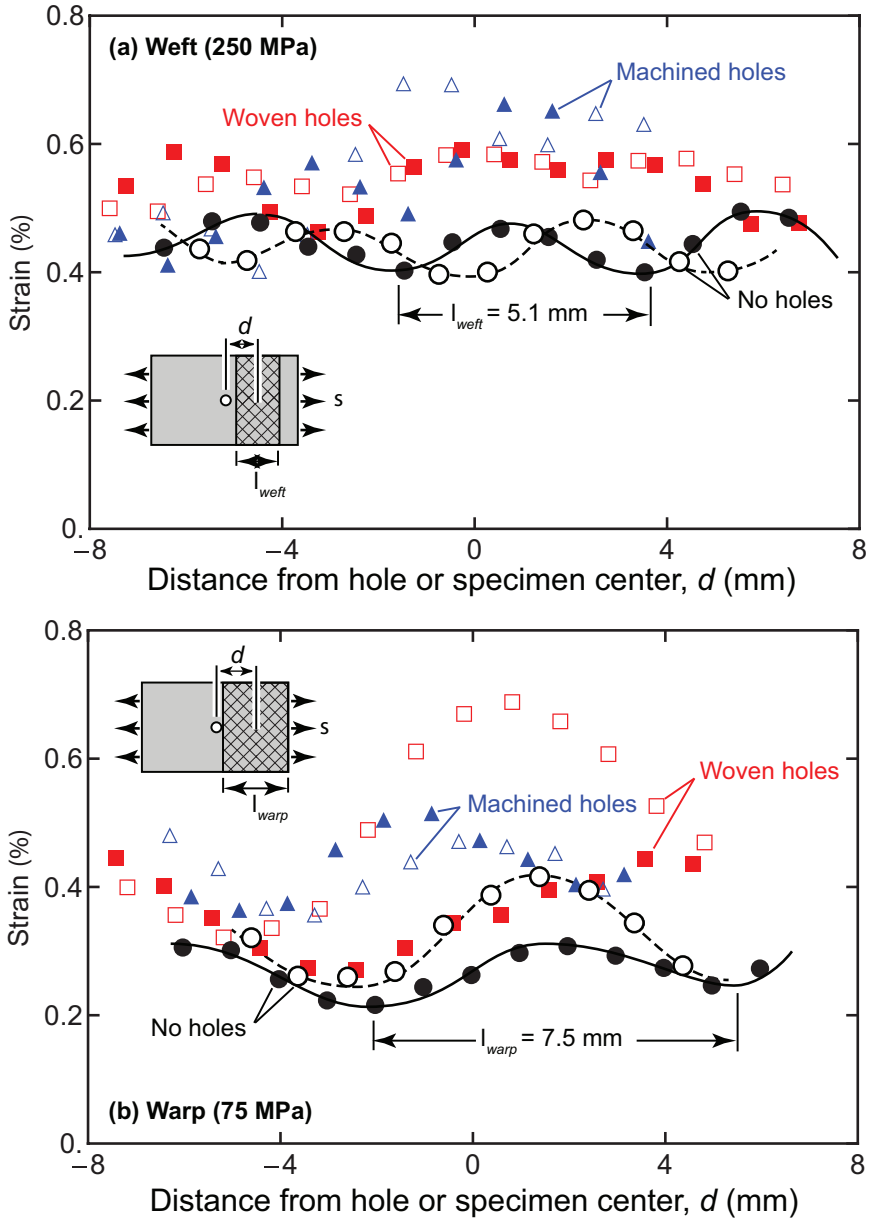

Figure 5.8: Average axial strain as a function of distance from the hole center for (a) weft-oriented specimens at a stress of 250 MPa, and (b) warp-oriented specimens at a stress of 75 MPa. Open and closed symbols correspond to individual specimens within a group. For the specimens without holes, the distance is measured from the specimen center. Dashed and solid curves represent approximate fits to the data sets for specimens without holes. Insets show the areas over which the strains were computed and the manner in which the distance d was ascertained.

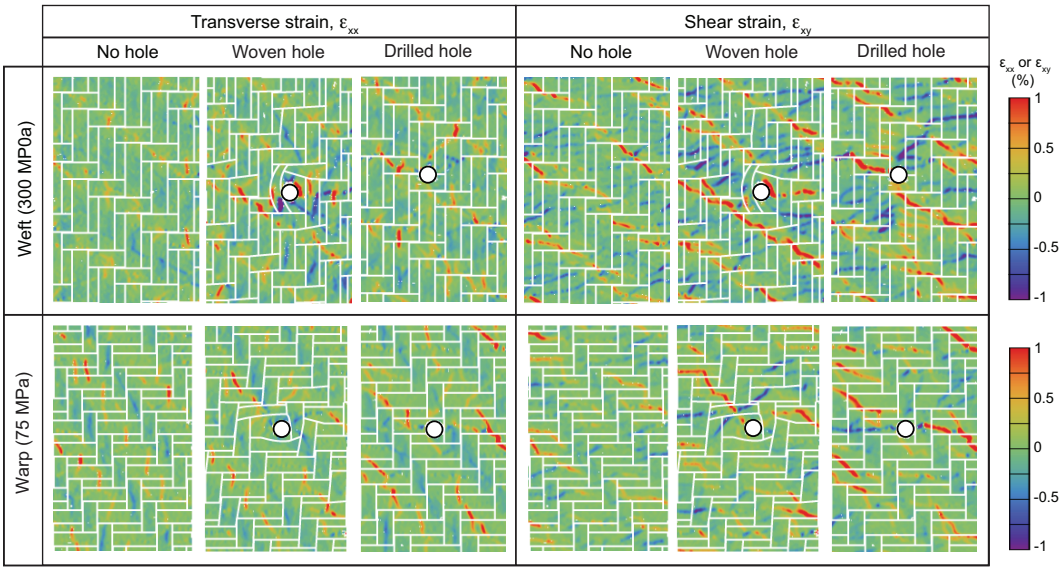

Figure 5.9: Maps of transverse and shear strain fields near the ultimate tensile strength of specimens containing holes in warp and weft directions.

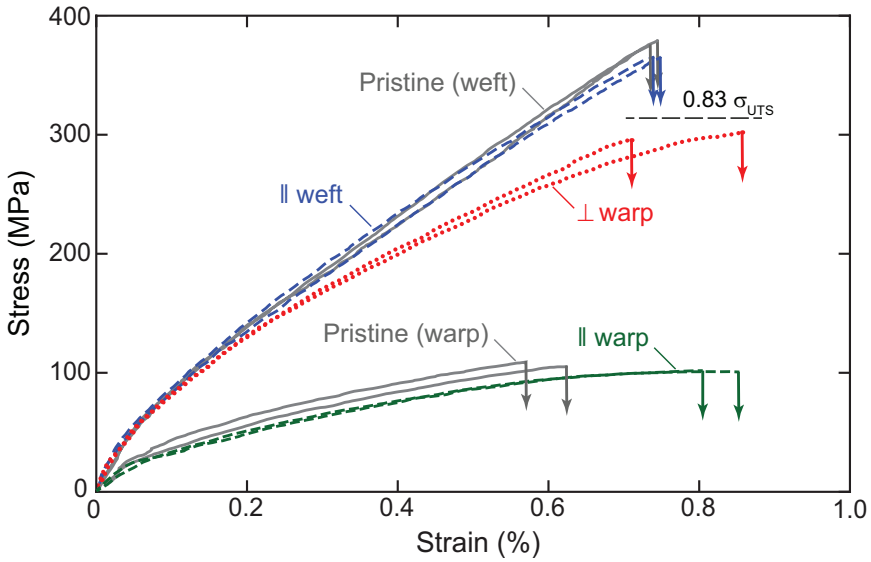

Figure 5.10: Tensile stress-strain response of pristine and sheared composite specimens. Dotted and dashed curves are for the panel in which the preform had been sheared; solid lines are for the pristine (unsheared) panel. The horizontal dashed line indicates the expected reduction in strength of ⊥ warp specimens relative to pristine weft specimens (analysis presented in Figure 5.15).

Figure 5.11: Full-field axial strains of tensile specimens from the sheared composite panel in the (nominally) weft and warp directions. Underlying tow boundaries are overlayed in white. Dashed rectangles/parallelograms represent unit cells. Equivalent contour plots for the pristine specimens have been included for reference. Points A and B denote the end points of the line scan plotted in Fig. 5.14. Arrows in the bottom image of the center column denote near-edge regions where the axial strains are essentially zero. (Note the slight differences in image magnification for the various test specimens.)

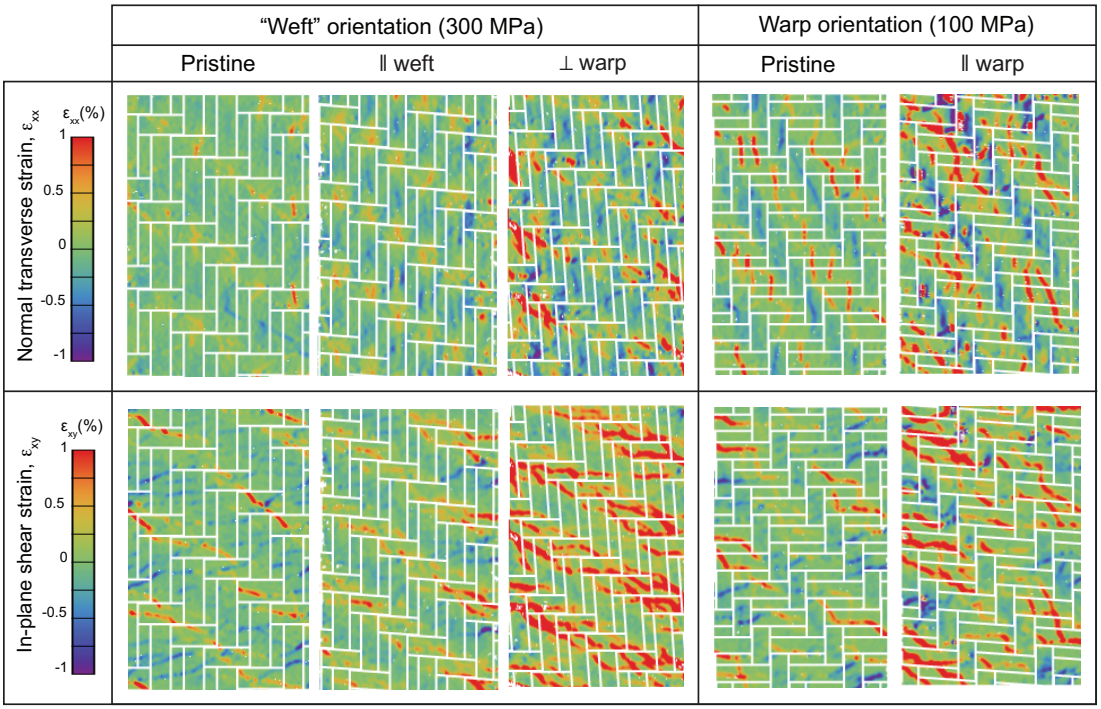

Figure 5.12: Maps of transverse and shear strains near the ultimate tensile strength of specimens from the sheared and pristine composite panels in the (nominally) weft and warp directions.

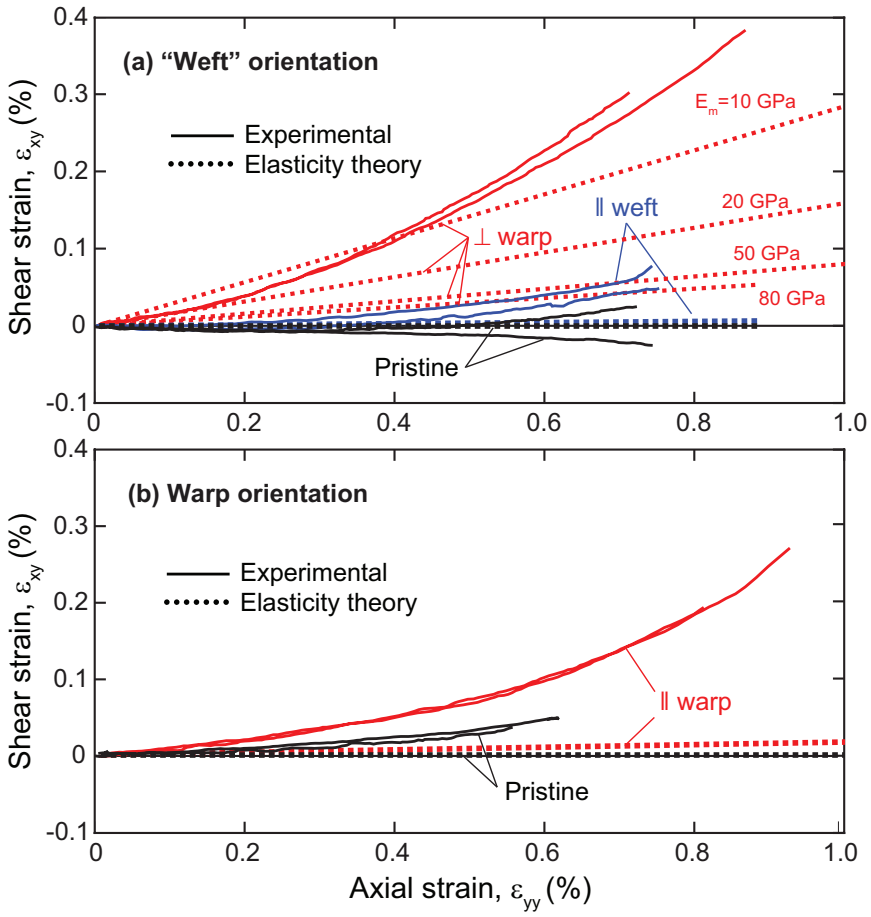

Figure 5.13: Predicted and measured shear strains for specimens from the sheared composite panel tested in (a) the nominally weft and (b) the warp directions.

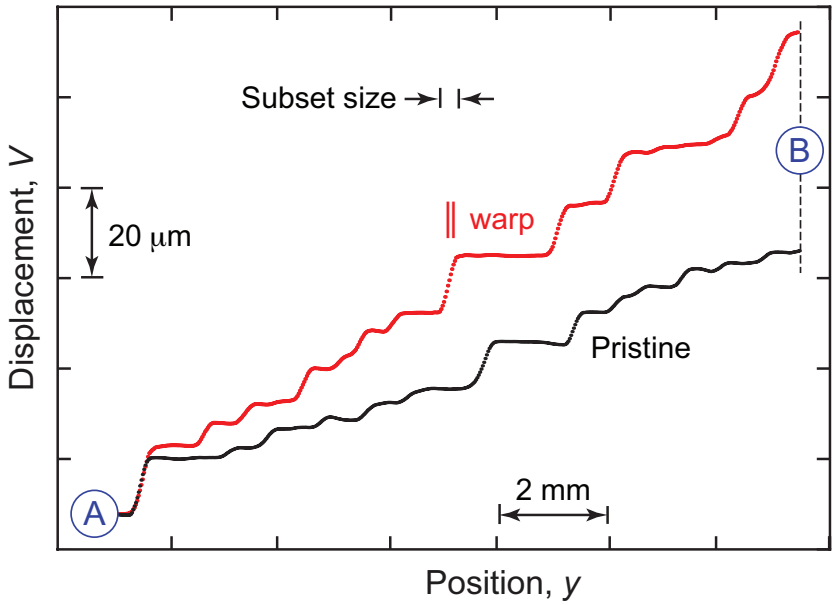

Figure 5.14: Line scans of axial displacement along two nominally-equivalent paths (indicated by dotted lines in Fig. 5.11) in pristine and sheared panel specimens loaded in the warp direction. The displacement jumps are associated with matrix cracks. The finite (apparent) slopes at the jump locations are a consequence of the finite subset size needed to correlate the images via DIC.

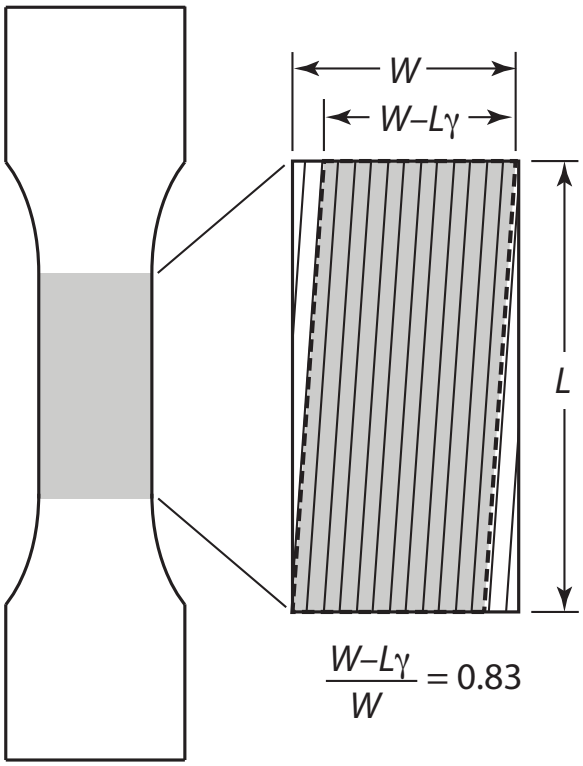

Figure 5.15: Schematic of continuous fibers traversing the composite gage length when the test specimen is oriented for loading perpendicular to the warp direction in the sheared panel.

Chapter 6

Modeling discrete damage in composites

6.1 Introduction

As discussed in Chapter 3, the composite system studied here exhibits periodic matrix cracking with a relatively low crack density ($\sim$1 mm^{-1}). The low crack density means that composite deformation can only be homogenized over relatively long length-scales. For simulations of geometries at or below the unit cell size, cracks should be explicitly modeled.

Two methods for modeling discrete damage are available in commercial codes (such as Abaqus). One method is to mesh cohesive elements between

all continuum elements. This has two limitations: the degrees of freedom of the model are greatly increased, and the crack path is dependent upon the mesh shape (since cracks can only propagate along boundaries of continuum elements). Therefore, the crack paths must be shown to converge with respect to mesh shape and size. The additional degrees of freedom may result in a high computational cost.

The second method is to use the extended finite element method (XFEM). This method is capable of modeling discontinuities within an element. Since the crack path is no longer dependent on the mesh shape and size, this method can make use of a much coarser mesh than one using cohesive elements. However, the number of degrees of freedom is increased relative to an elastic calculation; all nodes in each XFEM element must be duplicated to capture displacements after the onset of cracking (Yang and Liu, 2013).

Two new methods have been developed for modeling discrete damage that reduce the computational cost of the two methods discussed above. The first is based on the discrete element method (DEM) (Pro et al., 2014). It is similar in nature to the first method described above: the model consists of continuum elements (representing the material) with cohesive interactions at all element interfaces (allowing for cracks to propagate between them). Although this also results in a large number of degrees of freedom, the method can readily be par-

allelized to run on graphics processing units (GPUs) (Pro et al., 2014). Thus, computation time is reduced relative to an Abaqus model using cohesive elements.

The second method is the augmented finite element method (AFEM). It is similar to XFEM in that discontinuities can be captured within an element, however, it reduces the total degrees of freedom by modeling the discontinuities with nodes internal to the element (Ling et al., 2009; Yang and Do, 2014; Yang and Liu, 2013). It has been shown that using AFEM can increase computational speed (relative to XFEM) by at least an order of magnitude (Yang and Liu, 2013).

A preliminary assessment of two codes (one using DEM, the other using AFEM) is presented below. The AFEM code is capable of 3D calculations but does not presently include thermal degrees of freedom. It was used to simulate matrix cracking and interface debonding under uniaxial tension. The DEM code is presently limited to 2D calculations, though it includes thermal degrees of freedom. It was used to simulate the onset of matrix cracking during a thermal cooling cycle.

6.2 Simulation of tensile response

An attempt was made to capture the inelastic tensile behavior of the composite using a code developed by Yang and Naderi (*private communication*). The code is a user element that runs within Abaqus. At present it has several limitations: thermal degrees of freedom are not included, arbitrary crack initiation is not enabled (*i.e.*, cracks need to be seeded), and cracks cannot bifurcate. The code also has difficulty accommodating crack turning; if the crack plane passes too close to a node, the resulting small-angle or -volume element can cause numerical instability. In the present simulations crack turning was disabled.

Based on the results of elastic and DEM calculations presented in the next section, as well as experimental observations, cracks are assumed to initiate above tows transverse to the loading direction. In the simulations presented here a crack has been seeded in the matrix above a transverse tow on one surface of the virtual specimen.

6.2.1 Geometry generation and meshing

The model makes use of the voxel mesh presented in Chapter 4. For the purpose of demonstration the size of the model was intentionally reduced;

only a quarter of a unit cell (three weft tows and four quarter-length warp tows) was generated with a 100 µm voxel size. The AFEM code uses tetrahedral elements, so the voxel mesh had to be refined. Each quadrilateral was split into five tetrahedra; adjoining elements still shared faces.

Matrix elements in the plane of the seeded crack were duplicated. One set was defined as AFEM user elements. Abaqus is incapable of rendering user elements, so the duplicated set was used for display purposes.

All element faces at the tow-matrix interface were identified. Nodes on this surface were duplicated and the interface was meshed with cohesive elements. This enabled the model to capture interface debonding.

The final mesh consists of 1.1×10^5 C3D4 continuum elements in the tows and the matrix, 3.6×10^3 user elements in the matrix at the plane of the crack and 1.7×10^4 COH3D6 cohesive interface elements at the tow-matrix boundary. Finite element simulations were conducted in Abaqus Standard (Version 6.11-2).

Displacement boundary conditions were used to simulate the tensile test. All nodes on the bottom face ($y = 0$) of the tensile specimen were constrained from displacing axially ($v = 0$); those on the top face ($y = 25.4$) were incrementally displaced. To prevent rigid body motion of the entire specimen, off-axis degrees of freedom for the central node on the top and bottom faces were con-

strained ($u = w = 0$).

6.2.2 Constitutive laws

The tows were meshed with continuum elements and were assumed to be transversely isotropic. Local coordinate systems were defined to align each element to the tow path. The elements were assigned the elastic constants listed in Table 3.1. The matrix was assumed to be isotropic; its modulus and Poisson's ratio were chosen to be $E_m = 200\,\text{GPa}$ and $\nu = 0.2$, respectively. Matrix continuum elements that were coincident with AFEM user elements were used for display purposes only; they were assigned a modulus of 1 MPa.

The user elements representing the matrix in the plane of the crack were also assumed to be isotropic. Their elastic properties were the same as the continuum elements above. Matrix cohesive strength was chosen to be 50 MPa based on the low expected strength of the porous matrix. The toughness of the matrix was assumed to be the same as that of monolithic silicon carbide ($\sim 50\,\text{J}\,\text{m}^{-2}$ (Henshall et al., 1977)). The tow-matrix interface was assumed to be weaker than the matrix, although the exact interfacial properties are unknown and would depend on the exact path of the crack. Inspection of polished cross-sections of a tensile specimen (shown in Fig. 3.8) indicates that cracks propagate at the fiber/CVI SiC boundary as well as the matrix/CVI

SiC boundary. For the purpose of demonstration, values typical of a boron nitride interface (as used in SiC/SiC composites) were assumed (Morscher et al., 1996). Cohesive elements representing the interface were assigned properties of $\sigma_C = 20\,\text{MPa}$ and $\gamma = 10\,\text{J}\,\text{m}^{-2}$.

6.2.3 Results

A simulated tensile test was run to an applied strain of 1 %. It successfully completed in $\sim$ 10 hours. A representative section of the deformed model along a weft tow is shown in Figure 6.1.

The simulated and experimentally measured global stress-strain curves are plotted in Figure 6.2. The initial elastic modulus and matrix cracking stress are overpredicted. Evidently, the matrix modulus of $E_m = 200\,\text{GPa}$ (predicted from the thermal expansion simulations of Chapter 4) was an overestimate.

After the onset of nonlinearity, the tangent modulus of the simulated stress-strain curve is approximately twice that of the experiment. This is most likely due to the fact that only one crack was modeled in the simulation. In experiments the crack density was found to be $\sim 1\,\text{mm}^{-1}$, resulting in 4 or 5 cracks per unit cell in the weft direction. If more had been included, the matrix would likely have carried less load and the tangent modulus would have been lower.

6.3 Simulation of thermally-induced matrix cracks

Motivated by the matrix cracks found in as-received composite panels, a model was developed to simulate matrix cracking that occurs due to thermal stresses induced by cooling of the panels from processing temperatures. The model makes use of a DEM code developed by Pro et al. (2014). At present, the code is limited to 2D simulations.

The feasibility of approximating the composite as a 2D section was evaluated. This was done by running an elastic calculation on a 3D model of the composite. A virtual specimen of single unit cell with a full matrix was generated using the procedure outlined in Chapter 4. It was meshed with a 50 µm voxel size and imported into Abaqus. The tow elements were assigned local orientations, the elastic constants listed in Table 3.1 and the thermoelastic constants calculated in Chapter 4. The matrix was assigned a modulus of $E_m = 200\,\text{GPa}$ and a thermal expansion coefficient of $\alpha_m = 4.3 \times 10^{-6}\,\text{K}^{-1}$. The model used in-plane periodic boundary conditions. A temperature change of $-1000\,^{\circ}\text{C}$ was applied to all elements.

The calculated in-plane stresses induced by the thermal excursion are shown in Figure 6.3. The virtual specimen is shown from an oblique view; the front face corresponds to a section along a warp or a weft tow and the upper face shows the matrix surface. In the plane of the sections, the tensile

stresses in the matrix are highest directly above tows coming out of plane. This is consistent with the observed locations of cracks in polished sections of the composite (Fig. 2.3). Furthermore, the magnitude of the tensile stresses is $> 200\,\text{MPa}$: likely high enough to initiate cracking in a porous SiC matrix.

The stress distribution on the specimen surface is periodic. In the section along the warp orientation there is little change in the stress distribution in the out-of-plane direction; stress concentrations appear to persist across the sample. In the weft orientation a similar effect is observed, though the stress concentrations do not persist as far in the out-of-plane direction. The persistence of the stress distributions suggests that, for the warp orientation at least, the composite response may be approximated with a 2D section. A 2D model should result in stress concentrations at similar locations to those calculated in the 3D model.

6.3.1 Geometry and meshing

The virtual geometry generator (Blacklock et al., 2013) was used to generate a single unit cell of the composite with a grid spacing of 50 µm. Meshes were created from the virtual geometry in two ways.

In the first, used in the damage simulations presented below, a voxel mesh was created from the geometry with a voxel size of 50 µm. The quadrilaterals

were divided into tetrahedra as described above. All nodes on a select plane through a warp tow were extracted to form a 2D mesh of triangles. As with the other voxel-based meshes, this mesh results in a stepped interface between the tows and the matrix. The mesh contains 2.8×10^4 elements.

An alternative method of meshing has been developed which results in a smooth interface between the tows and the matrix. This method was used in the elastic calculations presented below. A 2D section along a warp tow was selected from the virtual geometry, prior to meshing. Neighboring points within a given tow section were connected to form a planar straight line graph. A bounding box was then defined to represent the full region occupied by the tows and the matrix (Fig. 6.4(a)).

In order to prevent numerical problems in meshing and simulation, small angle regions of the geometry were eliminated in the following way. For all values of x in the grid of points in the planar straight line graph, pairs of points were identified that were separated in y by less than 14 µm. Given a grid spacing of 50 µm, this guaranteed that there were no angles smaller than $\theta = \arcsin(14/50) = 16^\circ$.

The resulting planar straight line graph was meshed with the publicly available code *Triangle* (Shewchuk, 1996). The meshing algorithm is based on Delaunay triangulation and allows for user control of allowable element vol-

umes and angles. Several meshing algorithms can be used which will, for a given number of elements, generate different mesh shapes. Mesh shape convergence can be established in this manner. The code also identifies all elements lying within a given region, which aids in assignment of material properties. An example mesh is shown in Figure 6.4, where elements have been colored by material region.

Following a successful convergence study, the final mesh consisted of 3×10^4 elements.

6.3.2 Constitutive laws

The DEM code takes as input elastic constants describing all elements and a traction-separation law (defined by stiffness k, cohesive strength σ_C and toughness γ) for all interfaces between elements. Element properties are assigned by material region; interface properties are assigned between pairs of regions (*i.e.*, tow-matrix, tow-tow, and matrix-matrix). The elastic and thermoelastic constants of the matrix are the same as those used in the 3D elastic model ($E_m = 200\,\text{GPa}$; $\nu = 0.2$; $\alpha_m = 4.3 \times 10^{-6}\,\text{K}^{-1}$). Elements in the tows were assigned local orientations aligned with the tow axis; the out-of-plane tows were assumed to be aligned with the out-of-plane axis. They were assigned the same elastic and thermoelastic properties as the tow elements in the 3D

elastic model.

The cohesive stiffness k was chosen to be the same for all interfaces ($4 \times 10^9\,\mathrm{GPa\,m^{-1}}$). The value was chosen based on comparisons of total strain energy with a quasistatic Abaqus calculation for the same mesh (presented below). Cracking was prohibited in the tows by assigning them infinite strength and toughness. Cohesive properties for the tow-matrix and warp-weft tow interfaces were varied to determine their influence on crack initiation and propagation. The cohesive properties of the matrix were assumed to be $\sigma_C = 50\,\mathrm{MPa}$ and $\gamma = 50\,\mathrm{J\,m^{-2}}$ (as in the AFEM simulation).

6.3.3 Time stepping and loading rate

DEM is an explicit calculation, and is therefore time step-dependent. The time step must be small enough to resolve the propagation of an elastic wave across a single element. The elastic wave speed is given by $\sqrt{E/\rho}$, where E is the material Young's modulus and ρ is the density. For the present composite ($E_m = 200\,\mathrm{GPa}$; $\rho = 3000\,\mathrm{kg/m^3}$) the elastic wave speed is $8.2\,\mathrm{km\,s^{-1}}$. The average element size is $\sim$50 µm, so the upper limit on the time step is 6.1×10^{-9} s. A value of 1×10^{-10} s was used for all simulations.

The loading rate must be chosen to be quasi-static. This is accomplished by calculating the ratio of dynamic strain energy to total strain energy to estab-

lish insensitivity to loading rate (*i.e.*, a ratio of $< 1\,\%$ at fracture). Convergence was obtained in elastic simulations with a loading rate of $1 \times 10^7\,^{\circ}\mathrm{C\,s^{-1}}$. The loading rate can be accelerated through the use of proportional damping, although this has not been incorporated in the present simulations. Load rate insensitivity has not yet been established for the damage simulations; for the purpose of demonstration of the technique, the damage simulations presented here were run using the same loading rate as the elastic simulations.

6.3.4 Results

Elastic simulation

Elastic simulations of a 1000 °C cooling cycle were run to validate the DEM model with Abaqus. Identical meshes were used in DEM and quasi-static Abaqus simulations. Excellent agreement between the two was obtained when a cohesive stiffness of $k = 4 \times 10^9\,\mathrm{GPa\,m^{-1}}$ was used in the DEM simulations (Fig. 6.5).

The elastic simulations also indicate that stress concentrations are expected in approximately the same locations in the 2D simulations as in the 3D simulations. The exception is the region of matrix above a surface weft tow mid-way between two warp crowns. In this region, the 2D simulations predict lower stresses than the 3D simulations.

Damage simulation

Simulations were run to evaluate the influence of interfacial strength and toughness on the evolution of matrix cracks during a 1000 °C cooling cycle (as above). Three combinations were considered. In the first, the cohesive strength between the tows and the matrix and between the warp and the weft tows was selected to be $\sigma_C = 20\,\mathrm{MPa}$; the interfacial toughness was selected to be $\gamma = 10\,\mathrm{J\,m^{-2}}$. These conditions were chosen to represent a relatively weak interface, as might be expected if cracks propagate along the boundary between the fibers and CVI SiC within the tow. The second combination was designed to model an intermediate interfacial strength and toughness, representative of cracks propagating along the boundary between the CVI SiC and the slurry- and PIP-derived SiC matrices. In this case the same values were used for the interfaces as were used for the matrix ($\sigma_C = 50\,\mathrm{MPa}$ and $\gamma = 50\,\mathrm{J\,m^{-2}}$). The third set of parameters was chosen to only allow the matrix to crack; the material interfaces were assigned infinite strength and toughness. This is consistent with the observed cracks in the as-received material (Fig. 2.3).

Calculated in-plane stresses for the three simulations are shown in Figure 6.6. Displacements have been amplified by a factor of 10 so that cracks are readily visible. The influence of interfacial properties is clear. With a weak interface, debond cracks develop between the warp tow and the matrix; the

matrix itself remains intact. At intermediate interfacial strength both debond cracks and matrix cracks appear. The matrix cracks correspond to regions of high tensile stress predicted by the elastic calculations. When interfacial debonding is prohibited, matrix cracks develop in the same locations as the intermediate case.

The matrix crack density that develops in the intermediate and high interfacial strength simulations is lower than that observed in polished cross-sections (1–2 versus 4–5 per unit cell). The difference in crack densities is attributable to the fact that the simulations only predict cracking in the matrix adjacent to warp crowns, whereas it is also observed to occur in the matrix adjacent to weft tows in polished cross-sections. An improper choice of matrix cohesive properties may have prevented cracks from initiating in the matrix adjacent to weft tows. Another possibility is that these cracks initiate over a warp crown that is out of the plane of the section and then propagate along the weft tow; it would not be possible to capture this with a 2D model.

A comparison of the calculated crack patterns of Figure 6.6 and those observed in the polished cross-sections (Fig. 2.3) suggests that the matrix and tows are very well bonded. Few debond cracks are observed in polished sections of the composite, though they are predicted in the two simulations with finite interfacial strength and toughness. However, there are two reasons to be-

lieve that the debond cracks may be favored in the simulations. The first is that only a single unit cell is modeled without periodic boundary conditions; edge cracks initiating at the weakest interface may have dominated the response. The second reason is the use of a 2D model. This means that the matrix-tow interface is a through-thickness flaw. Debonding along the interface would therefore be more favorable than if the full 3D geometry were modeled.

6.4 Conclusions

Two methods have been evaluated for modeling discrete cracking in CMCs.

Using AFEM, a model incorporating a single matrix crack and tow-matrix debonding broadly captured the global response of the physical specimen. Further refinement of material properties and seeding of additional cracks is required to improve the accuracy of the model.

Additionally, only a quarter of a unit cell was modeled. Scaling up the model to a full unit cell will greatly increase the computational cost of the simulations. A new meshing technique is required to take full advantage of the code's ability to handle arbitrary cracking. The voxel mesh is an inefficient way to mesh the matrix; coarsening the mesh results in a significant loss of

geometric accuracy. Ideally an unstructured tetrahedral mesh should be used, though that poses difficulty in meshing interfaces between materials.

A second model based on DEM has been used to illustrate the influence of tow-matrix interface properties on the evolution of matrix damage. Further development of the code is ongoing to incorporate proportional damping and establish load rate insensitivity in the damage model. The model shows promise in studying the effects of material properties on thermally-induced matrix cracks. Additionally, since the weave geometry can be modeled with smooth interfaces, it is possible to study the effects of geometrical defects on matrix cracking.

Application of the DEM model to tensile loading is technically feasible, but may not be accurate. Due to the geometry of the weave, a 3D model may be required to incorporate the constraint provided by tows out of the plane of the 2D simulation.

Extension of the DEM model to 3D, and incorporation of thermal degrees of freedom and crack bifurcation in the AFEM model, would offer the ability to fully capture composite response. A representative virtual specimen could be first cooled from processing temperatures to initiate matrix cracks due to thermal stresses. The same specimen could then be loaded in tension to predict the extension of matrix cracks under applied load. This would be a powerful

tool for studying the influence of material properties and weave geometry on the response of a composite.

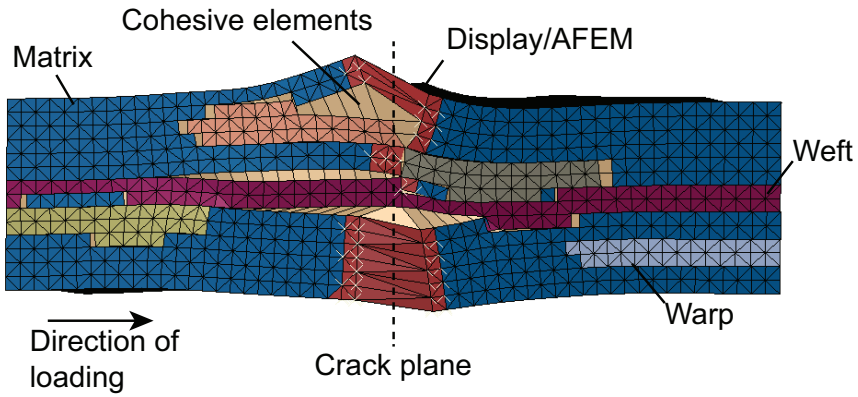

Figure 6.1: Section along a weft tow of the AFEM simulation at 1 % applied tensile strain. Displacements have been scaled by a factor of 20.

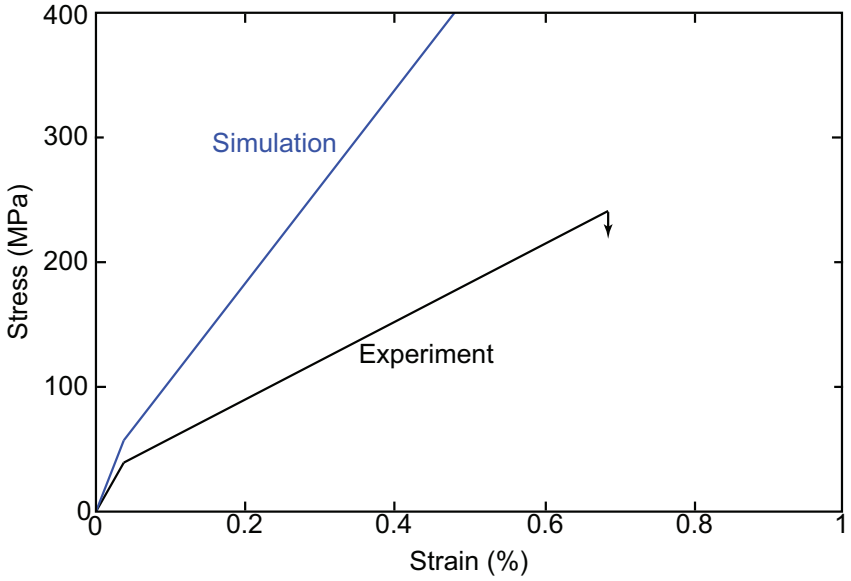

Figure 6.2: Global stress-strain response measured on the fully-processed large unit cell composite and calculated from the AFEM simulation.

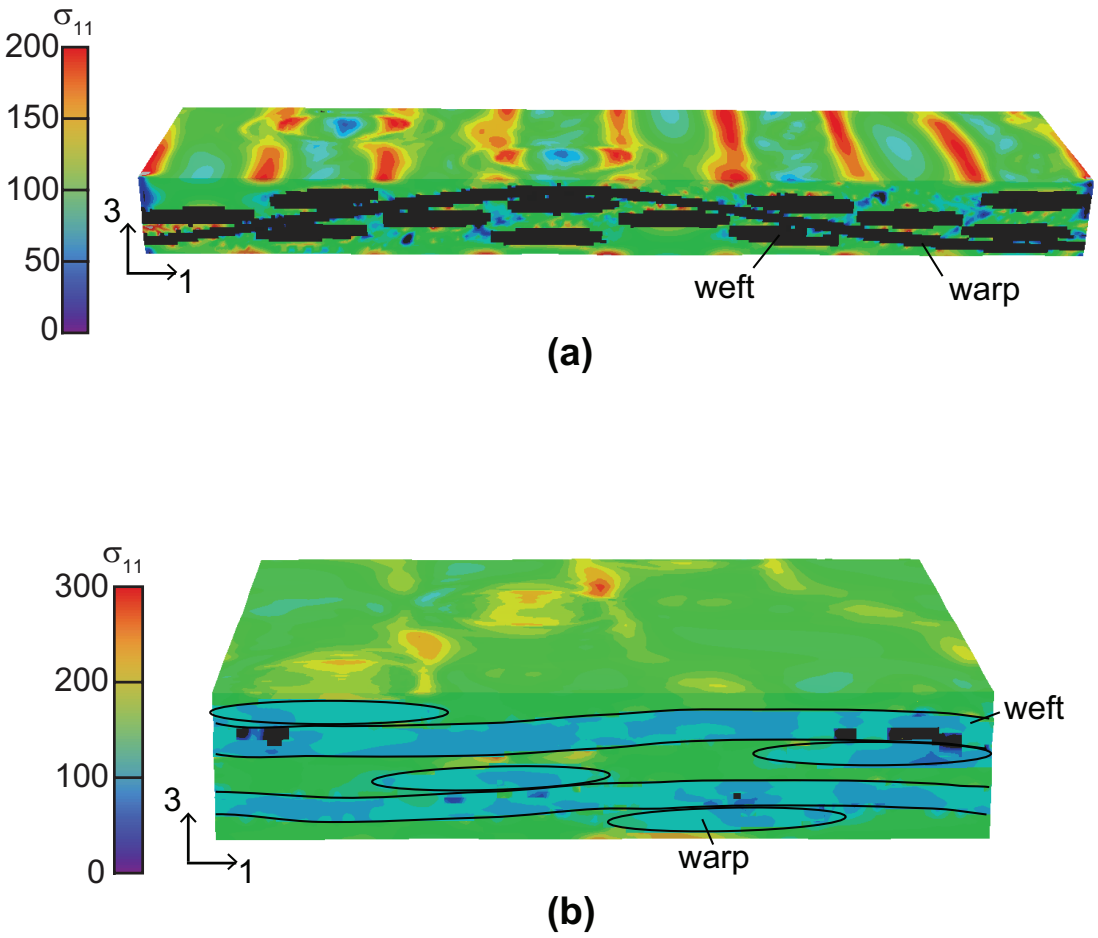

Figure 6.3: Development of in-plane stresses in a 3D elastic model (calculated with ABAQUS) following a 1000 °C cooldown cycle. The model has been sectioned along the (a) warp direction and (b) weft direction. The black shading in the warp section indicates that the tows are in compression. Contour plots are oblique view; the front face is a section along a tow population and the top face is the specimen surface.

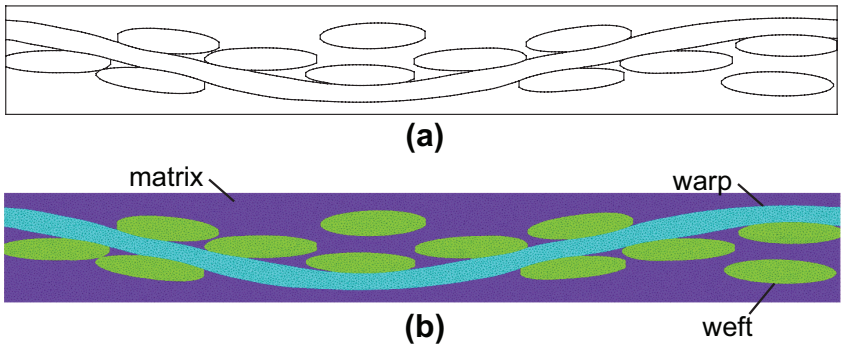

Figure 6.4: (a) Planar straight line graph and (b) mesh of virtual section along warp tow.

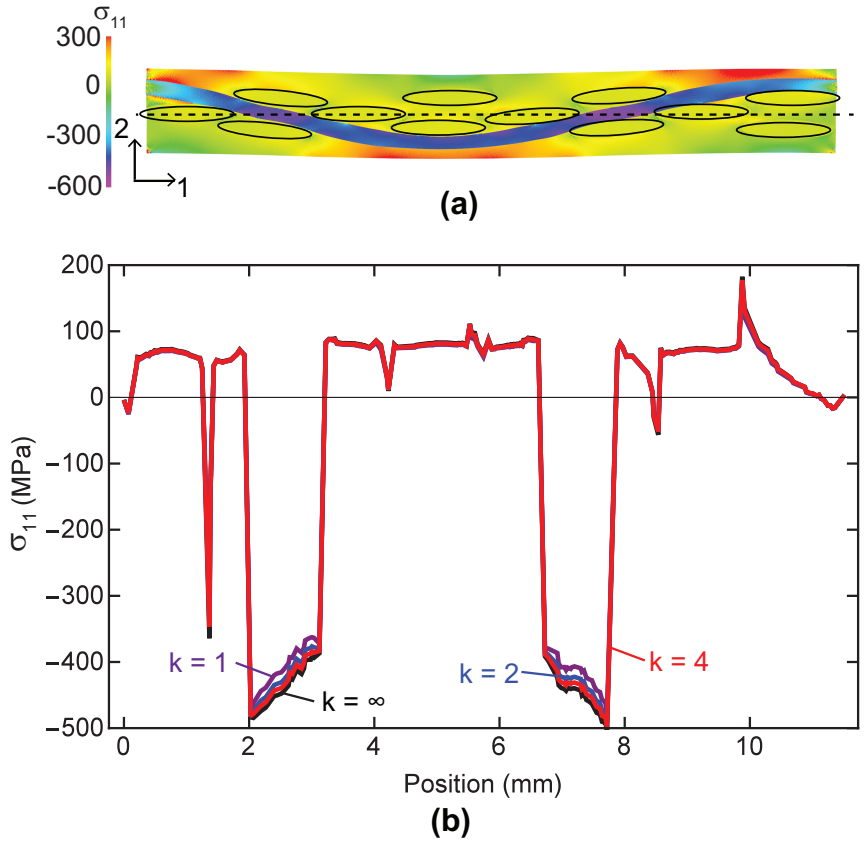

Figure 6.5: (a) Contour plot of in-plane stresses for an elastic 2D model of a 1000 °C cooling cycle. Ovals indicate location of out-of-plane weft tows. Dashed line indicates location of (b) a line scan of axial stress comparing elastic simulations with infinite cohesive stiffness (calculated with ABAQUS) to those of DEM with a range of values for cohesive stiffness. The units of k are 1×10^9 GPa m^{-1}.

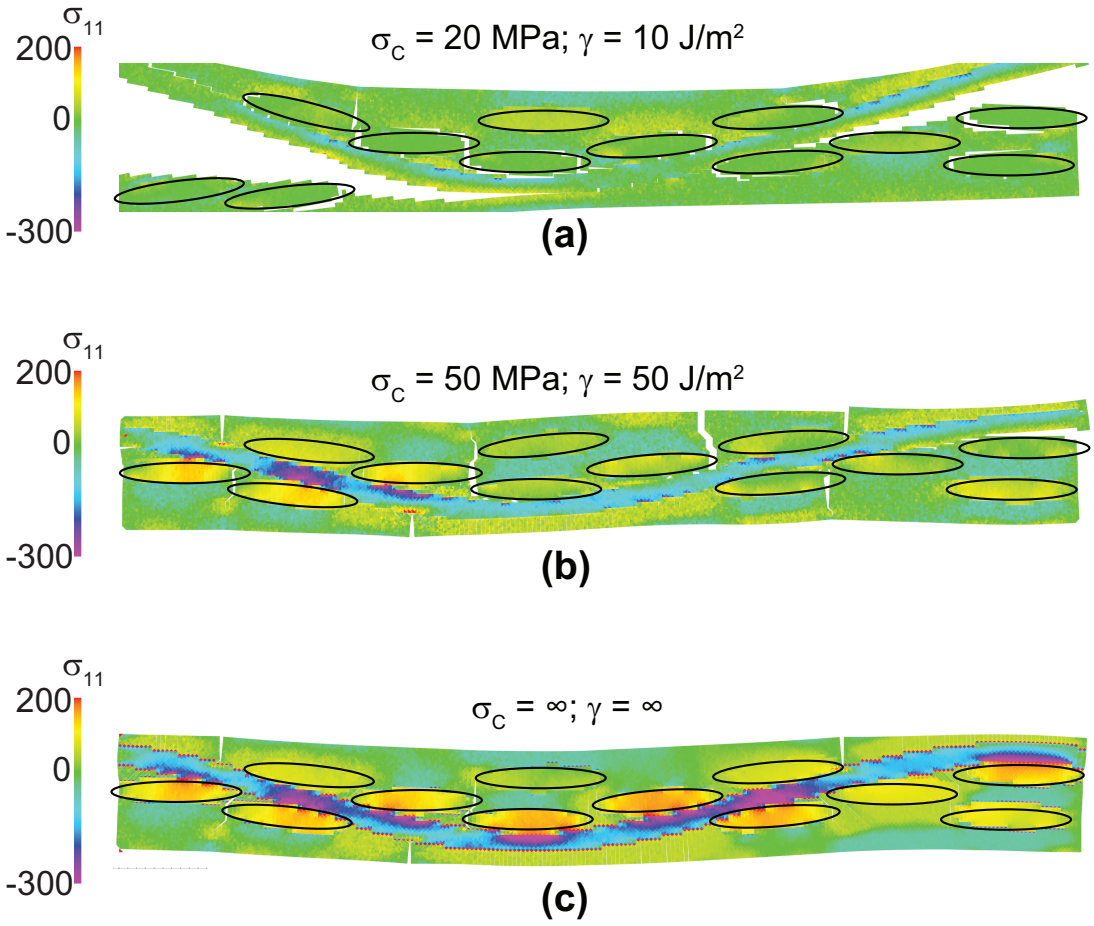

Figure 6.6: Contour plots of in-plane stress for DEM damage simulations of a 1000 °C cooling cycle using the indicated values of tow-matrix interface strength, σ_C, and toughness, γ. Locations of weft tows are indicated with ovals.

Chapter 7

Conclusions

In this study, an assessment of the architecture-dependence of composite mechanical response was performed using a combination of experimental and computational tools. The work was focused on a prototypical C/SiC composite produced with two different fabric preforms and two different types of matrix. A geometrically-accurate virtual model of the composite was developed to probe architecture effects. Full-field strain measurements were used to characterize both the global and the local stress-strain response of the composites. By combining the experimental measurements with micromechanical models and virtual tests, the elastic and thermoelastic properties of the tows were ascertained. Once calibrated, virtual tests were used to study the architecture-dependence of mechanical response and of matrix cracking in tex-

tile composites.

The effects of textile architecture can broadly be grouped by the four length-scales at which they are observed: the panel, the coupon, the tow, and the sub-tow.

At the scale of the *panel*, Rossol et al. (2014) observed that the packing density of tow populations can vary on the order of a few percent due to defects introduced during the weaving process. Defects can also be introduced during handling, resulting in relative rotation of the two tow populations by 1–2°. Generally the magnitude of these effects is small, and they are therefore not detectable at the scale of the coupon (at which mechanical tests are performed). This was the case for shear defects intentionally introduced to a panel (presented in Chapter 5); when tow populations were rotated relative to each other by $\sim 4.5°$, the mechanical response along the direction of the tow axis was essentially unaffected relative to pristine material. However, when the relative rotation of tows resulted in misalignment of fibers to the loading direction, both the tensile strength and the post-cracking tangent modulus were reduced. These effects are attributable to a reduction in the number of fibers spanning the gage section. After the global onset of nonlinearity, fibers that do not span the gage section evidently carry minimal load; thus, the strength and the modulus are reduced.

At the scale of the *coupon*, architecture effects are related to the paths of tows (*i.e.*, tow waviness) and to the extent of matrix processing. In composites with little matrix filling the space between tows, such as the partially-processed composite studied here, the tows may be considered to be sinusoidal beams in the elastic regime. As such, when they are nearly straight (as when the present composite was loaded in the weft direction) their mechanical response is dominated by the homogenized properties of the tows and matrix. In contrast, when there is substantial out-of-plane variation in the paths of the tows (as when the present composite was loaded in the warp direction), the stiffness of the composite is reduced relative to the volume fraction-weighted contributions of the fibers and the matrix; qualitatively, this would be expected from the axial extension of a curved beam. In the present composite, a rudimentary model based on beam theory under-predicted stiffness. This was presumably because the constraint provided by the transverse tows on the motion of the axial tows was not included. A more detailed 3D virtual model of the composite that included the transverse tows captured the composite stiffness in the warp orientation well. In the inelastic regime of composites without matrix between the tows, tow waviness can result in large strains to failure. In the present composite, after the limited matrix surrounding the tows undergoes cracking, the tows may straighten with relatively little constraint on their motion.

When matrix is present between the tows, the extensional phenomena observed in the elastic and inelastic response of wavy tows are heavily constrained. In the elastic regime, architecture dependence of mechanical response may still arise from tow anisotropy; that is, if the stiffness of the tow is lower when loaded off-axis, then the coupon stiffness will be reduced with wavy tows. In the inelastic regime of the present composite, regardless of tow waviness, the terminal tangent modulus is the same as the elastic modulus of the composite in the partially-processed state. Evidently, after the onset of matrix cracking, the composite is once again dominated by the tow response. However, increasing tow waviness was observed to decrease failure strain. This is likely due to bending stresses that develop in the constrained, curved tows.

More broadly, the effects of tow waviness on composite failure follow a general trend. Consistent with previous observations of architecture effects on composite failure by Berbon et al. (2002), increasing tow waviness was observed to decrease strength. As mentioned above, this is most likely due to bending stresses that develop in curved tows due to constraint of either the matrix (if fully-processed) or the transverse tows (if partially-processed). Increasing tow waviness is also found to decrease strain to failure when the tows are highly constrained and to increase strain to failure when they are not (as in the partially processed composite studied here and in those studied by Berbon

et al. (2002)).

As with effects at the panel scale, architecture effects at the scale of the *tow* typically do not influence mechanical response at the scale of the coupon. Two examples of tow-scale architecture effects were studied in the present work. One of these was distortions to the weave. Graphite rods were inserted through a fabric preform to create holes without damaging the fibers; the resulting distortions to the fabric were large but highly localized (over a distance of $< 1\,\text{mm}$). On a net-section basis, the effects of these distortions on specimen strength were negligible compared to pristine specimens. Any effects of the distortions on strains and cracking were smaller than the natural variation observed in the pristine composite. This coupon-scale insensitivity to fabric distortions is encouraging.

The second example of tow-scale architecture effects manifests in local strains measured on the tow surface. When the partially-processed composite studied here was loaded in tension, average strains on the surface of individual visible tow segments were typically lower than the macroscopic strain. This was a result of tow waviness; the observed surface was always convex, meaning that the local strain was reduced relative to the macroscopic strain due to a negative bending strain component. Natural variation in tow shape (as observed by Bale et al. (2012)) also results in heterogeneity of surface strains;

this was observed in the thermoelastic response of the present composite. The interaction between neighboring tows is an important variable in these local effects (as shown with simulations of composite tensile and thermal response).

Finally, at the *sub-tow* scale, architecture effects are manifest primarily in the location of matrix cracks. Matrix cracking in C/SiC composites is essentially unavoidable; this is due to the thermal expansion mismatch between the fibers and the matrix and the high processing temperatures required to deposit a SiC matrix. For instance, in the CVI process, the SiC matrix is formed at $\sim 1500\,^{\circ}\mathrm{C}$. Upon cooling from this temperature, the mismatch strains are on the order of 0.006. Assuming the SiC is fully dense, the resulting tensile stress in the matrix would be 2.4 GPa: sufficient to initiate cracks. The processing temperatures are lower in the PIP process ($\sim 1000\,^{\circ}\mathrm{C}$) and the resulting SiC matrix is more compliant ($\sim 200\,\mathrm{GPa}$). Nevertheless, the expected tensile stresses due to thermal expansion mismatch (800 MPa) would still be high enough to initiate cracks.

While the matrix cracks are not unexpected, the locations at which they occur are correlated with the underlying textile architecture. A virtual test of the $1000\,^{\circ}\mathrm{C}$ cooling cycle from PIP processing temperatures, calibrated with the measured thermoelastic response of the tows, showed that peak tensile stresses within the matrix occur at the locations at which cracks are found in

polished cross-sections of the PIP-processed material. The simulation was in agreement with the expectation that tensile stresses are of sufficient magnitude to initiate cracks.

The sub-tow architecture effects (*i.e.*, matrix cracks) ultimately tie into the coupon-level mechanical response. In the composites studied here, the cracked PIP-derived SiC matrix initially responds elastically in both loading directions. However, at relatively low global strains ($\sim$ 0.05 %), the pre-existing matrix cracks appear to extend and bifurcate. This gives rise to the global onset of nonlinearity.

Future work should focus on furthering understanding of the matrix cracking process. This can be achieved through the development of models of discrete damage. Two potential methods for doing so were evaluated in Chapter 6. Thermal cooling from processing temperatures was simulated using a model based on the discrete element method. Interface properties between the tows and the matrix were found to have a strong influence on the progression of matrix cracking. A second model, based on AFEM, was developed to capture the tensile response of the composite by incorporating both matrix cracks and interface debonding. The model broadly captures the global stress-strain response of the composite.

Both models show potential for predicting the influence of material prop-

erties and geometric defects on the onset of matrix cracking. However, further development of geometrically accurate 3D models remains a challenge using either AFEM or DEM due to the difficulty in meshing smooth interfaces. The potential benefits of solving this problem are large. Such models would capture the full evolution of matrix cracks, from crack initiation during processing to extension and bifurcation under applied load.

Appendix A

Tow elastic constants

The elastic properties of the C/SiC tows are obtained in the following way. The SiC and the intra-tow porosity are homogenized into an effective medium and the properties of this medium are inferred from experimental measurements and FE simulations of tensile properties in both warp and weft orientations. The calibration procedure is performed in three steps: (i) the tow properties are calculated using established composite models, the reported fiber properties (Table A.1) and a set of assumed elastic properties of the effective medium; (ii) FE calculations are performed of the elastic response of the composite in both orientations using the calculated tow properties; and (iii) the FE results are compared with the experimental measurements. The procedure is repeated until consistency is obtained between the computed and measured

composite moduli.

The tows are treated as being transversely isotropic. Denoting x as the fiber direction and y and z as the two orthogonal directions, the pertinent elastic constants are the Youngs moduli, E_x and E_y, the shear moduli, G_{xy} and G_{yz}, the bulk modulus, k, and the Poisson's ratios, ν_{xy} and ν_{yz}. Among these, five are necessary for a complete description of the tow response. The constants are calculated from Hashin's equations for composites reinforced with unidirectionally aligned anisotropic fibers (Hashin, 1979).

Closed-form solutions for the elastic constants E_x, G_{xy}, ν_{xy} and k for composites with transversely isotropic fibers are based on modifications to the solutions from the composite cylinder assemblage model for isotropic constituents (Hashin, 1979; Hashin and Rosen, 1964). They are given by:

$$E_x = E_{f\parallel} f + E_m(1-f) + \frac{4(\nu_{f\parallel} - \nu_m)^2 f(1-f)}{\frac{(1-f)}{k_{f\perp}} + \frac{f}{k_m} + \frac{1}{G_m}} \tag{A.1}$$

$$\nu_{xy} = \nu_{f\parallel} f + \nu_m(1-f) + \frac{(\nu_{f\parallel} - \nu_m)(\frac{1}{k_m} + \frac{1}{k_{f\perp}}) f(1-f)}{\frac{(1-f)}{k_{f\perp}} + \frac{f}{k_m} + \frac{1}{G_m}} \tag{A.2}$$

$$G_{xy} = G_m + \frac{f}{\frac{1}{G_{f\parallel} - G_m} + \frac{1-f}{2G_m}} \tag{A.3}$$

$$k = k_m + \frac{f}{\frac{1}{k_{f\perp} - k_m} + \frac{1-f}{k_m + G_m}} \tag{A.4}$$

where the subscripts $\parallel$ and $\perp$ denote axial and transverse directions, respectively, f is the fiber volume fraction and the subscript m denotes the effective medium.

Although closed-form solutions for the remaining parameters—G_{yz}, E_y and ν_{yz}—do not exist, the available bounds are close to one another and provide a useful basis for estimation. Here, we employ average values of the upper and lower bounds. Provided $G_{f\perp} < G_m$ and $k_f < k_m$ (as in the system of present interest), the bounds for the transverse shear modulus, $G_{yz(\pm)}$ are given by:

$$G_{yz(-)} = G_m \left[1 + \frac{(1+\beta_1)f}{\rho - f\left(1 + \frac{3\beta_1^2(1-f)^2}{\alpha f^3 - \beta_1}\right)} \right] \tag{A.5}$$

$$G_{yz(+)} = G_m + \frac{f}{\frac{1}{G_{f\perp}-G_m} + \frac{k_m+2G_m}{2G_m(k_m+G_m)}(1-f)} \tag{A.6}$$

where $\pm$ represents the upper or lower bound and $\alpha = \frac{\beta_1 - \gamma\beta_2}{1+\gamma\beta_2}$; $\rho = \frac{\gamma+\beta_1}{\gamma-1}$; $\beta_1 = \frac{k_m}{k_m+2G_m}$; $\beta_2 = \frac{k_f}{k_f+2G_{f\perp}}$; $\gamma = \frac{G_{f\perp}}{G_m}$. The bounds for E_y and ν_{yz} are:

$$E_{y(\pm)} = \frac{4kG_{yz(\pm)}}{k + mG_{yz(\pm)}} \tag{A.7}$$

$$\nu_{y(\pm)} = \frac{k - mG_{yz(\mp)}}{k + mG_{yz(\mp)}} \tag{A.8}$$

where $m = 1 + \frac{4k\nu_{xy}}{E_x}$.

The Poissons ratio of the effective medium is taken to be $\nu_m = 0.2$ and its Youngs modulus E_m is varied over a wide range. For each selected value of E_m, the effective tow properties are computed from Eqs. (A.1)–(A.8) and used as inputs to the finite element calculations.

Comparisons of the experimental measurements and the numerical results are plotted in Fig. A.1. Focusing on the very small strain regime, the comparisons indicate that the best estimate of the effective medium modulus is

$E_m \approx 100\,\text{GPa}$ (it should be noted, however, that the composite modulus is only weakly dependent on this selection and thus the inferred estimate is subject to considerable uncertainty). The resulting average tow properties are summarized in Table 3.1.

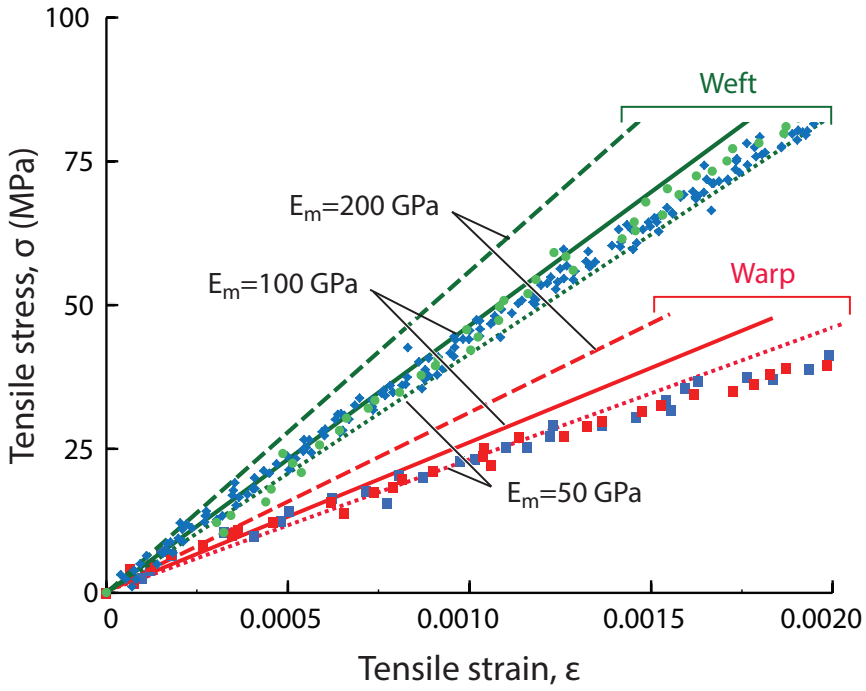

Figure A.1: Calibration of effective medium Young's modulus for warp and weft loading. The solid symbols are experimental data points and the lines are results of finite element calculations. Only the small strain parts of the full stress-strain curves are shown.

Table A.1: Elastic Properties of T300-Carbon Fibers

Young's modulus[1]		Shear modulus[1]		Bulk modulus[2]	Poisson's ratio[3]		Volume fraction[4]
$E_{f\parallel}$	$E_{f\perp}$	$G_{f\parallel}$	$G_{f\perp}$	$k_{f\perp}$	$\nu_{f\parallel}$	$\nu_{f\perp}$	f
230 GPa	14.5 GPa	22.75 GPa	4.8 GPa	15 GPa	0.27	0.51	0.61

[1] BP-Amoco chemicals.

[2] $E_{f\perp} = \frac{4k_{f\perp}G_{f\perp}}{k_{f\perp}+mG_{f\perp}}$, $m = 1 + \frac{4k_{f\perp}\nu_{f\parallel}^2}{E_{f\parallel}}$.

[3] $\nu_{f\perp} = (E_{f\perp}/2G_{f\perp}) - 1$

[4] Determined from filament count and fiber density reported by the manufacturer in combination with the tow cross-sectional area measured by computed tomography (Bale et al., 2012)

Appendix B

Laminate representation of a woven composite

The elastic properties of the woven composite are expected to follow (to first order) the predictions of laminate theory (Cox and Flanagan, 1997). As noted in Chapter 3, the composite is treated as an unbalanced symmetric laminate with two ply populations representing the regions containing warp and weft tows, each with the same fiber volume fraction. The ratio of ply thicknesses is then selected to be equal to the ratio of fiber volume fractions in the weft and warp direction. This ratio is 2 and 1.36 in the small and the large unit cell composites, respectively.

The engineering elastic constants of the plies are computed using the same

micromechanical model described in Appendix A. This model provides all of the necessary engineering elastic constants of a unidirectionally-reinforced ply. The total volume fraction of fibers in the composite (33 % and 26 %) is substituted for the volume fraction of fibers within the tow. As with the partially-densified composite, the effective medium properties must be calibrated to the measured elastic response. With the elastic constants describing the ply on hand, the corresponding reduced compliance matrix for a unidirectional ply is given by:

$$\boldsymbol{S}_0 = \begin{bmatrix} 1/E_1 & -\nu_{21}/E_2 & 0 \\ -\nu_{12}/E_1 & 1/E_2 & 0 \\ 0 & 0 & 1/G_{12} \end{bmatrix} \tag{B.1}$$

The compliance matrix can be transformed into an alternative coordinate system, rotated by an angle θ with respect to the original system, via:

$$\boldsymbol{S}(\theta) = [\boldsymbol{A}(\theta)]^{-1}\boldsymbol{S}_0\boldsymbol{A}(\theta) \tag{B.2}$$

where

$$\boldsymbol{A}(\theta) = \begin{bmatrix} \cos^2\theta & \sin^2\theta & 2\cos\theta\sin\theta \\ \sin^2\theta & \cos^2\theta & -2\cos\theta\sin\theta \\ -\cos\theta\sin\theta & \cos\theta\sin\theta & \cos^2\theta - \sin^2\theta \end{bmatrix} \tag{B.3}$$

Finally, the compliance matrix S^C of the *laminate* is expressed as

$$\boldsymbol{S}^C(\theta_{weft}, \theta_{warp}) = \left(\phi\left[\boldsymbol{S}(\theta_{weft})\right]^{-1} + (1-\phi)\left[\boldsymbol{S}(\theta_{warp})\right]^{-1}\right)^{-1} \tag{B.4}$$

where

$$\phi = f_{weft}/(f_{weft} + f_{warp}) \tag{B.5}$$

and θ_{warp} and θ_{weft} denote the angles that the warp and weft tows make with the loading direction.

Appendix C

Micromechanical model for thermoelastic tow properties

The thermoelastic properties of the tows are estimated from micromechanical models using the coefficients of thermal expansion of the constituents, found in Table C.1, and the tow mechanical properties calculated in Appendix A. The thermal expansion coefficient of the effective medium is assumed to be the same as that of CVI SiC. A comprehensive presentation can be found elsewhere (Hashin, 1979; Levin, 1967). For composites with transversely isotropic fibers, the axial and transverse coefficients of thermal expansion, α_x and α_y, are given by:

$$\alpha_x = \bar{\alpha}_{\parallel} + (\alpha_{kl}^f - \alpha_{kl}^m) P_{klrs} (S_{rs11}^c - \bar{S}_{rs11}) \tag{C.1}$$

$$\alpha_y = \bar{\alpha}_\perp + (\alpha^f_{kl} - \alpha^m_{kl}) P_{klrs} (S^c_{rs22} - \bar{S}_{rs22}) \tag{C.2}$$

where S denotes the elastic compliance tensor (computed using the results in Appendix A) and the superscripts f, m, and c refer to fiber, effective medium and composite, respectively. The overbar denotes phase average, notably:

$$\bar{\alpha}_\parallel = \alpha^f_\parallel f + \alpha^m_\parallel (1 - f) \tag{C.3}$$

$$\bar{\alpha}_\perp = \alpha^f_\perp f + \alpha^m_\perp (1 - f) \tag{C.4}$$

$$\bar{S}_{rsij} = S^f_{rsij} f + S^m_{rsij} (1 - f) \tag{C.5}$$

and the tensor P is the inverse of the difference between fiber and effective medium compliance tensors:

$$P_{klrs} \left(S^f_{rsij} - S^m_{rsij} \right) = I_{klij} \tag{C.6}$$

where I is the identity tensor (Hashin, 1979).

Table C.1: Thermal Expansion Coefficients of Composite Constituents

α_m[1]	$\alpha_{f\parallel}$[2]	$\alpha_{f\perp}$[2]
$4.3 \times 10^{-6}\,\mathrm{K}^{-1}$	$-0.6 \times 10^{-6}\,\mathrm{K}^{-1}$	$9 \times 10^{-6}\,\mathrm{K}^{-1}$

[1] Lara-Curzio et al. (1993)

[2] BP-Amoco chemicals (near ambient temperature).

References

ASTM Standard C1275. Standard test method for monotonic tensile behavior of continuous fiber-reinforced advanced ceramics with solid rectangular cross-section test specimens at ambient temperature, 2005. URL www.astm.org. 3.2.2

P. Badel, E. Vidal-Sallé, and P. Boisse. Computational determination of in-plane shear mechanical behaviour of textile composite reinforcements. *Computational Materials Science*, 40(4):439–448, 2007. 1.3

H. A. Bale, M. Blacklock, M. R. Begley, D. B. Marshall, B. N. Cox, and R. O. Ritchie. Characterizing three-dimensional textile ceramic composites using synchrotron X-ray micro-computed-tomography. *Journal of the American Ceramic Society*, 95(1):392–402, 2012. 1.4, 2.2.1, 2.2.2, 2.3.1, 2.3.2, 2.6, 2.7, 3.3.1, 3.3.2, 4.3.1, 7, 4

M. Z. Berbon, K. L. Rugg, M. S. Dadkhah, and D. B. Marshall. Effect of weave architecture on tensile properties and local strain heterogeneity in thin-sheet

C-SiC composites. *Journal of the American Ceramic Society*, 85(8):2039–2048, 2002. 1.2, 1.3, 2.2.1, 3.1, 7

M. Blacklock, H. A. Bale, M. R. Begley, and B. N. Cox. Generating virtual textile composite specimens using statistical data from micro-computed tomography: 1D tow representations for the Binary Model. *Journal of the Mechanics and Physics of Solids*, 60(3):451–470, 2012. 1.4, 2.3.2

M. Blacklock, R. G. Rinaldi, and B. N. Cox. Virtual Specimen Generator, Version 2013a, last accessed: August 2012. http://www.engineering.ucsb.edu/~mblacklock/VSG/, 2013. 2.3.2, 4.3.1, 6.3.1

M. Blacklock, J. H. Shaw, F. W. Zok, and B. N. Cox. Calibrated stochastic virtual specimens for analyzing local strain variations in woven ceramic composites. In preparation, 2014. 3.1, 3.3, 3.2, 3.6, 3.10, 3.11

M. Blacklock, F. W. Zok, and B. N. Cox. A voxel-based approach to meshing woven fibre composites. *8th Australasian Congress on Applied Mechanics*, submitted, 2014. 4.3.1

Boeing. Boeing X-51A WaveRider sets record with successful 4th flight, 2013. URL http://boeing.mediaroom.com/2013-05-03-Boeing-X-51A-WaveRider-Sets-Record-with-Successful-4th-Flight#assets_117. 1.1

B. Budiansky, J. W. Hutchinson, and A. G. Evans. Matrix fracture in fiber-reinforced ceramics. *Journal of the Mechanics and Physics of Solids*, 34(2):167–189, 1986. 3.2.2

C. M. Cady, T. J. Mackin, and A. G. Evans. Silicon carbide/calcium aluminosilicate: A notch-insensitive ceramic-matrix composite. *Journal of the American Ceramic Society*, 78(1):77–82, 1995. 5.1

N. Chawla, Y. Tur, J. Holmes, and J. Barber. High-frequency fatigue behavior of woven-fiber-fabric-reinforced polymer-derived ceramic-matrix composites. *Journal of the American Ceramic Society*, 81(5):1221–1230, 1998. 1.2, 3.1

R. M. Christensen and K. H. Lo. Solutions for effective shear properties in three phase sphere and cylinder models. *Journal of the Mechanics and Physics of Solids*, 27:315–330, 1979. 1.3, 3.3.2

B. N. Cox and M. S. Dadkhah. The macroscopic elasticity of 3D woven composites. *Journal of Composite Materials*, 29(6):785–819, 1995. 1.2, 3.1, 3.4.1

B. N. Cox and G. Flanagan. *Handbook of analytical methods for textile composites*. 1997. 1.2, 2.2.1, 3.1, 3.4.1, B

B. N. Cox and Q. D. Yang. In quest of virtual tests for structural composites. *Science*, 314(5802):1102–7, 2006. 1.1, 3.1

B. N. Cox, W. C. Carter, and N. A. Fleck. A binary model of textile

composites—I. Formulation. *Acta metallurgica et materialia*, 42(10):3463–3479, 1994. 1.3

B. N. Cox, H. A. Bale, M. R. Begley, M. Blacklock, B.-C. Do, T. Fast, M. Naderi, M. D. Novak, V. P. Rajan, R. G. Rinaldi, R. O. Ritchie, M. N. Rossol, J. H. Shaw, O. Sudre, Q. D. Yang, F. W. Zok, and D. B. Marshall. Stochastic virtual tests for high-temperature ceramic matrix composites. *Annual Review of Materials Research*, 44(1):140512172139009, 2014. 1.3, 1.4

S. Daggumati, E. Voet, W. Van Paepegem, J. Degrieck, J. Xu, S. Lomov, and I. Verpoest. Local strain in a 5-harness satin weave composite under static tension: Part I – experimental analysis. *Composites Science and Technology*, 71 (8):1171–1179, 2011. 1.2, 3.1

S. Flores, A. G. Evans, F. W. Zok, M. Genet, B. N. Cox, D. B. Marshall, O. Sudre, and Q. D. Yang. Treating matrix nonlinearity in the binary model formulation for 3D ceramic composite structures. *Composites Part A: Applied Science and Manufacturing*, 41(2):222–229, 2010. 1.3

G. M. Genin and J. W. Hutchinson. Composite laminates in plane stress: constitutive modeling and stress redistribution due to matrix cracking. *Journal of the American Ceramic Society*, 80(5):1245–1255, 1997. 1.3

C. González and J. LLorca. Stiffness of a curved beam subjected to axial load

and large displacements. *International Journal of Solids and Structures*, 42(5-6): 1537–1545, 2005. 3.4.1

H. T. Hahn. Nonlinear behavior of laminated composites. *Journal of Composite Materials*, 7(2):257–271, 1973. 1.3

S. Hang. Tetgen 1.4.3, last accessed: April 2013. http://tetgen.org/. 3.3.1, 4.3.1

A. Haque, L. Ahmed, and A. Ramasetty. Stress concentrations and notch sensitivity in woven ceramic matrix composites containing a circular hole—An experimental, analytical, and finite element study. *Journal of the American Ceramic Society*, 88(8):2195–2201, 2005. 5.1

Z. Hashin. Analysis of properties of fiber composites with anisotropic constituents. *Journal of Applied Mechanics*, 46(3):543–550, 1979. 1.3, 3.3.2, 4.3.2, A, C, C

Z. Hashin and B. W. Rosen. The elastic moduli of fiber-reinforced materials. *Journal of Applied Mechanics*, 31(2):223–232, 1964. 1.3, 3.3.2, A

J. L. Henshall, D. J. Rowcliffe, and J. W. Edington. Fracture toughness of single-crystal silicon carbide. *Journal of the American Ceramic Society*, 60(7–8):373–375, 1977. 6.2.2

F. E. Heredia, S. M. Spearing, T. J. Mackin, M. Y. He, A. G. Evans, P. Mosher,

and P. Brøndsted. Notch effects in carbon matrix composites. *Journal of the American Ceramic Society*, 77(11):2817–2827, 1994. 5.1

D. Ivanov, S. Ivanov, S. Lomov, and I. Verpoest. Strain mapping analysis of textile composites. *Optics and Lasers in Engineering*, 47(3-4):360–370, 2009. 1.2, 3.1

Joint Technology Office on Hypersonics. Roadmap for the Hypersonics Programs of the Department of Defense, 2008. 1.1

W. Keith and K. Kedward. Notched strength of ceramic-matrix composites. *Composites science and technology*, 57(6):631–635, 1997. 5.1

Y. Kogo, H. Hatta, H. Kawada, and T. Machida. Effect of stress concentration on tensile fracture behavior of carbon-carbon composites. *Journal of Composite Materials*, 32(13):1273–1294, 1998. 5.1

E. Lara-Curzio, S. Sternstein, C. Hubbard, B. Cavin, and W. Porter. High temperature structural stability of chemically vapor-deposited silicon carbide filaments. *Materials Science and Engineering: A*, 172(1-2):167–171, 1993. 4.2.4, 1

C. G. Levi, J. Y. Yang, B. J. Dalgleish, F. W. Zok, and A. G. Evans. Processing and performance of an all-oxide ceramic composite. *Journal of the American Ceramic Society*, 81(8):2077–2086, 1998. 5.1

V. Levin. On the coefficients of thermal expansion of heterogeneous materials. *Mechanics of Solids*, 2(1):58–61, 1967. 1.3, C

H. J. Lin and Y. J. Lee. Strength of composite laminates with continuous fiber around a circular hole. *Composite Structures*, 21(3):155–162, 1992. 5.1

D. Ling, Q. D. Yang, and B. N. Cox. An augmented finite element method for modeling arbitrary discontinuities in composite materials. *International Journal of Fracture*, 156(1):53–73, 2009. 6.1

D. B. Marshall and B. N. Cox. Integral textile ceramic structures. *Annual Review of Materials Research*, 38(1):425–443, 2008. 1.1, 1.3, 5.1

M. A. McGlockton, B. N. Cox, and R. M. McMeeking. A binary model of textile composites: III high failure strain and work of fracture in 3D weaves. *Journal of the Mechanics and Physics of Solids*, 51(8):1573–1600, 2003. 1.3

J. C. McNulty, F. W. Zok, G. M. Genin, and A. G. Evans. Notch-sensitivity of fiber-reinforced ceramic-matrix composites: Effects of inelastic straining and volume-dependent strength. *Journal of the American Ceramic Society*, 82 (5):1217–1228, 1999. 5.1

J. C. McNulty, M. Y. He, and F. W. Zok. Notch sensitivity of fatigue life in a Sylramic^{TM}/SiC composite at elevated temperature. *Composites Science and Technology*, 61(9):1331–1338, 2001. 5.1

G. N. Morscher, J. Martinez-Fernandez, and M. J. Purdy. Determination of interfacial properties using a single-fiber microcomposite test. *Journal of the American Ceramic Society*, 79(4):1083–91, 1996. 6.2.2

G. N. Morscher, J. A. DiCarlo, J. D. Kiser, and H. M. Yun. Effects of fiber architecture on matrix cracking for melt-infiltrated SiC/SiC composites. *International Journal of Applied Ceramic Technology*, 7(3):276–290, 2009. 1.2

A. Nakai, T. Ohki, N. Takeda, and H. Hamada. Mechanical properties and micro-fracture behaviors of flat braided composites with a circular hole. *Composite Structures*, 52(3-4):315–322, 2001. 5.1

M. D. Novak and F. W. Zok. High-temperature materials testing with full-field strain measurement: Experimental design and practice. *Review of Scientific Instruments*, 82(11):115101, 2011. 4.1, 4.2.2

J.-J. Orteu, T. Cutard, D. Garcia, E. Cailleux, and L. Robert. Application of stereovision to the mechanical characterisation of ceramic refractories reinforced with metallic fibres. *Strain*, 43(2):96–108, 2007. 4.2.3

J. W. Pro, R. K. Lim, L. R. Pretzold, M. Utz, and M. R. Begley. GPU-based simulations of fracture in idealized brick and mortar composites. Submitted, 2014. 6.1, 6.3

L. Qin, Z. Zhang, X. Li, X. Yang, Z. Feng, Y. Wang, H. Miao, L. He, and X. Gong.

Full-field analysis of shear test on 3D orthogonal woven C/C composites. *Composites Part A: Applied Science and Manufacturing*, 43(2):310–316, 2012. 1.2, 3.1

V. P. Rajan and F. W. Zok. Remediation of a constitutive model for ceramic composite laminates. *Composites Part A: Applied Science and Manufacturing*, 52:80–88, 2013. 1.3

V. P. Rajan, M. N. Rossol, and F. W. Zok. Optimization of digital image correlation for high-resolution strain mapping of ceramic composites. *Experimental Mechanics*, 2012. 1.2, 1.4, 3.1, 3.2.1, 4.2.3

V. P. Rajan, J. H. Shaw, M. N. Rossol, and F. W. Zok. An elastic-plastic constitutive model for ceramic composite laminates. *Composites Part A: Applied Science and Manufacturing*, 66:44–57, 2014. 1.3, 1.5

R. G. Rinaldi, M. Blacklock, H. A. Bale, M. R. Begley, and B. N. Cox. Generating virtual textile composite specimens using statistical data from micro-computed tomography: 3D tow representations. *Journal of the Mechanics and Physics of Solids*, 60(8):1561–1581, 2012. 1.4, 2.3.2

M. R'Mili, T. Bouchaour, and P. Merle. Estimation of Weibull parameters from loose-bundle tests. *Composites science and technology*, 3538(56):831–834, 1996. 3.2.2

M. N. Rossol, T. Fast, D. B. Marshall, B. N. Cox, and F. W. Zok. Characterizing in-plane geometrical variability in textile ceramic composites. *Journal of the American Ceramic Society*, in press, 2014. 2.2.2, 5.1, 5.2.2, 5.2.2, 5.2.2, 5.3, 7

M. B. Ruggles-Wrenn and G. Kurtz. Notch sensitivity of fatigue behavior of a Hi-Nicalon^{TM}/SiC-B_4C composite at 1200 °C in air and in steam. *Applied Composite Materials*, 20(5):891–905, 2013. 5.1

J. R. Shewchuk. Triangle: Engineering a 2D Quality Mesh Generator and Delaunay Triangulator. In M. C. Lin and D. Manocha, editors, *Applied Computational Geometry: Towards Geometric Engineering*, volume 1148 of *Lecture Notes in Computer Science*, pages 203–222. Springer-Verlag, 1996. From the First ACM Workshop on Applied Computational Geometry. 6.3.1

O. Siron and J. Lamon. Damage and failure mechanisms of a 3-directional carbon/carbon composite under uniaxial tensile and shear loads. *Acta Materialia*, 46(18):6631–6643, 1998. 1.2, 3.1

M. Trinquecoste, J. L. Carlier, A. Derré, P. Delhaès, and P. Chadeyron. High temperature thermal and mechanical properties of high tensile carbon single filaments. *Carbon*, 34(7):923–929, 1996. 4.3.2

N. Vermaak, L. Valdevit, and A. G. Evans. Materials property profiles for actively cooled panels: An illustration for scramjet applications. *Metallurgical and Materials Transactions A*, 40(4):877–890, 2009. 1.1

Wright-Patterson Air Force Base. X-51A flight ends prematurely, 2012. URL http://www.wpafb.af.mil/news/story.asp?id=123314235. 1.1

J. Xu, B. N. Cox, M. A. McGlockton, and W. C. Carter. A binary model of textile composites—II. The elastic regime. *Acta metallurgica et materialia*, 43 (9):3511–3524, 1995. 1.3

Q. D. Yang and B. N. Cox. Predicting failure in textile composites using the binary model with gauge-averaging. *Engineering Fracture Mechanics*, 77(16): 3174–3189, 2010. 1.3

Q. D. Yang and B.-C. Do. Predicting damage evolution in composites with explicit representation of discrete damage modes. *Handbook of Damage Mechanics*, pages 1–49, 2014. 6.1

Q. D. Yang and W. Liu. An efficient A-FEM for arbitrary cracking in solids. *ICF13*, pages 1–10, 2013. 6.1